Transport Experiments in Undoped GaAs/AlGaAs Heterostructures

Wendy Wing Yee Mak

Department of Physics

University of Cambridge, Downing College

This dissertation is submitted for the degree of

Doctor of Philosophy

January 2013

To my parents, and my fellow colleagues at the Semiconductor Physics Group.

Preface

The work presented in this thesis was done in the Semiconductor Physics (SP) Group at the Cavendish Laboratory, Department of Physics, University of Cambridge between October 2008 and January 2013.

All the work presented is solely done by the author, unless explicitly stated otherwise. It has also not been submitted in whole or in part for any other degree at any university.

This thesis is less than 60,000 words in length.

Acknowledgements

First, I would like to thank my parents, for supporting me in this venture through four years.

My thanks also go to Prof. David Ritchie, for taking me on as a student, and offering guidance.

My PhD would not have been possible without the help of the post-docs in room 332, who all assisted me at one point or another. This is especially true of Dr. François Sfigakis, who is always willing to lend his expertise in everything from cryostats to experiments.; Dr. Kantimay Das Gupta, who taught me how to process in the cleanroom and is a whiz in theory; Dr Andy Croxall, who offered me useful advice on processing, and lastly, Dr. Masaya Kataoka, without whom I would not have done a Part III project in the Semiconductor Physics group and might not have considered this a choice for a PhD topic!

I would also like to acknowledge financial support from the Cambridge Overseas Trust and the Semiconductor Physics Group.

Abstract

The focus of this thesis is the study of electron transport in GaAs/AlGaAs heterostructures free of intentional dopants, and where free electrons are obtained by applying a suitable electric field. Optimisation of the fabrication process for ohmic contacts enabled 2DEGs formed at heterointerfaces just 30nm below the surface to be contacted. In addition, ohmic contacts with resistances of less than 50 ohms can be obtained in deeper induced 2DEGs.

The transport experiments discussed are done in both 2D and in mesoscopic devices. In 2D transport, a method of determining the different background impurity concentrations in AlGaAs and GaAs in an undoped wafer was developed. In addition, it was found that bias cooling and illumination have effects on the electron mobility of undoped 2DEGs.

An investigation into the $\nu = 5/2$ fractional quantum hall state was attempted at several electron densities on a high mobility undoped sample. The measured activation gap was less than 100mK, even at the highest density. However, this may be due to the electron temperature, which was unknown, being a lot higher than the thermometer reading.

Mesoscopic devices measured included quantum dots and quantum wires. The quantum dots were made on 2DEGs at 30nm, 60nm and 110nm below the surface, and it was possible to observe the weak coupling regime in all of them. These devices show reproducible characteristics from device to device and from cooldown to cooldown. Stability measurements show that the quantum dot devices on the 60nm and 110nm 2DEGs were more stable against random telegraph signal noise as compared to those only 30nm deep. A series of bias cooling experiments was also done on one sample from each depth. Preliminary results are slightly contradictory, with the 30nm and 110nm deep devices becoming more noisy with bias cooling, as compared to a cooldown with no bias, while 60nm deep devices are quieter with a bias cooldown.

Quantum wires made on 60nm and 300nm deep 2DEGs demonstrated 1D confinement, and the zero bias anomaly effect was also seen at 300mK in the 60nm deep sample.

The final section offers some possibilities for future experiments which would give some very interesting insights into electron transport.

An appendix detailing the fabrication steps is provided.

Contents

Chapter 1

Introduction

1.1 GaAs/AlGaAs semiconductor system

The III/V semiconductor systems, with their superior mobility as compared to silicon, have been the material of choice for fundamental semiconductor physics research. One of the most common is the Gallium-Aresenide/Aluminium-Gallium-Arsenide (GaAs/AlGaAs) system [1]. In AlGaAs, atoms of Ga substitute for Al atoms, with a common fraction of Al being 0.33 (i.e., $Al_{0.33}Ga_{0.67}As$). For fractions of Al less than 0.4, there is a direct bandgap transition between the valence and conduction bands. Above this, the transition is indirect. However, it is possible to use higher fractions of Al, such as 0.9, in order to provide a stronger confinement.

GaAs and AlGaAs have the same crystal structure and very similar lattice spacings, enabling layers of both materials to be grown one on top of the other with little strain or defects, leading to a smooth interface. This means that it is possible to obtain high carrier mobilities in these samples, as a rough interface would lead to extra scattering events.

The interface between GaAs and AlGaAs forms what is known as a heterointerface. As GaAs and AlGaAs have different bandgaps, it is possible, with either suitable doping [2] or an applied electric field [3], to bend the conduction band profile such that a very thin conducting layer is formed. An example bandstructure of such a system is illustrated in fig.1.1 The confinement to two dimensions

Chapter 1

Introduction

1.1 GaAs/AlGaAs semiconductor system

The III/V semiconductor systems, with their superior mobility as compared to silicon, have been the material of choice for fundamental semiconductor physics research. One of the most common is the Gallium-Aresenide/Aluminium-Gallium-Arsenide (GaAs/AlGaAs) system [1]. In AlGaAs, atoms of Ga substitute for Al atoms, with a common fraction of Al being 0.33 (i.e., $Al_{0.33}Ga_{0.67}As$). For fractions of Al less than 0.4, there is a direct bandgap transition between the valence and conduction bands. Above this, the transition is indirect. However, it is possible to use higher fractions of Al, such as 0.9, in order to provide a stronger confinement.

GaAs and AlGaAs have the same crystal structure and very similar lattice spacings, enabling layers of both materials to be grown one on top of the other with little strain or defects, leading to a smooth interface. This means that it is possible to obtain high carrier mobilities in these samples, as a rough interface would lead to extra scattering events.

The interface between GaAs and AlGaAs forms what is known as a heterointerface. As GaAs and AlGaAs have different bandgaps, it is possible, with either suitable doping [2] or an applied electric field [3], to bend the conduction band profile such that a very thin conducting layer is formed. An example bandstructure of such a system is illustrated in fig.1.1 The confinement to two dimensions

of this layer makes some very interesting experiments possible.

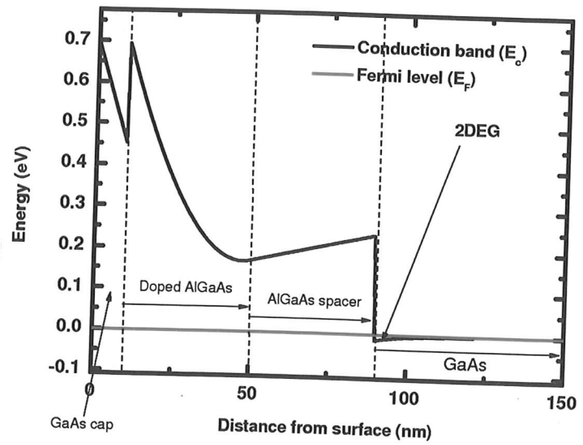

Figure 1.1: The bandstructure in a GaAs/AlGaAs heterostructure with suitable doping such that a conducting layer of electrons is formed at the interface.

1.2 The Two Dimensional Electron Gas

The following are several important properties of a two dimensional electron gas (2DEG) in a semiconductor heterostructure, such as that in GaAs/AlGaAs. More detailed derivations can be found in articles/books such as [4, 5].

In a 2DEG, where electrons are free to move in the x and y directions, but are confined in the z direction[1], the energy of the electrons is quantised in the z dimension as E_z^n, and the total energy is given by

$$E = E_z^n + \frac{\hbar(k_x^2 + k_y^2)}{2m^*} \tag{1.1}$$

where m^* is the effective mass of the electrons, and k is the wavevector. It

[1]The z direction is normally the one perpendicular to the heterointerface

can be shown that the density of states in 2D, $g_{2D}(E)$, in zero magnetic field is independent of energy, and is given by

$$g_{2D}(E) = \frac{g_s g_v m^*}{2\pi\hbar^2} \tag{1.2}$$

where g_s is the spin degeneracy of the electron and g_v is the number of conduction band minima that are relevant for transport. In GaAs, g_s=2 for electrons and g_v=1. A Fermi energy, E_F can also be defined for the 2DEG with an electron density per unit area of n_{2D}, with

$$E_F = n_{2D}\frac{2\pi\hbar^2}{g_s g_v m^*} \tag{1.3}$$

The mean free path of electrons in a 2DEG is the average distance electrons travel between scattering events. This is given by

$$l = \frac{\mu\hbar\sqrt{2\pi n_{2D}}}{e} \tag{1.4}$$

where μ is the electron mobility.

1.3 Molecular Beam Epitaxy

Molecular beam epitaxy, or MBE, is a method of growing single crystals of materials of high purity, such as the III-V semiconductor GaAs. MBE is widely used in semiconductor research. Details of how MBE works, as well as how a MBE chamber is optimised for material growth, are covered elsewhere [5, 6, 7]. Nonetheless, it is worth mentioning the development of MBE techniques over the last few decades, which had led to a large increase in sample quality and the carrier mobility, as illustrated in fig.1.2. Samples with the highest quality have enabled exotic effects such as Fractional Quantum Hall effects[8], complex structures in the $\nu = \frac{5}{2}$ Fractional Quantum Hall state [9], microwave induced resistance oscillations [10, 11], and new phases of electron solids [12] to be studied.

Most of the work presented in this thesis is based on GaAs/AlGaAs wafers grown at the MBE facilities at the Cavendish Laboratory. An exception is the

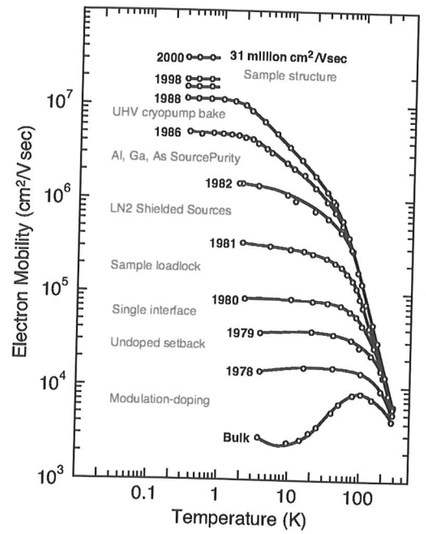

Figure 1.2: Improvements in carrier mobility in GaAs, with the development of different MBE techniques. Figure taken from [13]

wafer used in the experiment in section 3.6, which is grown at the MBE facilities at the ETH Zurich, Switzerland. Unless specified otherwise, any samples referred to in this work is a GaAs/AlGaAs heterostructure.

1.4 Thesis overview

In this thesis, I will discuss how to fabricate samples from undoped GaAs/AlGaAs heterostructures, the experiments that can be done on these samples, and the advantages that they offer over their doped counterparts. The experiments are divided into two main areas: two dimensional transport in chapter 3, and mesoscopic transport through devices such as quantum dots and quantum wires in chapter 4. Through these two aspects, I will explore the insights that induced devices offer, as well as the possibilities that they present for future experiments.

Whilst I may not have gone into huge depths on each experiment, preferring instead to try out the many ways induced devices can be used, each section has the potential to be developed further, and to yield some very interesting results.

Chapter 2

The Induced Device

What is an induced device? How do they work, and how does one go about making them? These questions will be answered in this chapter, together with a discussion of why one would even want to make them in the first place.

2.1 Bandstructure

In contrast to a GaAs/AlGaAs system where dopants cause the conduction band to dip below the Fermi level, resulting in a conducting layer, an undoped GaAs/AlGaAs system requires a voltage to be applied to a topgate covering the area of interest to bend the bandstructure, and hence to 'induce' carriers. Fig.2.1(a) shows the wafer structure of an undoped heterostructure, and fig.2.1(b) shows the bandstructure in an unbiased condition: the conduction band and the Fermi level are flat, and the conduction band does not dip below the Fermi level, so there are no carriers. On applying a voltage, the Fermi level and the bands bend according to how much voltage is applied to the topgate. Fig.2.2 illustrates a situation where the applied voltage is sufficient to cause the conduction band to dip below the Fermi level. The shape of the potential is triangular as there is only one heterointerface. A higher applied voltage will result in greater band bending and a deeper well and hence a higher electron density.

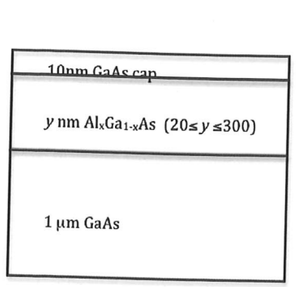

(a)

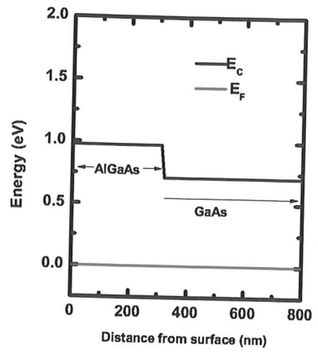

(b)

Figure 2.1: The structure of an induced wafer is shown in (a), and (b) shows what its bandstructure is when no voltages are applied.

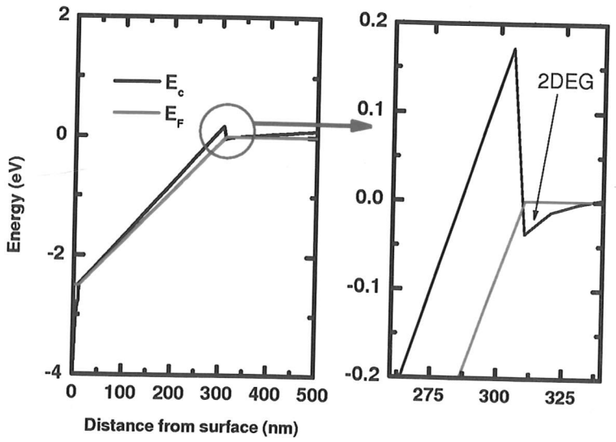

Figure 2.2: Bandstructure of an induced 2DEG, with the heterointerface 300nm below the surface. The topgate voltage is sufficient to generate the 2DEG in this case. The band energies are calculated with a 1D Poisson solver [14].

2.2 Advantages of using undoped samples

The first question one may ask is: why study undoped devices? After all, one has to redo many experiments already done on doped samples in order to optimise the system for the undoped structure. However, there are many areas where undoped samples offer advantages over their doped counterparts. The following discusses a few major ones, but hopefully, it shall become clear from the rest of this thesis that there are many more ways in which induced devices offer insights that cannot be obtained easily from doped samples.

2.2.1 Achieving low carrier densities

At low carrier densities, the factor limiting mobility is scattering from ionised impurities, be they intentional dopants or background impurity atoms. As the concentration of dopants is much higher than background impurity ions (by at least four orders of magnitude), the increased scattering from these dopants means that the mobility of doped wafers at low carrier densities is limited. An undoped sample is therefore able to maintain a higher mobility than a doped sample at a low carrier density. This is illustrated in fig.2.3. Both wafers are grown with the MBE chamber under similar conditions, being less than 20 wafers apart in the growth run. They also had similar mobilities ($\sim 10^7 \mathrm{cm}^2\mathrm{V}^{-1}\mathrm{s}^{-1}$) at high densities ($\geq 10^{11}\mathrm{cm}^{-2}$), and thus they form a good comparison of doped versus undoped samples.

As can be seen in fig.2.3, the mobility of the undoped sample at carrier densities of $\lesssim 2\mathrm{x}10^{10}\mathrm{cm}^2$ is much higher than the doped sample. As the low density regime is of interest in studies where electron interaction is very strong (e.g. Wigner crystallisation), and the region near pinch off in mesoscopic devices, undoped devices offer a much better system to investigate these effects. Undoped samples can also reach much lower densities than doped samples. The lowest carrier density ever measured was $7\mathrm{x}10^8\mathrm{cm}^{-2}$ in an undoped 2DHG [15].

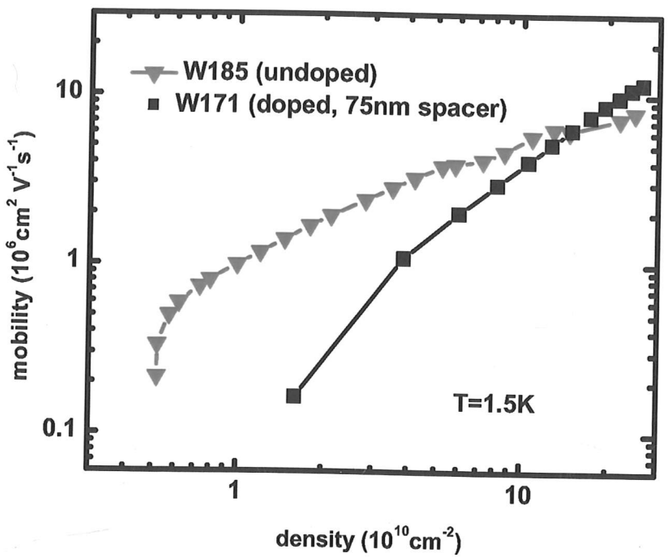

Figure 2.3: Comparing the mobilities of a doped heterostructure and an undoped heterostructure. Whilst the maximum mobility of the undoped wafer is less than the doped sample, its mobility at low densities is higher. The undoped sample was also able to reach a lower density.

2.2.2 Gateable high density/mobility samples with no parallel conduction

Experiments that require the highest quality material, such as those investigating 'fragile' fractional quantum hall states, utilise very high mobility wafers. In doped wafers, this means very high doping levels in order to obtain a high carrier density where mobility is higher. Many of these wafers are not gateable as the applied voltage causes the dopant layer to parallel conduct, or because of leakage between the gate and the dopants.

In contrast, an undoped sample is always gateable—especially as it depends on gates to form the conduction layer in the first place. This means that carrier density can be varied in experiments, which can be used to investigate the effects of different scattering mechanisms in transport.

2.2.3 Very shallow, gateable 2DEGs

For mesoscopic devices defined by surface gates, a shallow 2DEG depth is advantageous as the electrostatic potential from the gates is better defined, and there has been interest in using shallow 2DEGs for devices such as quantum dots [16]. While 2DEGs that are very shallow (i.e. less than 50nm below the surface) are possible in doped samples, e.g.[17, 18], they require very high levels of doping to bend the bandstructure enough to ensure conduction in the 2DEG.

The high doping levels, together with the very thin spacer layer between the doping layer and the 2DEG, means that scattering from ionised dopants is more significant in shallow doped 2DEGs, and hence they tend to have quite low mobilities as compared to deeper doped 2DEGs. Undoped shallow 2DEGs do not suffer from the scattering from intentional dopants, and can therefore reach higher mobilities than their doped counterparts, as fig.2.4 illustrates.

Mobility is not necessarily the most important consideration in mesoscopic transport. However, a device on an undoped wafer with higher mobility at similar densities is less likely to suffer from interactions with unintentional dopants, which could cause noise in the device.

Besides a higher mobility, undoped 2DEGs offer another advantage for mesoscopic devices: their gateability. Most of the nanostructure devices on doped,

very shallow 2DEGs reported in literature require atomic force microscope (AFM) lithography to form the 2DEG into the mesoscopic region (e.g.[24]). Gating was not possible on many of these wafers due to high doping levels causing the dopant band to parallel conduct, and therefore screening any potential applied from the surface gates.

These advantages mean that shallow, undoped 2DEGs offer a good basis for experiments with mesoscopic devices.

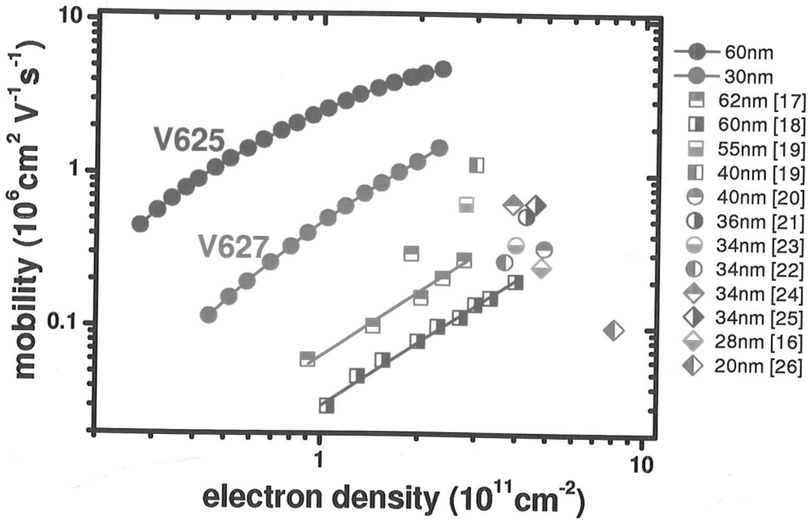

Figure 2.4: Density-mobility relation of very shallow 2DEGs, comparing two undoped samples made from wafers V625 and V627, which were grown in MBE facilities in this group, with doped samples reported in literature

2.3 Device Configuration

Fig.2.5 shows the different layers of an induced device. This configuration is optimised for mesoscopic devices, with very few ohmics and a large number of surface gates. However, the basic layers are the same across all induced devices:

the etched mesa, ohmics, insulator, and the topgate. Surface gates are required to define fine features, such as in mesoscopic devices, or for low density measurements.

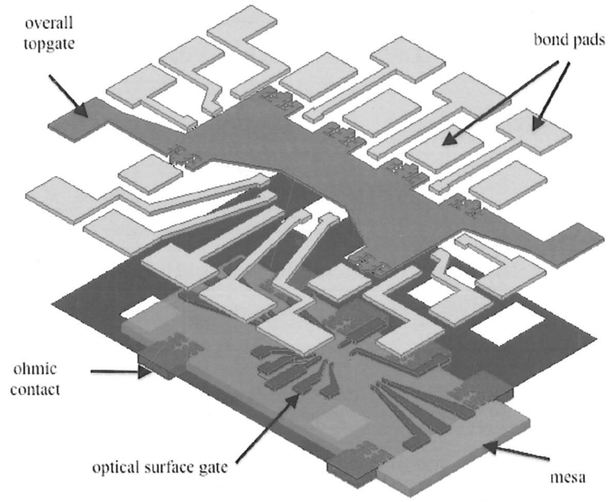

Figure 2.5: The components of an induced device. This particular pattern of gates is configured for mesoscopic devices.

In induced devices, the 2DEG only exists in the areas covered by the topgate. The etched mesa, while useful for defining the area of the device, does not have an important function. This is in contrast to doped samples where the mesa etch is crucial to defining the transport region. The ohmic contacts provide a way of accessing the device, and should be of low resistance. How to obtain good ohmic contacts to induced 2DEGs is discussed later on in this chapter. The 2DEG is generated upon applying a voltage to the topgate, and thus an insulating layer between the ohmic contacts and the gate is required to for a voltage to be maintained on the topgate. For 2D measurements, the variation in topgate voltage produces a change in carrier density, and this is sufficient to do four terminal measurements such as the mobility vs carrier density measurements, or higher magnetic field sweeps to look for Fractional Quantum Hall states.

In mesoscopic devices, voltages would be applied to the fine surface gates to provide additional confinement. As opposed to doped devices, where the surface gates have no effect on transport until a voltage is applied, in an undoped sample, the surface gates always have an effect, even at 0V. This is because they screen the topgate voltage, and as a result the carrier density under them and in the constriction defined by the gates would be quite different from the density further away.

2.3.1 Gate leakage

In induced samples, either a 2D or mesoscopic, the definition of a good device is one that does not leak, ie, there is no current path between the topgate and the ohmic contacts and/or surface gates, and none between the surface gates to each other and/or the 2DEG via impurities. In fact, as fig.2.6 shows, when there is a large enough leakage between the topgate and the ohmic contacts, the 2DEG can no longer be generated and the conductance drops to zero. Any leaks/shorts between surface gates in mesoscopic devices such as quantum dots would yield a non-working device as well.

2.4 Fabrication challenges

While induced devices offer advantages over their doped counterparts, there are certain fabrication steps which are more complex, and required optimisation in order to obtain good working devices. The following is a discussion of some of these issues.

2.4.1 Ohmic contacts to an induced 2DEG

One major difference in fabrication between doped and undoped samples is the ohmic contacts. In doped samples, the ohmic material will provide a contact as long as it can punch through to the conducting layer. Thus, they are usually made by depositing material onto the surface of the sample. An annealing process, where the sample is heated for a short time at around 400 °C, causes the material to diffuse into the sample and reach the conducting layer.

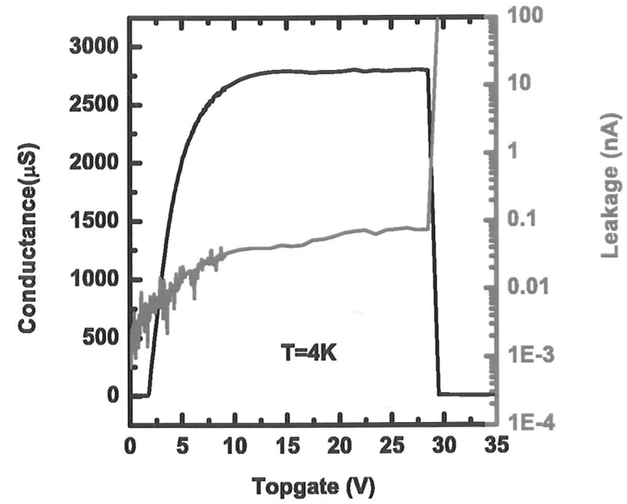

Figure 2.6: The leakage current of the top gate to the 2DEG as the topgate is swept, together with the two terminal conductance between a pair of ohmic contacts. This was measured on a sample with polyimide as the insulator. At operation of similar devices, top gate voltages are typically between 10 and 20V, below where the insulator breaks down.

However, this process would not work well for induced devices. This is because the conducting layer depends on the applied gate voltage, and if the top of the contact is wider than the area where metal penetrates to the heterointerface, then the voltage will be screened and the 2DEG will not be continuous with the ohmic contacts. This situation is illustrated in fig.2.7(a).

Therefore, ohmic contacts to induced 2DEGs are recessed. The area where the material is to be deposited is first etched away using a chemical etchant, with the depth of the etch greater than the depth of the heterointerface from the surface. Then, the material is deposited, and annealed. The recess means that the material can diffuse sideways into the interface so that the gate voltage is no longer screened and the 2DEG can be continuous with the contacts, as illustrated in fig.2.7(b).

The profiles of the ohmic contacts in fig.2.7 are idealised: not all doped ohmic contacts have a profile like fig.2.7(a), and the material will go sideways as well as down in the annealing process. However, the random nature of the diffusion process means that a 'top down' ohmic contact is likely to have a large area where situation (a) occurs, whereas recessed ohmics contacts will favour situation (b), and provide a better contact to the induced 2DEG.

The voltage difference between the topgate, the ohmic contacts and the wafer can only be maintained if there are no shorts between the gate and the ohmic contacts. One major source of shorts is spikes formed in the ohmic material during annealing. Thus the overlap between the topgate and the ohmic contacts is minimised to reduce the chance of a short forming. However, to decrease the resistance of the contacts, the perimeter should be maximised. Therefore, the ohmic contacts have multiple 'wiggles', as illustrated in fig.2.5 (p.13).

2.4.2 Ohmic optimisation

Getting working ohmic contacts to an induced 2DEG is the hardest part of the processing, due to the complexity of the etching and the possibility of spike formation. In addition, for certain experiments, the contacts would also have to work in high magnetic fields, low temperatures and have a very low contact resistance.

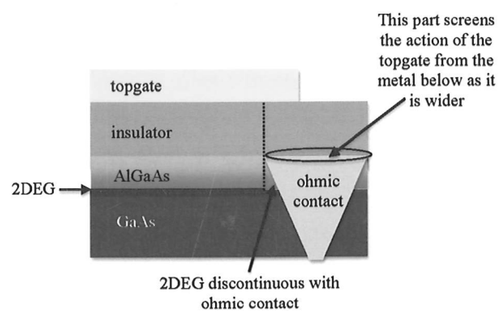

Figure 2.7: The diffusion profiles of (a) ohmic materials deposited onto the surface of the wafer and, (b) ohmic material deposited in an etched pit. The profile of the ohmic contact in (a) means that it will not be continuous with the 2DEG, whereas (b) can provide a contact.

Using a fabrication method very similar to those in [27, 28], one is able to obtain good ohmic contacts to a deep (ie 300nm) undoped heterostrcuture. However, improvements were necessary to lower the contact resistance further, to improve the surface morphology of the contact to reduce spike formation and to increase yield.

The optimal situation for the ohmics is where most of the material diffuses sideways into the GaAs/AlGaAs during the annealing process. i.e. little material goes upwards, giving ohmics that are very smooth. To achieve this, the wetting of the side walls of the etch pit of the ohmic contacts is important. Therefore, optimisation is carried out both on the etch profile of the pit of the recessed ohmics as well as the actual evaporation itself, such that the deposited material wets the sidewalls nicely. To improve the profile of the etch pit, two different etch solutions were tried.

Fig.2.8 shows the etch profiles using two different etch solutions: 4:5:80 H_2SO_4:H_2O_2:H_2O (sulphuric acid etch) and 1:1:20 H_3PO_4:H_2O_2:H_2O (phosphoric acid etch). The sulphuric acid etch gave an undercut profile to the top layer of AlGaAs. In contrast, the phosphoric acid etch gave an almost vertical profile in the AlGaAs layer. The ohmic material can therefore reach the interface, where the 2DEG forms, more easily.

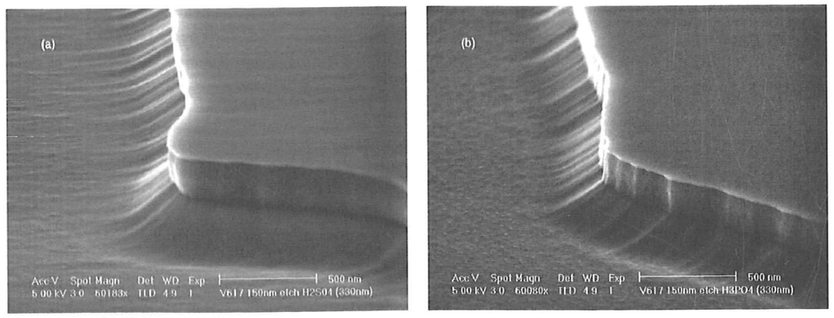

Figure 2.8: SEM images of the etch profiles of the ohmics pit using two different etch solutions: (a) 4:5:80 H_2SO_4:H_2O_2:H_2O and (b) 1:1:20 H_3PO_4:H_2O_2:H_2O

An added advantage of the phosphoric acid etch is that it gives an almost equal etch rate in GaAs and AlGaAs. As shown in fig.2.9(a), the etch rates in two undoped wafers with the heterointerface at different depths are the same

within experimental error. In contrast, the sulphuric acid etch has a different etch rate in the two different materials. As shown in fig.2.9(b), wafers with the heterointerface at different depths have different etch rates, and a clear change in the etch rate as the solution reaches a different material could also be seen on the data from the wafer with a 300nm deep heterointerface. Thus, by using a phosphoric acid etch solution, wafers with the interface at different depths can be etched to the same depth using identical times, reducing the need for calibrating the etch solution for each chip.

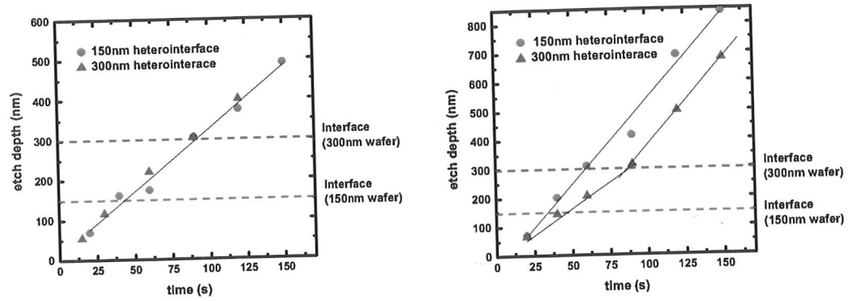

Figure 2.9: Etch rates of (a) 1:1:20 H_3PO_4:H_2O_2:H_2O and (b) 4:5:80 H_2SO_4:H_2O_2:H_2O on two different undoped wafers with the heterointerface at 150nm and 300nm below the surface

The second step is to optimise the metal deposition process. This is especially important for contacting shallow 2DEGs, and is discussed in the following section.

2.4.3 Contacting a very shallow 2DEG

For very shallow 2DEGs, where the interface is 60nm or less from the surface, it is very important that the ohmic material can actually reach the interface. As the recessed ohmic is etched using a wet etchant, the photoresist produces an overhang, which prevents the ohmic material from reaching the sidewalls closest to the surface during evaporation, as fig.2.10(a) shows. However, it is possible to remove most of this overhang by doing an extra microwave ash after etching. The ashing time is calibrated using an AFM such that a small amount of overhang

is left to assist in liftoff and prevent the ohmic material from depositing on the surface outside the etch pit. As fig.2.10(b) illustrates, the metal can now reach the interface. This step is crucial to contacting a shallow 2DEG. Samples with insufficient/no ashing could not conduct at all, suggesting that the ohmic material has not reached the interface. A rinse in HCl after the microwave ashing step ensures that any oxides formed on the walls of the etch pit are removed.

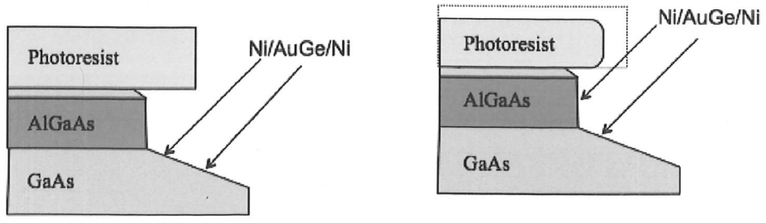

(a) (b)

Figure 2.10: An illustration of how the ashing step is crucial for ohmic material to reach the interface for very shallow 2DEGs

During the metal deposition process, the evaporation of Ni(10nm)/AuGe(250nm)/ Ni(120nm) is carried out with the sample angled at 60° to the vertical. The sample was held in a rotatilt which enabled the sample to be rotated around. This ensures very good sidewalls wetting. Figure 2.11 shows an AFM scan of an ohmic contact made using this process. One can see that the metal has wetted the sidewalls completely, but there are no spikes formed.

Using the phosphoric acid etch together with the overhang removal and the rotatilt evaporation step, it is possible to contact 2DEGs that are 30nm below the surface, with a contact resistance of less than 1kΩ. On deeper 2DEGs, especially on high mobility wafers, the contact resistance can be as low as 20Ω.

For samples where the 2DEG was just 30nm below the surface, the composition of the AlGaAs layer also had to be changed from $Al_{0.33}Ga_{0.67}As$ to $Al_{0.90}Ga_{0.10}As$ to prevent charges from leaking through the AlGaAs barrier to the surface. This was found by comparing two undoped wafers with the heterojunction 30nm below the surface: V626 with $Al_{0.33}Ga_{0.67}As$ barrier and V627

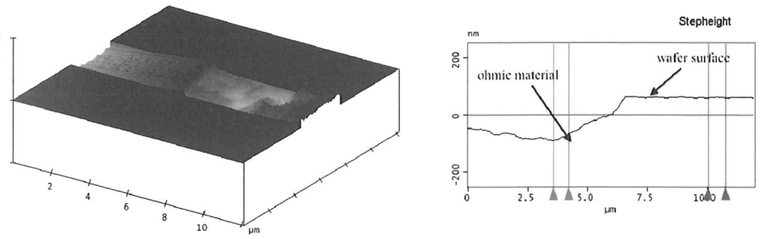

(a) (b)

Figure 2.11: An AFM scan of an ohmic contact on an induced device made with a rotatilt evaporation following an overhang removal with a microwave ash. (a) shows the three dimensional scan and (b) is a linescan through the same region to illustrate the relevant heights.

with $Al_{0.90}Ga_{0.10}As$ barrier. V627 conducts and is able to maintain the 2DEG for at least 3 days. In contrast, the conductance in V626 drops to zero within a few minutes of the 2DEG being induced. This 'charge leakage' is different to leakage to the topgate: the voltage is still maintained on the topgate, with no leakage current detected by the SMU. This effect is probably due the thin $Al_{0.33}Ga_{0.67}As$ barrier not being high enough to prevent electrons from tunnelling from the 2DEG to the surface. Once electrons have tunnelled to the surface, they would screen the topgate, resulting in the 2DEG underneath disappearing.

Fig.2.12 shows four terminal magnetotransport measurement of a hall bar from a wafer that has a heterointerface 30nm beneath the surface (V627). The longitudinal resistance at integer Landau level filling factors goes to zero at 300mK, showing that there is no parallel conduction. Also note that the ohmic contacts are still working at fields up to 9T. The inset shows a density vs topgate voltage trace. It is linear, with no gate hysteresis or saturation.

2.4.4 Contacts to a 2DHG

The lack of dopants in an induced system means that, by applying a negative topgate voltage, it is possible to have holes as carriers instead of electrons. However, challenges remain in obtaining good ohmic contacts to an undoped two dimensional hole gas (2DHG). In doped samples, AuBe is used for hole gas contacts.

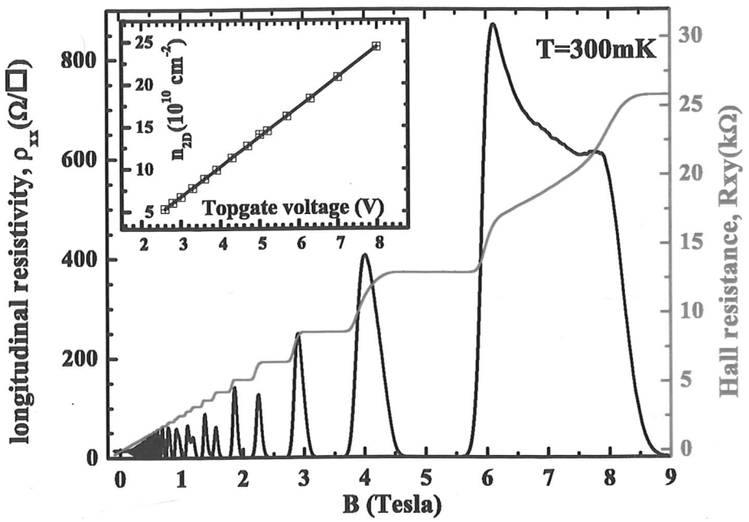

Figure 2.12: Shubnikov-de-Haas oscillations and Hall measurements on a very shallow induced 2DEG , with the heterointerface 30nm below the surface. The 2D density, n_{2D}=2.45x10^{11}cm^{-2}, and the mobility, μ=1.68x10^6cm^{2}V^{-1}s^{-1}. The inset shows the density versus topgate relation of the sample.

Similarly, this was tried in undoped 2DHG devices. The steps in processing the hole gas contacts were the same as for electron gas contacts, with the only difference being the ohmic material. It was found that AuBe on its own would give a very rough contact after annealing, which would render the device inoperable, as the spikes would form a short to the topgate. However, a capping layer of Ni, deposited before annealing, helps in smoothing the contact, as fig.2.13 shows. Nevertheless, the yield is still much lower than for induced 2DEGs, and more investigations into the best method to contact an induced 2DHG is required.[1]

2.4.5 Choice of insulator

The insulator is crucial to the operation of an induced device, as this separates the topgate from the ohmics and enables a voltage to be applied to 'induce' carriers. Polyimide was used in the work done in [27, 28], as well as in most of the samples used in the experiments presented in this thesis. Polyimide is a good option for an insulator as it is easy to process, and can be patterned optically. However, for good insulation, the layer has to be very thick, typically between 500nm to 1μm, requiring high voltages (>10V) to reach high carrier densities. In addition, the thickness of the polyimide may show non-uniformities, leading to a variation in the carrier density through the sample. This can be a problem, especially in measurements where there are stringent uniformity requirements, such as observing Fractional Quantum Hall states.

As an alternative, SiO_2 deposited by PECVD (plasma-enhanced chemical vapour deposition) was tested. It was found that a layer as thin as 175nm can provide good insulation. The voltage required to reach a similar carrier density to a polyimide sample was also reduced by approximately one third. Another advantage is the conformal coating provided by the PECVD process, ensuring a uniform thickness. However, there are also disadvantages to SiO_2. The processing is more complex, as the SiO_2 cannot be patterned during the PECVD process. Hence, the insulator has to be etched away from regions in which it is not required using buffered HF after the deposition. In addition, above a certain voltage on

[1] Recent work by Dr. Croxall and others at the Cavendish seems to indicate that a recess etch that ends just before the GaAs/AlGaAs interface, together with an ohmic evaporation done with a rotatilt can improve yield.

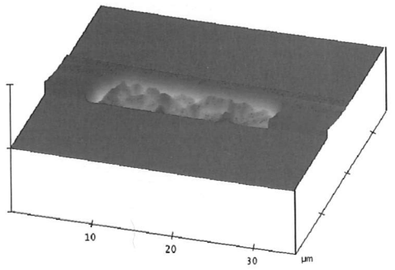

(a)

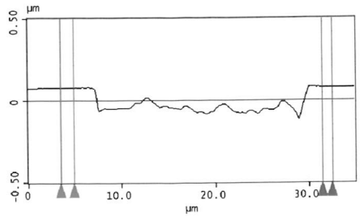

(b)

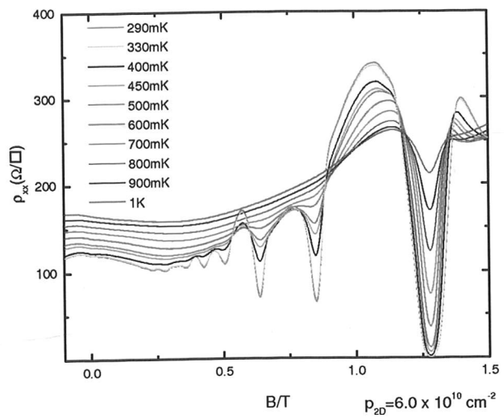

(c)

Figure 2.13: (a) shows an AFM scan of a Ni capped AuBe ohmic contact to an induced 2DHG. There are no spikes in this sample, which is crucial for an induced device to work. (b) shows a cross section of the scan image shown in (a). (c) shows the operation of the device with the AuBe ohmics. A four terminal measurement was made at temperatures from 1.5K to 300mK. The Shubnikov de Haas oscillations become more pronounced on cooling from 1.5K to 300mK, as one would expect in a 2DHG, as holes have a higher effective mass than electrons.

the topgate, the insulator causes the gate voltage versus density curve to become hysteretic, and consequently, the conductance of the 2DEG also shows significant drift. Nevertheless, this does not happen until the 2DEG density reaches approximately 3-4x10^{11}cm^{-2}, which is sufficiently high for most purposes. The threshold voltage for this behaviour is dependent on the thickness of the insulator, with a thicker layer having a higher threshold, and vice versa.

2.4.5.1 Influence of insulator on the density-mobility relation

The choice of insulator can also affect the density-mobility relation of a 2DEG. This effect is more pronounced for 2DEGs closer to the surface, with deeper 2DEGs hardly affected at all. Fig.2.14 shows the data from two undoped wafers, both with the heterointerface 60nm below the surface. The differences between the density-mobility relation for samples from the same wafer using different insulators can be modelled by changing the surface charge density[1]. As can be seen in fig.2.15, in deeper 2DEGs, where the surface states do not affect transport, there is little difference between the density-mobility relations of samples with polyimide or SiO_2 as the insulator.

In 60nm deep 2DEGs, the difference in the density-mobility relation between samples with different insulators may be explained by charges that are locked into the insulator during processing. However, this effect seems to be random, i.e. using polyimide does not necessarily give samples with better/worse mobility.

To have more information as to whether one insulator will tend to give a better density-mobility relation than the other, more samples from the two wafers can be measured. These samples will be made in different processing runs to check whether the slight variations in processing conditions is enough to make a difference.

Nonetheless, the density-mobility trace for each sample are reproducible between cooldowns, and thus any density-mobility data taken is accurate for that particular sample.

Samples used for the experiments discussed in this thesis are made with either insulator. However, certain experiments compare samples with variations such

[1]Details of the factors affecting mobility will be discussed in Chapter 3.

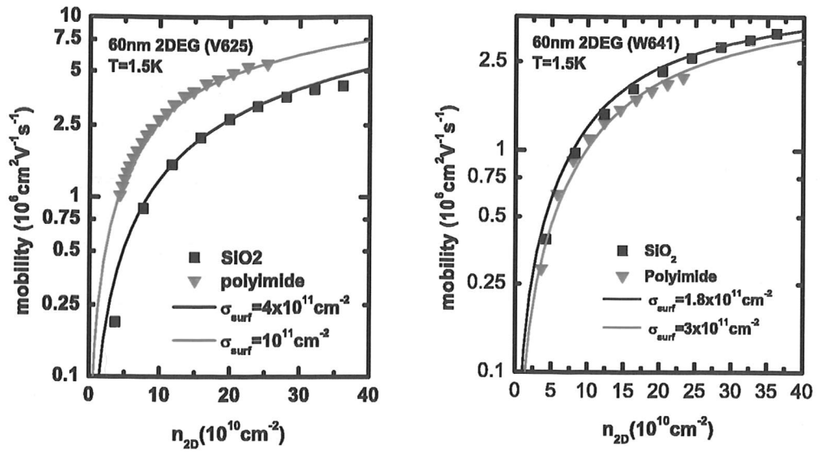

Figure 2.14: Comparisons of undoped samples made with either polyimide or SiO_2 as insulator, where the 2DEG is 60nm below the surface. Symbols are measured data, lines are calculated with the density-mobility model described in Chapter 3 with all parameters identical except for the surface charge density.

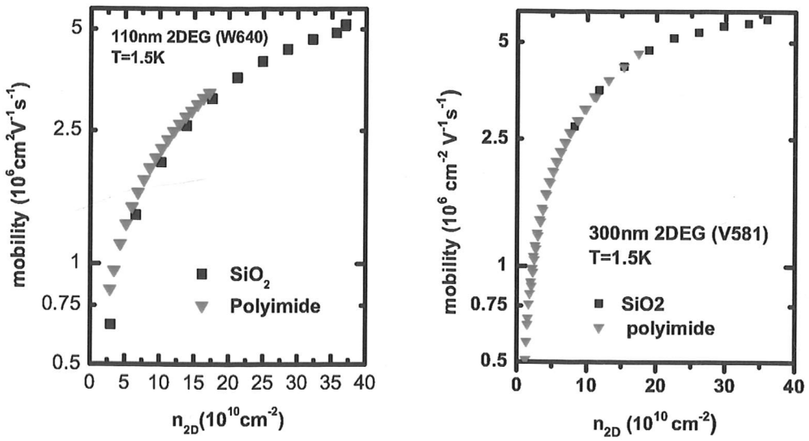

(a) (b)

Figure 2.15: Comparisons of undoped samples made with either polyimide or SiO_2 as insulator, with the 2DEG at distances of (a) 110nm and (b) 300nm below the surface.. On these deeper 2DEGs, changing the insulator made little difference to the density-mobility relation.

as the depth of the 2DEG, and these will have the same insulator if possible, to eliminate any effects of changing insulator on sample properties.

2.5 Measurement techniques

There are a few standard techniques that are used throughout the experiments in this thesis, both in electrical measurements and achieving low temperatures; these are presented below.

2.5.1 Voltage sources

As there is no way to obtain a 2DEG in induced devices without an applied topgate voltage, nor to have a lower dimensional device without voltages on surface Schottky gates, there are two main voltage sources used: a Keithley 2400 Source Measure Unit (SMU) for 2D devices, and IOTech high resolution digital-analogue converters (DAC) for mesoscopic devices. SMUs have the advantage of being able to limit their output current, and to prevent large leakage currents from permanently damaging samples. However, they introduce noise into the circuit, and do not work with the RC filters used on the Schottky gates. DACs, on the other hand, when used with filters, introduce little noise into the circuit, and can have very high resolution. However, a disadvantage is that one cannot set a current limit, and they can supply up to 10mA. This equates to approximately 1-10μA with a gate filter. Thus if a gate starts leaking, the large current flow is sufficient to damage the device permanently.

2.5.2 Four terminal measurements

Constant current, four terminal measurements were carried out to obtain the density-mobility relationship of various 2DEGs, as well as to explore Quantum Hall effects. The basic setup is illustrated in fig.2.16. The hall voltage, V_{xy}, is measured between ohmics 1 and 3, or 2 and 4. The longitudinal voltage, V_{xx}, is measured between ohmics 1 and 2, or 3 and 4.

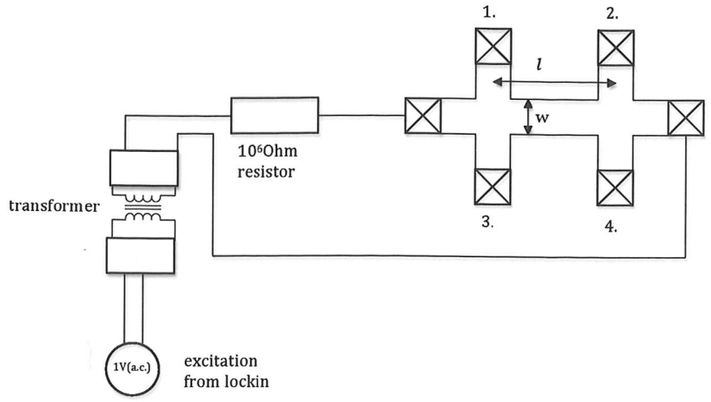

Figure 2.16: Setup for a four terminal, constant current measurement to obtain the density mobility relationship of a 2DEG

The carrier density is related to the Hall resistance R_H:

$$n_{2D} = \frac{B}{eR_H} \tag{2.1}$$

where $R_H = V_{xy}/I$. As I remains constant, it is simple to obtain n_{2D}. We can also obtain the carrier mobility, μ, which is related to the longitudinal resistivity ρ_L and carrier density by the following equation:

$$\mu = \frac{1}{n_{2D}e\rho_L} \tag{2.2}$$

where

$$\rho_L = \frac{V_{xx}(B=0)}{I(l/w)} \tag{2.3}$$

Density and mobility data was obtained via sweeping the magnetic field from -0.2T to 0.2T in the hall measurement configuration and from 0.2T to -0.2T in the longitudinal configuration. The hall slope is then fitted with a linear relation to calculate the density, whereas the zero field longitudinal resistance was also obtained in the sweep. The gate voltage was not changed until both sweeps are done to ensure that there is no offset in density between the two measurements.

2.5.3 Two terminal conductance measurements

To measure mesoscopic devices, the setup shown in fig.2.17 is used. The constant excitation voltage applied means that the conductance at any point can be obtained easily. The value of 20μV as the excitation voltage, obtained by a voltage divider placed as close to the sample as possible , was the maximum voltage that could applied at 300mK without changing the device characteristics. The series of RC filters, and the RF filter box shown, are used to protect the device from electrical spikes and to reduce noise. This is especially important for quantum dot devices, where the currents coming out of the device are only a few tens of pico amps. In addition, it was also found that the input to the lockin amplifier also outputs noise that can reach the device. Therefore, a multipole filter was used at the input to the lockin to filter this. The presence of the filters, which have a response time, means that to observe effects such as Coulomb blockade and conductance quantisation in mesoscopic, one has to sweep the gate voltages on the Schottky gates fairly slowly. This is typically around 1-2V/hr.

2.5.4 Low temperature systems

All of the devices discussed in this thesis require very low temperatures (< 100K) to operate, and most of the measurements were conducted below 4K. There are four main temperature regimes: 4K for testing devices, with the main experiment conducted at either 1.5K, 300mK or < 100mK.

At 4K, it is sufficient to test whether the ohmics work and that there is no leakages in the gates. It is also useful to check at this point that there is no significant drift in the conductance when the topgate voltage is held steady. Mesoscopic devices can be tested to check that the Schottky gates respond to the applied voltage.

Measurements involving investigation into density-mobility relations were carried out in a pumped He^4, 1.5K cryostat, as this enabled samples to be changed or thermocycled rapidly. The mobility of electrons does not vary significantly below 1.5K, and thus there is little gain in going to colder temperatures, and hence more complex systems.

Mesoscopic devices, such as quantum dots and quantum wires were mea-

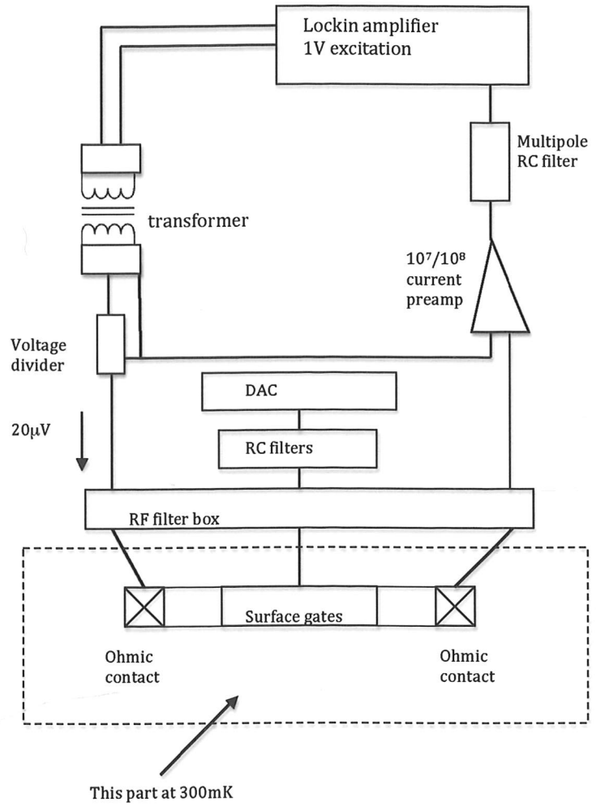

Figure 2.17: Setup for a two terminal, constant voltage measurement used to study mesoscopic devices. Each RC filter consists of two 1MΩ resistors and one 100nF capacitor. The multipole RC filter has four 1kΩ resistors in series and three 100nF capacitors in parallel. Each line in the RF filter box is connected to a 1500pF filter manufactured by Tusonix. (Product number 2463-002-X5U0-152P LF)

sured in a pumped He^3 , 300mK system. This is required as quantisation effects, such as Coulomb blockade, are not visible above approximately 1K due to thermal broadening. Peaks are also sharper as temperature decreases. Most of the measurements presented in this thesis were conducted in an Oxford Instruments Heliox system which can stay at base temperature (∼280mK) for approximately 72 hours. While the best effects would be seen in a dilution fridge, again, the 300mK system offers a much faster turnaround time, enabling more samples, as well as bias cooldown effects, to be investigated.

One set of experiments, that on the Fractional Quantum Hall effect, was carried out in a dilution fridge with a base temperature of approximately 50mK. This is required as observing certain states, such as the 5/2, which has a small activation gap, require the coldest temperatures.

2.5.4.1 Protecting induced mesoscopic devices during measurement

Mesoscopic devices, due to the presence of fine gates, can be easily damaged if there is an electric discharge from one gate to another. Besides the usual precautions of providing suitable grounding during sample cooldown and when making connections from the device to instruments, an additional step is required in induced mesoscopic devices. During liquid helium fills, or a He^3 recondensation (in which adjustments of the 1K pot needle valve are required) in the cryostat where the device is being measured, it is necessary to ground *all* gates, i.e., there must be no 2DEG while the fill is taking place. This means that the device may change slightly from fill to fill or from condensation to condensation. Thus a long hold time in the cryostat is desirable as it would enable one complete set of measurements to take place while the device is in the same configuration.

Chapter 3

Two Dimensional Transport

The experiments discussed in this chapter are all based on two dimensional transport, with the emphasis on transport under an applied magnetic field that is perpendicular to the plane of conduction. Sample sizes are typically longer than the mean free path of the electrons, i.e., the transport is diffusive, and electrons experience scattering via various mechanisms. At low magnetic fields, the behaviour of the electrons can be treated using a classical model, while their behaviour at higher fields requires a quantum mechanical explanation.

While induced 2DEGs are very simple systems, the fact that they are free of intentional dopants mean that they can offer unique insight into effects such as scattering mechanisms.

3.1 Classical transport in magnetic fields

The transport of electrons under applied electric and magnetic fields that are perpendicular to each other can be explained under the semi-classical model [29] in the low field case where the quantum effects are not significant. Besides the electric and magnetic fields, the electrons are also subject to scattering, with a characteristic scattering time of τ. Taking into account the scattering and the cyclotron motion of the electrons in the magnetic field, the equations of motion can be derived. For an electric field $\mathbf{E}=(E_x,0,0)$ and magnetic field $\mathbf{B}=(0,0,B_z)$, it can be shown that the drift velocity, $\mathbf{v}$ is given by:

$$v_x = -E_x \frac{|e|\tau/m^*}{1+\omega_c^2\tau^2} \tag{3.1}$$

$$v_y = -v_{avg}\left(1 - \frac{1}{1+\omega_c^2\tau^2}\right) \tag{3.2}$$

where $\omega_c = |e|B/m^*$ is the cyclotron frequency and v_{avg} is the average drift velocity of the electrons. When B=0, v_y=0, $v_x \rightarrow -E_x\mu$, where $\mu = |e|\tau/m^*$ is defined as the electron mobility.

The current density is related to the velocity of the electrons by $\mathbf{j} = -n_{2D}e\mathbf{v}$, and the components of $\mathbf{j}$ can be found using equations 3.1 and 3.2. Since in a two dimensional sheet of electrons in a perpendicular magnetic field, the current density, $\mathbf{j}$, is also related to the electric field $\mathbf{E}$ by $\mathbf{j} = \sigma\mathbf{E}$ where σ is the conductivity tensor, i.e.

$$\begin{pmatrix} j_x \\ j_y \end{pmatrix} = \begin{pmatrix} \sigma_{xx} & -\sigma_{xy} \\ \sigma_{xy} & \sigma_{xx} \end{pmatrix} \begin{pmatrix} E_x \\ E_y \end{pmatrix} \tag{3.3}$$

σ_{xx} and σ_{xy} can be found, and as thus the resistivity, ρ , which is the inverse of conductivity. The longitudinal and transverse resistivity can be written as:

$$\rho_{xx} = \frac{\sigma_{xx}}{\sigma_{xx}^2 + \sigma_{xy}^2} = \frac{m^*}{n_{2D}e^2\tau} \tag{3.4}$$

$$\rho_{xy} = \frac{\sigma_{xy}}{\sigma_{xx}^2 + \sigma_{xy}^2} = \frac{B}{|e|n_{2D}} \tag{3.5}$$

This means that a measurement of the longitudinal, ρ_{xx}, and the transverse, ρ_{xy}, resistivity will give parameters such as the electron density and the mobility. In the case of a Hall bar, with a constant current, I flowing through it, it can be shown that $\rho_{xy} = R_H$ where R_H is the Hall resistance. From this, one can derive the equations 2.1 and 2.2 (p.28).

3.2 Scattering Mechanisms

The mobility of carriers is limited by scattering events, caused by interactions with ionised impurities, dopants (if present), surface states, alloy scattering, and

the non uniform interface between two materials (e.g. the GaAs/AlGaAs interface). In an undoped wafer, it is possible to obtain a wide range of densities, and from determining how the mobility relates to the density, it is possible to estimate the scattering rates from each interaction. A detailed derivation of how each mechanism contributes to the mobility can be found elsewhere [5, 30]. The main points are summarised in this section, to give a better picture of how each mechanism affects the mobility of the 2DEG.

The mobility is related to the scattering relaxation time τ_T by the following relation:

$$\mu = \frac{e\tau_T}{m^*} \tag{3.6}$$

where m^* is the effective mass. At low temperatures, one can assume that the contributions from each different scattering mechanism are independent of each other, and that the they follow the relation:

$$\frac{1}{\tau_T} = \sum_i \frac{1}{\tau_i} \tag{3.7}$$

where τ_i is the relaxation time due to scattering mechanism i.

In an undoped wafer, at low temperatures, the main contributions to scattering come from background impurities in the GaAs, the background impurities in the AlGaAs, the interfacial roughness, and scattering from surface states, which is relevant for samples where the 2DEG is very close ($\lesssim$80nm) to the surface. Thus one may write the relation for the mobility as:

$$\frac{1}{\mu(N)} = \frac{m^*}{e}\left(\frac{1}{\tau_B^{GaAs}} + \frac{1}{\tau_B^{AlGaAs}} + \frac{1}{\tau_\delta^{surf}} + \frac{1}{\tau_{IR}}\right) \tag{3.8}$$

In order to calculate scattering rates, it is necessary to assume a form for the electron wavefunction in the triangular-like potential when the 2DEG is formed. The wavefunction can be calculated by a self-consistent solution of the Poisson and Schrödinger equations for the structure. However, an analytical approximation to the wavefunction is often used to make calculations easier. A common form for this is the Fang-Howard wavefunction, which takes the form $f(z)exp(i\mathbf{k}\cdot\mathbf{r})$ where z is the perpendicular direction, $\mathbf{r}$ the direction in the plane of the 2DEG,

and

$$f(z) = \left(\frac{b^3 z^2}{2}\right)^{1/2} exp\left(\frac{-bz}{2}\right) \tag{3.9}$$

Using a variational approach, one can show that

$$b = \left(\frac{33 m^* e^2 n_{2D}}{8\hbar^2 \epsilon_0 \epsilon_r}\right)^{1/3}, \tag{3.10}$$

with the relative permittivity of GaAs, $\epsilon_r = 12.8$. Limitations of a scattering model using the Fang-Howard wavefunction are discussed in section 3.2.7 (p.40).

It is also necessary to take into account the screening of scattering centres by the 2DEG. Under the Thomas-Fermi approximation, this can be described by a dielectric function, $\epsilon(q)$, which is given by:

$$\epsilon(q) = 1 + \frac{e^2}{2\epsilon_0 \epsilon_r q} \frac{m}{\pi\hbar^2} F(q) \tag{3.11}$$

with the form factors $F(q)$ and $F_1(q,z)$ being

$$F(q) = \int dz \int dz' |\phi(z)|^2 \phi(z')|^2 e^{-q|z-z'|} \tag{3.12}$$

and

$$F_1(q,z) = \int dz' |\phi(z)|^2 e^{-q|z-z'|} \tag{3.13}$$

3.2.1 Background Ionised Impurities

Ionised atoms can cause scattering events which limit the carrier mobility. These atoms are incorporated into the material during MBE growth, and can either be intentional dopants or impurity atoms. In an undoped wafer, there are only impurity atoms, which are assumed to have a certain concentration N_B^{GaAs} in the GaAs and a higher N_B^{AlGaAs} in AlGaAs. The scattering rate due to impurities is given by:

$$\frac{1}{\tau_B^{GaAs}} = N_B^{GaAs} \int_{-\infty}^{0} dz \int_0^{\pi} d\theta (1 - cos\theta) \nu(\theta, z) \tag{3.14}$$

and

$$\frac{1}{\tau_B^{AlGaAs}} = N_B^{AlGaAs} \int_0^d dz \int_0^{\pi} d\theta (1 - cos\theta) \nu(\theta, z) \tag{3.15}$$

d is the thickness of the layer of AlGaAs[1], and $\nu(\theta, z)$ is the scattering cross-section from a charged impurity at a distance z from the interface. It is given by:

$$\nu(\theta, z) = \frac{me^4}{8\pi\hbar^3 \epsilon_0^2 \epsilon_r^2} \left| \frac{F_1(q,z)}{q\epsilon(q)} \right|^2 \tag{3.16}$$

3.2.2 Surface charge

For samples in which the 2DEG is less than approximately 80nm from the surface, scattering can occur from surface states. These states arises because the Fermi level is usually 'pinned' within the band gap at the surface, which gives rise to an electric field, and can bind charges [31]. Another way of picturing the surface states is that the bonds between atoms at the semiconductor surface may not be complete, leading to charge formation. The charge on the surface also changes in order to maintain overall charge neutrality in the wafer, compensating for the ionised dopants inside the structure. This layer affects the 2DEG in a similar way to a δ-doped layer, and is treated as such in the scattering rate equations:

$$\frac{1}{\tau_\delta^{surf}} = \sigma^{surf} \int_0^{\pi} d\theta (1 - cos\theta) \nu(\theta, z^{surf}) \tag{3.17}$$

3.2.3 Interfacial Roughness

During MBE growth, the AlGaAs and GaAs interface can develop slight non uniformities, leading to a 'rough' interface. The electric field that is experienced by the electrons is no longer smooth, resulting in scattering events. This interfacial roughness is described by two parameters: Δ, the amplitude of the bumps in the direction perpendicular to the interface, and Λ, the lateral correlation length between the bumps. The deviation, $\Delta(r)$ is assumed to follow a Gaussian

[1]The heterointerface is set at z=0.

distribution such that

$$< \Delta(r)\Delta(r') >= \Delta^2 e^{-(r-r')^2/\Lambda^2} \tag{3.18}$$

The expression for the scattering lifetime from the interfacial roughness is:

$$\frac{1}{\tau_{IR}} = \frac{m}{\hbar^3}(\Lambda\Delta)^2 \int_0^\pi d\theta(1 - cos\theta) \left| \frac{e^2}{2\epsilon_0\epsilon_r} \frac{N}{2\epsilon(q)} \right|^2 e^{-\Lambda^2 q^2/4} \tag{3.19}$$

where

$$N = \frac{1}{2}n_{2D} + N_{depl} \tag{3.20}$$

and N_{depl} is the depletion charge density, given by

$$N_{depl} = \sqrt{2\epsilon_r\epsilon_0 N_a E_g} \tag{3.21}$$

where N_a is the acceptor concentration in the buffer layer and E_g the bandgap in GaAs. The depletion charge arises because the substrate is usually lightly p doped by impurity atoms. This changes the overall bandstructure and affects the position of the electron wavefunction.

The effect of the interfacial roughness is more dominant at the highest densities. An intuitive way of thinking about this is that as the density increases, the electrons have less freedom to move around scattering centres such as a defect in the interface. In addition, as the topgate voltage increases, the wavefunction of the electron gets pushed more against the interface. The electron wavefunction has a greater overlap with the interface and this results in increased scattering.

3.2.4 Phonon scattering

Phonons are the thermal vibrations of the lattice, and their presence can contribute to scattering events that limit mobility. The main source of phonon scattering below 100K is acoustic phonons. While these had little effect at the usual measurement temperatures of 1.5K or below [32], they have an observable effect for measurements conducted at higher temperatures. Studies have shown that the contribution to the scattering lifetime from phonons, τ_p, is proportional

to the temperature, T below approximately 70K, and proportional to $T^{5/2}$ at higher temperatures [33].

3.2.5 Alloy scattering

Alloy scattering comes from the imperfect arrangement of Al and Ga in the AlGaAs crystal. However, this is not significant in the GaAs/AlGaAs heterostructure, and is of an order of magnitude or more smaller than interface roughness scattering [34]. However, for structures where conduction occurs in a channel with a ternary alloy, such as the InGaAs channel discussed in section 3.8, alloy scattering will have a significant effect on transport[35]. It can be shown [36] that the relaxation time due to alloy scattering is

$$\frac{1}{\tau_{alloy}} \propto \frac{(1-x)}{x^{3/2}} \left(\frac{1}{2}n_{2D} + N_{depl} \right) \tag{3.22}$$

where x is the fraction of the fraction of the other material e.g. Al.

3.2.6 Modelling the density-mobility relation

Before leaving this discussion of the scattering mechanisms, it is useful to see what the various contributions do to the density-mobility relation. Fig.3.1[1] shows how the background impurity levels, interfacial roughness and surface charge densities contribute to the overall mobility in undoped 2DEGs at a GaAs/AlGaAs heterostructure. 3.1(a) shows the situation where the interface is only 30nm below the surface. In this case, the scattering from the surface states dominates the low density regime. In 3.1(b), which is calculated for a structure where the interface is 300nm from the surface, the surface states almost play no effect. Instead, the background impurities are the dominant factor at low densities while the interfacial roughness scattering dominates at higher densities.

[1]The curves are generated by calculating $1/\tau_i$ at various densities using a modelling program in C, written by Dr. Kantimay Das Gupta, who was at the Cavendish Laboratory.

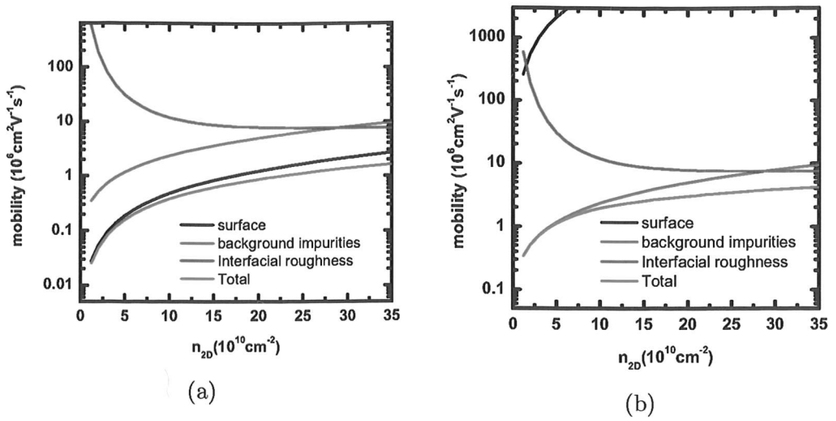

Figure 3.1: Comparing the how different scattering mechanisms limits the mobility in undoped 2DEGs at GaAs/AlGaAs heterostructures that are (a) 30nm and (b) 300nm below the surface

3.2.7 Limitations to the model

The modelling of density-mobility relations for various samples was done using the Fang-Howard wavefunction. While useful in making the calculations more straightforward, this model has the limitation that the electron wavefunction terminates at the interface. This means that the effects of any impurities in the AlGaAs would be less than in reality. In addition, alloy scattering cannot be taken into account in this model as the wavefunction does not penetrate the region where this scattering would take place.

The difference between this model and one which uses a finite barrier, with a wavefunction that can penetrate into the AlGaAs barrier[1], is illustrated in fig.3.2. Both sets of results are calculated with the same background impurity concentrations and the same interfacial roughness parameters. In the finite barrier model, the mobility is lower at higher densities as the wavefunction penetrates more into the interface and hence the scattering from impurities in the AlGaAs has a greater effect. There is also extra terms in this model that take into account alloy scattering, as well as allowing for different impurity concentrations in the region

[1]modelling program written by Dr. Andy Croxall.

of GaAs where the wavefunction penetrates and the region the wavefunction does not reach.

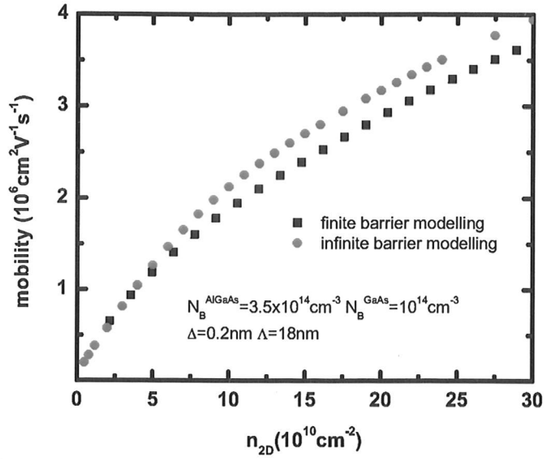

Figure 3.2: Comparing the density-mobility relation of a 300nm deep 2DEG calculated using a finite barrier model and an infinite barrier model.

While it would be desirable to have a more accurate model, ultimately, the background impurity levels, roughness parameters etc. do not have to be exact. What is important for MBE growers to produce better materials and gain improvement in experimental results is how wafer quality changes with time or growth conditions. Therefore, in most situations, as long as the same model is used in comparing samples, then it will give indications of what might be improved either in MBE growth or in experimental methods.

3.3 Characterising an MBE chamber

The cleanliness of an MBE chamber is very important to growing high quality material for experiments, and one measure of this is the background impurity levels in the MBE grown wafers. In fact, the background impurity concentration is one of the major limiting factors in achieving high mobility in 2DEGs, both doped and undoped [37]. Certain methods, such as Deep Level Transient

Spectroscopy (DLTS) [38] and Photoluminescence (PL) [39], can be used to monitor the background impurity levels. However, as the impurity concentration decreases below approximately 10^{14} cm^{-3}, these become increasingly inaccurate. As the background impurity concentrations in MBE chambers that grow the highest mobility wafers are usually below this concentration, characterising wafers using these methods is difficult.

A more accurate method is to measure the density and mobility relationship of a sample from a MBE-grown wafer. Then, using the scattering rate equations, calculate what this relation should be with certain values of background impurity concentration, doping, and interfacial roughness. The combination of values that best fit the data would yield the impurity levels in the MBE chamber, as well as providing information on interfacial roughness.

While the density-mobility relation modelling can be done for doped wafers as well as undoped wafers, the scattering in doped wafers is dominated by the intentional dopants, which are orders of magnitude more highly concentrated than the background impurities. Therefore, this technique is best used on undoped wafers, where there is only scattering from ionised background impurity atoms and the interfacial roughness, and possibly the surface states for shallow 2DEGs [40].

3.3.1 Clean up of an MBE chamber during a growth run

The MBE machine is normally maintained under ultra high vacuum conditions in order to minimise the impurity atoms incorporated into the material grown. However, when the source materials such as Ga, As run out, or a serious fault occurs, the growth chamber has to be vented. The time between when the chamber grows its first wafers to the time when the chamber has to be vented is what is known in the SP group as the growth run of the chamber. In general, the first wafers tend to incorporate higher levels of background impurities which were introduced when the chamber was vented. The levels of these impurities in the chamber drop in later wafers as the impurity atoms are covered by the growth materials and 'buried' by the growth of the first wafers.

Undoped 2DEGs are good monitors of the background impurity levels, and as

an example, the measurements of a set of three wafers from the 'V' chamber are presented. All three wafers (V535, V581, V591) had the heterointerface 300nm below the surface. V535 is grown at the beginning of a growth run, V581 grown a few months later, and V591 in the middle of a growth run, where the growth conditions are optimal. One would expect the background impurity level to drop as the chamber 'cleans up', and this is what is seen, as shown in fig.3.3, with the average background impurity level decreasing from 1.3x10^{14} cm^{-3} in V535 to a lower level of 4.9x10^{13} cm^{-3} in V591.

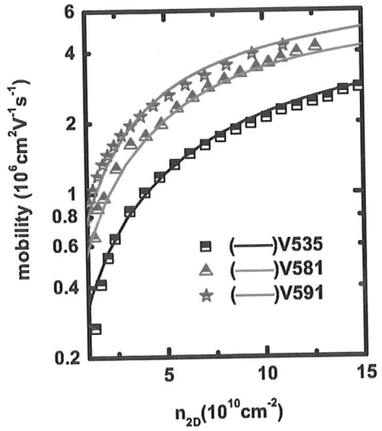

Wafer	N_B^{avg} (cm^{-3})	Δ (nm)	Λ (nm)
V535	1.3x10^{14}	0.15	16
V581	7.0x10^{13}	0.15	16
V591	4.9x10^{13}	0.15	18

Figure 3.3: The mobility vs density relation of three wafers grown at different times during the growth run of MBE chamber 'V'. The symbols are data points and the lines are calculated values with the parameters used shown in the table on the right.

3.3.2 Measuring the impurity concentrations in GaAs and AlGaAs separately

The above method allows one to measure the average background impurity level, which has contributions from $1/\tau_b^{AlGaAs}$ and $1/\tau_b^{GaAs}$. It would be useful to be able to determine the different impurity concentrations in GaAs and AlGaAs, so the growth conditions for the two materials can be optimised separately. However, it is not possible to obtain separate values for the background impurity

concentrations in GaAs and AlGaAs from one wafer. As an example, consider the density-mobility data shown in fig.3.4. It is possible to fit the data with a different combinations of values of N_B^{GaAs} and N_B^{AlGaAs}, provided the average N_B^{avg} remains the same; thus only N_B^{avg} can be determined.

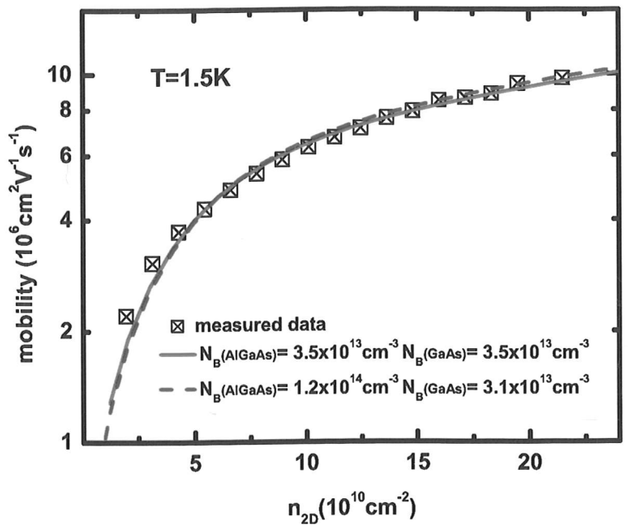

Figure 3.4: Density-mobility data for an undoped wafer with the heterointerface at 300nm below the surface. The two lines shows the calculated density-mobility relations with the parameters as shown in the legend. The roughness parameters used for both traces are Δ=0.12nm, Λ=18nm

In order to measure the background impurity concentrations of GaAs and AlGaAs separately, it is necessary to grow a set of undoped wafers in sequence, with the interface at different depths. As the chamber would be in an almost identical condition throughout the growth, the background impurity levels and the interfacial roughness should be the same. The only variable will be the thickness of the AlGaAs layer, which changes the total mobility, according to equation 3.15. The density-mobility relations for these wafers are then measured, and fits to the data calculated. The constraint is that N_B^{AlGaAs}, N_B^{GaAs}, and the interfacial roughness parameters, Δ and Λ, remain constant. Then only single

values of N_B^{AlGaAs} and N_B^{GaAs} would give a good fit to the data for the whole set of wafers.

One point to note is that the value for the surface charge density changes, increasing as the 2DEG gets closer to the surface. This is because this parameter is not an absolute value, but rather the effective surface charge that the 2DEG interacts with. This approximation simplifies the calculation for the complex structure of the device, which has multiple interfaces. (e.g. between insulator and wafer surface, between topgate and insulator, and between the substrate and the MBE layers.)

Fig.3.5(a) shows data from a set of 3 wafers from the 'A chamber', which are grown in sequence and had the heterointerface at 40, 80, and 310nm from the surface; fig.3.5(b) shows data from 3 wafers from the 'V chamber', which had the heterointerface at 30, 60 and 110nm below the surface[1]. The second set of wafers are not grown in sequence, but the chamber is nominally in the same condition. Tables 3.1 and 3.2 show the parameters used for fits to the data, showing that it is possible to extract unique values for N_B^{AlGaAs} and N_B^{GaAs} using this method.

Wafer	d(nm)	N_B^{GaAs} (cm^{-3})	N_B^{AlGaAs} (cm^{-3})	Δ (nm)	Λ (nm)	σ^{surf} (cm^{-2})
A2511	40	1.2x10^{14}	3.0x10^{14}	0.19	17.8	4.0x10^{11}
A2512	80	1.2x10^{14}	3.0x10^{14}	0.19	17.8	1.0x10^{11}
A2513	310	1.2x10^{14}	3.0x10^{14}	0.19	17.8	$\leq$ 8.0x10^{10}

Table 3.1: Fitting parameters for the 'A' chamber extracted from the density-mobility data in fig.3.5(a)

Wafer	d(nm)	N_B^{GaAs} (cm^{-3})	N_B^{AlGaAs} (cm^{-3})	Δ (nm)	Λ (nm)	σ^{surf} (cm^{-2})
V627	30	6.8x10^{13}	1.3x10^{14}	0.11	15	2.5x10^{11}
V625	60	6.8x10^{13}	1.3x10^{14}	0.11	15	10^{11}
V656	110	6.8x10^{13}	1.3x10^{14}	0.11	15	5x10^{10}

Table 3.2: Fitting parameters for the 'V' chamber extracted from the density-mobility data in fig.3.5(b)

From this analysis, the background impurity concentration in the AlGaAs was approximately three times that in GaAs, which is similar to those in [41, 42],

[1]The interface depths quoted include the standard 10nm GaAs cap.

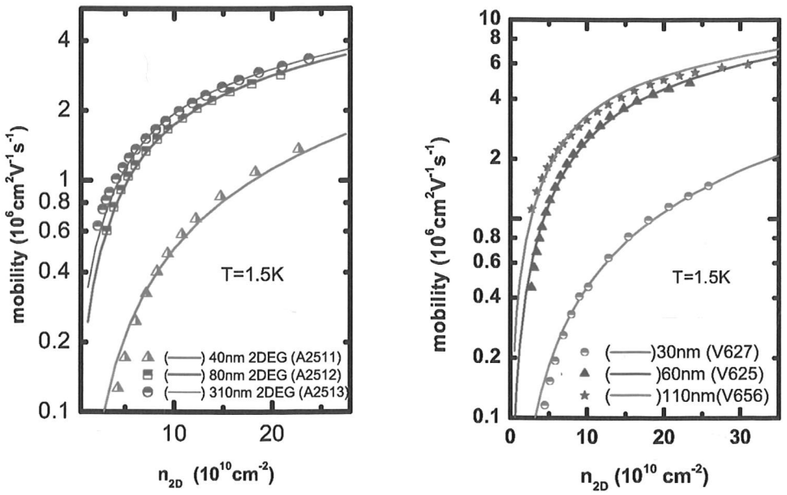

Figure 3.5: Density-mobility measurements of a set of wafers from the 'A' and 'V' MBE growth chambers. The symbols are experimental data. The lines are calculated from the same parameters for each data set, with the only change being the interface depth and the surface charge density.

and is a good indication that this technique is a simple and accurate way of determining separate values for the background impurity levels in the GaAs and AlGaAs layers in MBE-grown wafers.

The parameters obtained from the fitting show that σ^{surf} is typically in the 10^{11}cm^{-2} range for the shallowest wafers, which is an order of magnitude lower than typical dopant densities. So while the scattering from the surface charges reduces mobility in undoped wafers where the 2DEG is very close to the surface, the scattering would still be less than the of scattering from a dopant layer. This is why shallow undoped wafers can have a much improved mobility as compared to a similar doped wafer.

3.3.3 Optimisation of MBE growth conditions

In addition to monitoring the background impurity levels of an MBE chamber, undoped samples can also be used to investigate the conditions for optimal growth. These may include the growth rate or wafer structure. (Examples of growth variations can be found in refs such as [6, 43].) Some of these investigations were tried out on undoped samples. To investigate the effects of growth rate on the levels of impurities incorporated, four undoped wafers from the V chamber were grown in sequence. These wafers all had the 2DEG at 300nm below the surface, with the variations listed in table 3.6; the density-mobility relations for the set of wafers is shown in fig.3.6[1]. The 'normal' growth rate in the 'V' chamber is GaAs at 1μm per hour and AlGaAs at 0.5μm per hour, and it is useful to check whether these rates are optimum for getting good quality wafers.

The growth rate of a wafer is controlled by the temperature of the cells holding the growth materials, as well as the substrate temperature, which is controlled via the wafer holder (manipulator). Depending on the dominant source of impurities, a variation in the growth rate may affect the background impurities incorporated. If the dominant source of background impurities is the chamber, then the wafer grown at half rate would have a higher background impurity concentration, as it spent twice as long in the hot chamber; the opposite would be true for the wafer grown at twice the rate. On the other hand, if the dominant source of

[1]V594 cannot be processed, due to a large number of defects causing shorts to the gates

impurities is the cells, then the background impurity level may differ between the wafers depending on the rate the impurity atoms evaporate as compared to the primary material. For example, if the rates are more or less comparable, then there may not be a change in the background levels, whereas if the impurities evaporate slower compared to the main material at a lower temperature, then the background levels of the half-rate wafer may be lower than that of the normal rate one.

As can be seen from the density-mobility relation of the two wafers grown at normal and half rates, there is no significant difference between the two, and it is possible to fit the density-mobility relation of both with the same parameters of N_B^{avg}=5x10^{13}cm^{-3}, Δ=0.15nm, Λ=18nm. Interestingly, the two inch wafer grown at normal rate has a lower background impurity level of 3.5x10^{13}cm^{-3}, but a rougher interface, with Δ=0.25nm and Λ=15nm. While this suggests that the dominant source of impurities is less likely to be the chamber, the difference in the two inch wafer compared to the other two certainly suggests that the picture is very complex. In any case, it would mean that growing samples at a slower rate than normal does not yield any improvement in wafer mobility or decrease the levels of background impurities incorporated, supporting what is seen in ref [44].

This technique was also used to investigate other variations in wafer structure. These included whether the variation of buffer thickness can improve wafer quality and hence mobility, and whether incorporating an etch stop layer into the structure would affect mobility. The results from these two tests are shown in fig.3.7 (a) and fig.3.7 (b) respectively.

Previous studies have shown that a thicker buffer or a superlattice can improve mobility, as this removes impurity atoms from close to the conducting channel [43, 44]. However, the data from the buffer variation test seem to indicate that growing a thicker buffer does not have a significant effect on mobility, and in fact, the 3μm buffer sample has a lower mobility than the others. However, the buffer thickness was only varied from 1μm to 3μm. This variation may not reduce the background impurities enough to cause an improvement in mobility. In addition, the growth chamber was just a few months into its growth run when it produced this set of wafers, and thus the background impurity levels may be too

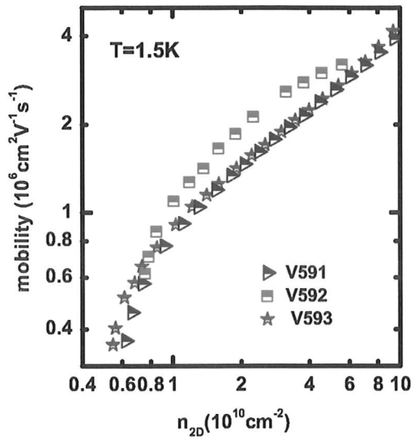

Wafer	Growth condition
V591	Control: standard 3 inch wafer
V592	Growth conditions as V591, but on a 2 inch substrate
V593	Grown at half the rate of V591
V594	Grown at twice the rate of V591

Figure 3.6: Investigating the effects of growth rate on wafer quality. In contrast to most of the samples presented in this chapter, these samples had separate gates for the ohmic contacts and the 2DEG region, allowing lower electron densities to be reached.

high for this method to yield any significant improvement. Future investigations where wafers are grown when the chamber is in an optimal condition, as well as growing much thicker buffers, such as 10μm, could yield more information about how much improvement a thicker buffer can make to wafer quality. While superlattices can help to improve mobility in doped wafers, this structure was not tested in undoped samples, as a superlattice would potentially cause parallel conduction problems. (This will be discussed in section 3.6.7.)

The comparison of two wafers with and without an etch stop layer shows that the extra layer did not adversely affect mobility. This information is useful as certain devices, such as the ultrathin undoped devices [45] require wafers with this structure. In fact, there is an improvement in the mobility of the wafer with the etch stop. Fitting the density-mobility data gives the parameters of N_B^{avg}=6x10^{13}cm^{-3},Δ=0.11nm and Λ=13nm for the sample with the etch stop (V651). For the sample with no etch stop (V656), the best fit parameters are N_B^{avg}=7.5x10^{13}cm^{-3},Δ=0.11nm and Λ=14nm. The lower background impurity concentration in V651 may be due to the more reactive Al in the etch stop layer,

which reacted with the impurities in the chamber, and the reduction in impurity concentration during the growth of the GaAs/AlGaAs layers means that the mobility of this sample is higher. However, this wafer is also slightly rougher, with the mobility saturating at similar values to V656. This may be due to the etch stop layer forming a rougher base for the growth of the GaAs and AlGaAs layers on top. Nevertheless, the differences in mobility between the two wafers is quite small, and it is possible that the differences seen are due to variations between sample cooldowns.

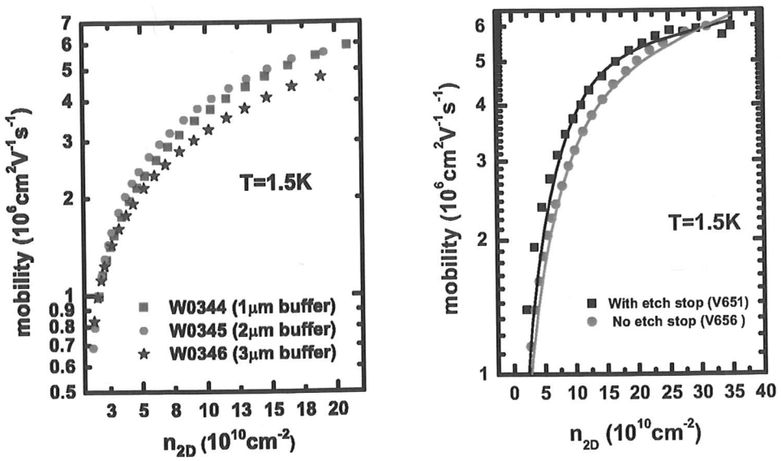

Figure 3.7: Investigating the effects of growth conditions on sample mobility. In (a), the buffer thickness was varied, and in (b), the presence/absence of an etch stop layer.

3.4 Effects of illumination

It is possible to modify the properties of compound semiconductors at low temperatures via illumination. These include changes to the carrier density and mobility, which can persist for a long time, as long as the sample is not warmed above approximately 100K. This effect is known as persistent photoconductivity

[2], and is a common technique used to vary the density in doped samples. Many studies have been conducted into this effect, and several mechanisms can explain these changes. One of the major effects of illumination on doped samples is on deep level states of the dopants, known as DX centres. The light energy can cause electrons to be released from the DX centres, which then are unable to drop back into the DX centre due to a potential barrier. These electrons then can move into the conducting channel [46]. The energy from light can also lead to the generation of free electron-hole pairs which are then separated due to the electric field in the material [47, 48]. If the temperature is low enough, the electron/holes do not recombine and the free electrons can again move into the conducting channel, resulting in a higher density, and a variation in mobility.

However, the exact effects of the illumination depend on the energy of the light. If the energy of the light is lower than the ionisation energy of the DX centres, the carrier density can decrease, as the electrons can be excited from the conducting channels, over the barrier of the DX centres and become captured [49]. For light that has sufficient energy to excite electrons out of the DX centres, the usual photoconductivity effect occurs. At even higher energies, above the bandgap of GaAs, electron-hole pair generation in the buffer region can occur [50]; the pairs then separate from each other due to the overall electric field in the crystal.

Besides enabling the study of different properties of GaAs, such as the nature of DX centres [51], illumination is also useful in other experiments. The potential to change the density and mobility of samples with this technique is often used in doped samples to optimise mobility/sample quality (e.g.[8]), especially as gated doped samples often suffer from a drop in mobility as compared to ungated samples.

3.4.1 Illumination on undoped 2DEGs

Besides acting on the dopants, illumination may also have other effects, such as activating or deactivating unintentional impurity atoms, or affecting the overall electric field in the crystal. In doped samples, these may be difficult to separate from the effects on the intentional dopants, and thus induced samples offer a

way to see what effects, if any, light has. In addition, it would be useful to investigate whether illumination can reduce the scattering potential, and hence improve mobility, in undoped samples. This may have an impact on experiments that require samples with very low disorder, such as studies of the Fractional Quantum Hall effect (discussed in section 3.6)

3.4.1.1 Experimental Method

A set of samples with a standard hall bar geometry were fabricated from three undoped wafers with the heterointerface at 60nm (W641), 110nm (W640) and 160nm (W639) from the surface. Three different depths were used to investigate whether the surface states would have any influence. These wafers were also grown on the same day; the use of this set for this experiment is to minimise any effects solely due to differences in background impurity levels.

In order for the light to shine directly on the transport region, these samples had transparent topgates, consisting of 5nm Ti capped with 1nm of gold. These samples were then cooled to 1.5K, and the density-mobility relations measured. In addition, the longitudinal and Hall resistances were also measured up to 7T at the highest density, around $3x10^{11}cm^{-2}$. The samples were then grounded, and illuminated for 465s with a red LED on full power (10mA). The density-mobility measurement was then repeated, as well as the traces to higher magnetic fields. In an initial test, a sample was illuminated for increasing lengths of time: 15s, 30s, 60s, 120s, and 240s, and the density-mobility relation measured after each illumination. The sample was not warmed up between each illumination, and thus the effect should be cumulative. However, it was found that the most obvious change in mobility occurred after the first illumination (15s) and there was little change afterwards. Thus the rest of the samples were illuminated for the same total length of time for a good comparison. This length of time is also longer than the usual illumination time (180s) for 'standard' assessments of doped wafers. In some doped wafers, 180s illumination is sufficient to cause parallel conduction, so it would be interesting to see if illumination would cause problems in an undoped wafer.

3.4.2 Changes to density-mobility relation after illumination

Fig.3.8 shows the effects of illumination on hall bars from induced 2DEGs at 60nm, 110nm and 160nm below the surface. In the 60nm deep 2DEG, there is a slight decrease in mobility after illumination, whereas there are slight increases in mobility for the 110nm and the 160nm deep 2DEGs. In all cases, there is a drop in carrier density for the same topgate voltage, i.e. it becomes harder to induce the 2DEG. This is in contrast to doped wafers, where there is usually an increase in carrier density after illumination. So how can these effects be explained? In the case of doped samples, the main effect of light seems to be on the dopants and the associated traps. Therefore, it seems surprising that an undoped sample should be affected. However, while there are no intentional dopants in induced devices, and hence no activation of deep traps, the background impurities can also be affected by light. In addition, the surface of the semiconductor can have bound states, and illumination can have effects on these. One should also consider whether there is sufficient ionisation that there is a change in the overall electric field throughout the structure, leading to a modification of the bandstructure, which may affect the scattering rates of the electrons.

The improvement of mobility in undoped heterostructures has been observed in undoped backgated samples [52, 53], where it is attributed to a decrease in the ionised background impurities. In this set of measurements, it is also possible to model the changes just by adjusting the background impurity concentration. In all three samples from W639, W640, W641, it is possible to model the dark density-mobility data with the same set of background impurity concentration parameters: N_B^{AlGaAs}= $3.3x10^{14}cm^{-3}$, N_B^{GaAs}= $1.2x10^{14}cm^{-3}$; as well as the same roughness parameters for W640 and W641: Δ=0.11nm, Λ=14nm.[1]

Assuming that the illumination made the same changes to the ionised background concentration in all three samples, it should be possible to model the density-mobility data after illumination with the same change to the values of

[1] W639 was slightly different from the other two wafers, because in order to fit the density-mobility data, one has to use a much higher roughness amplitude. W639 was the first wafer grown in that day and, for unknown reasons, the first wafer tends to be less good than subsequent ones.

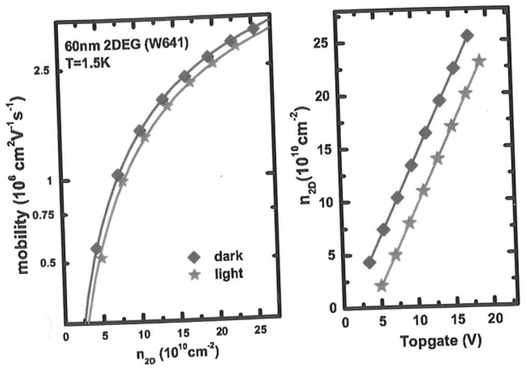

(a)

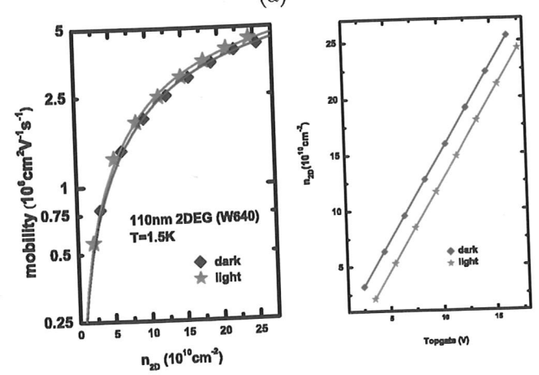

(b)

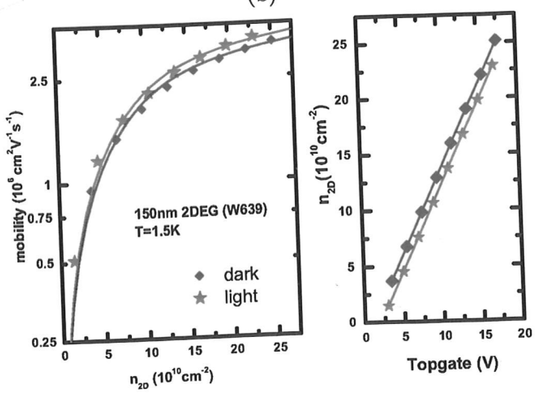

(c)

Figure 3.8: Illumination effects on undoped wafers with the heterointerface at (a) 60nm (b) 110nm and (c)160nm below the surface. The symbols are measured data an the lines are fits with parameters as explained in the text.

N_B^{AlGaAs} and N_B^{GaAs}.

In the samples from W640, with a 110nm deep 2DEG, and W639, a 160nm deep 2DEG, it is possible to obtain a good fit to the density-mobility relation after illumination by changing the background impurity concentration to N_B^{AlGaAs}= 3.2x10^{14}cm^{-3}, N_B^{GaAs}= 1.1x10^{14}cm^{-3}. The drop in mobility in W641, a 60nm deep 2DEG, cannot be explained in the same way. However, if the surface charge density is increased in the model, then it is possible to obtain a calculated relation that fits the experimental results.

In the density versus gate voltage curves, this set of samples show a drop in density for the same gate voltage, i.e. it is harder to induce carriers. While one would expect the reduction in ionised background impurities to enable carriers to be induced more easily, this is not the observed effect, and is in contrast to the results observed by [52]. However, as their devices are induced from the bottom, there is no insulator between the light source and the conducting channel. It is possible that in the top induced devices used in this experiment, the light has charged the insulator, such that it shifts the density versus gate voltage curve, and that this shift is separate from any effects seen in the mobility. In section 3.5, I will present more results showing that a shift in the density versus gate voltage curve does not necessarily lead to a change in the density-mobility relation, and that the charging up of the insulator is the most likely cause in the shift in the density versus topgate voltage curve.

One aspect to note is that the illumination has not caused parallel conduction in the undoped samples. An example of a sweep to 7T both before and after illumination in an undoped sample is shown in fig.3.9. The SdH oscillations go to zero, indicating that there is no parallel conduction. This is true for all the samples measured in this experiment. In doped wafers, illumination can cause the dopants to form a parallel conducting layer. This effect can be a serious problem in high mobility wafers with very high doping concentrations. However, induced devices do not suffer from this as the concentration of unintentional dopants are at least three orders of magnitude or more smaller than typical doping concentrations.

Wafer	d(nm)	N_B^{GaAs} (cm^{-3})	N_B^{AlGaAs} (cm^{-3})	Δ (nm)	Λ (nm)	σ^{surf} (cm^{-2})
W641	60	1.2x10^{14}	3.3x10^{14}	0.11	14	1.7x10^{11}
W640	110	1.2x10^{14}	3.3x10^{14}	0.11	14	3x10^{10}
W639	160	1.2x10^{14}	3.3x10^{14}	0.15	14	10^{10}

Table 3.3: Fitting parameters for the density-mobility relation in the 'dark' data for W639, W640 and W641

Wafer	d(nm)	N_B^{GaAs} (cm^{-3})	N_B^{AlGaAs} (cm^{-3})	Δ (nm)	Λ (nm)	σ^{surf} (cm^{-2})
W641	60	1.1x10^{14}	3.2x10^{14}	0.11	14	2.7x10^{11}
W640	110	1.1x10^{14}	3.2x10^{14}	0.11	14	3x10^{10}
W639	160	1.1x10^{14}	3.2x10^{14}	0.15	14	10^{10}

Table 3.4: Fitting parameters for the density-mobility relation in the 'light' data for W639, W640 and W641

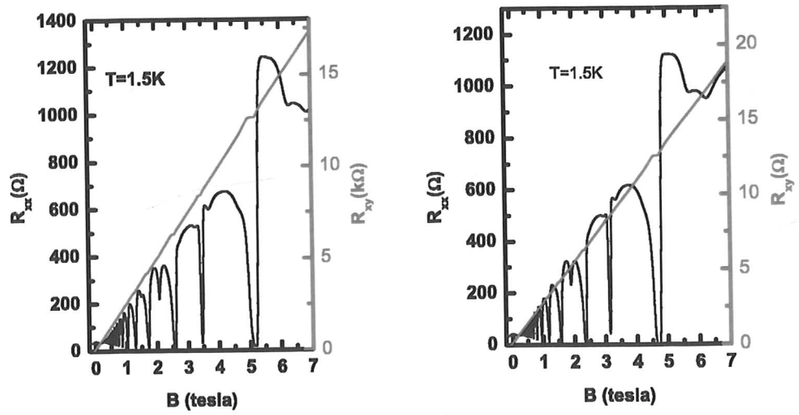

(a) (b)

Figure 3.9: Sweeps to higher magnetic fields in an undoped sample (W639) before (a) and after (b) illumination. The topgate is held at 17V for both traces. The slight shift in position of the SdH minima and the Hall plateaus after illumination is due to the decrease in carrier density.

3.4.3 Further investigations

This series of experiments with illumination on undoped 2DEGs has shown that red light does not have a large effect on 2D transport where there are no intentional dopants, and the small change in mobility can be explained by a change in background impurity levels. Nevertheless, it is worth extending this experiment to other wavelengths of light, as higher or lower energy photons may have very different effects on an undoped 2DEG. For example, one may find that only a small range of wavelength is relevant in changing the mobility, if the background impurities are not affected by the other wavelengths.

A set of experiments on samples with a different insulator such as SiO_2 will also be useful to isolate which effects come from the insulator; if very similar results are reproduced in samples with SiO_2 as the insulator, one can have confidence that the changes in mobility are not due purely to the insulator. In addition, the polyimide used in the above set of samples was also of the order of 1μm thick, and may have absorbed more of the energy from the light than a thinner insulator would, and a test of the effects of illumination with a thinner insulator would give more information on how undoped samples are affected.

3.5 Bias cooldown

Many studies have been conducted into the effects of bias cooling on semiconductor devices. Most of these have been on doped, mesoscopic samples, and they focus mainly on how bias cooling can affect RTS (random telegraph signal) noise in these devices. However, bias cooldown experiments have also been performed in two dimensional doped samples [54, 55, 56]. It was observed that while positive bias has no effect, a large negative bias has an adverse effect on sample mobility, with the largest decrease in mobility at lower densities. These effects were attributed to the bias removing the DX centres, and the charge on the donors are no longer screened. The modification to the scattering potential results in the change in the mobility of the sample.

3.5.1 Bias cooldown on undoped samples

In an undoped sample, there are no intentional dopants and hence the results of an experiment on bias cooldown could be quite different to those of doped samples. There are two different regimes where a bias cooldown of an induced device can have effects. Biasing the topgate during cooldown, the 2DEG is affected, and the effects can be investigated via measuring density-mobility relation of the sample under different biases. The other regime is effects on mesoscopic transport. This is done via biasing the surface gates defining the mesoscopic device. Both these regimes were investigated, and the effects of bias cooling on the 2DEG are presented below, whereas the effects of bias cooling on mesoscopic devices are presented in section 4.5.

3.5.1.1 Experimental details

To investigate the effects of bias cooling on a large area, a series of bias cooldowns was performed on a set of samples fabricated from undoped wafers with the heterointerface at three different depths: 60nm (W641), 110nm (W640), 160nm (W639). From each wafer, samples with either polyimide or SiO_2 as insulator were made. In addition, these samples were processed together to minimise any differences that may be introduced during the processing stages.

During cooldown from room temperature, a voltage was applied to the topgate with a SMU with a compliance level set to 5nA to prevent a high current flow which would destroy the sample. The leakage current at room temperature is sufficiently high that the full voltage was not applied. However, as the sample cools, the leakage current drops and the SMU automatically supplied a higher voltage until the set voltage is applied. The voltage applied by the SMU usually reaches the set value when the sample cools to around 200K, even for the highest bias voltages.

Each sample was cooled several times with different voltages applied on the topgate, including those considered as 'high' (a voltage sufficient to induce a 2DEG is the sample was below 4K), or 'low' (insufficient to induce a 2DEG even if the sample was below 4K). The first measurement trace was always done with zero bias to characterise the sample. On subsequent cooldowns, positive and

negative voltages were applied alternatively.

3.5.2 Effects on the insulator

An induced device always require an insulator between the topgate and the surface of the wafer, and the voltage applied during bias cooldowns could affect the insulator. The insulator could have charged up, and the resultant electric field from the insulator may affect the 2DEG.

Figures 3.10 and 3.11 illustrate the effect of the bias cooling on the insulator. The density vs topgate voltage trace moves more positive (negative) for a greater positive (negative) bias voltage, suggesting that the voltage caused charge to accumulate on the insulator on cooldown. However, the slope of the traces, which corresponds to the capacitance of the insulator, has not shifted, suggesting that the properties of the insulator have not changed. In addition, for each wafer, samples with different insulators (polyimide and SiO2) were measured to check for any effects the insulator may have introduced. In the following discussion, it will be shown that the effects (both in the density vs topgate relation and in the density-mobility relation) bias cooling has on samples with either insulator are very similar, and therefore it is likely that bias cooling has an effect on the GaAs crystal itself.

3.5.3 Effects on mobility

In all the samples measured, it was found that the density-mobility curve showed little change if either a 'low' voltage (positive or negative) or a negative 'high' voltage was applied on cooldown. However, if a 'high' positive voltage was applied, the mobility decreased significantly, especially at high electron densities. This seems to indicate that the interfacial roughness scattering, which has a dominant effect at higher densities, has increased. While it is not possible to change the roughness correlation length and amplitude, these being characteristics fixed during MBE growth, it is possible to freeze in an electric field during the cooldown, which could tilt the bandstructure. If the electron wavefunction is tilted closer to the GaAs/AlGaAs interface, the roughness scattering will increase, resulting in a drop in mobility. This effect is not dependent on whether the insulator is

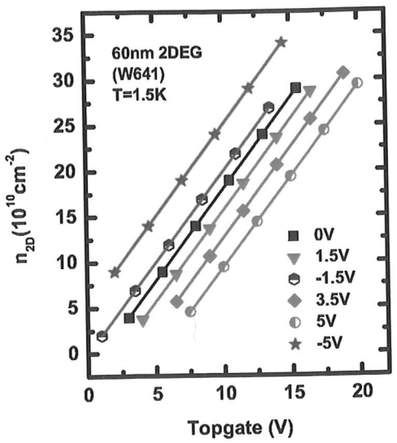

(a)

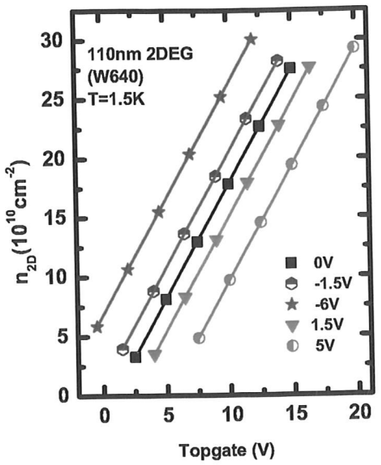

(b)

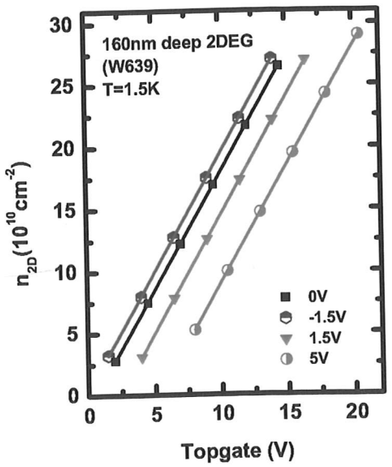

(c)

Figure 3.10: The density versus topgate voltage relation for different bias applied to the topgate during cooldown. This set of samples had polyimide as the insulator. The depths of the 2DEGs are: (a) 60nm, (b) 110nm, and (c) 160nm. The symbols are data and the lines are from a least squares fit. In sample (c), it was not possible perform a measurement after a 'high' negative voltage (-5V) was applied during cooldown due to the ohmics freezing out. This may be due to the charge built up in the polyimide insulator screening the topgate.

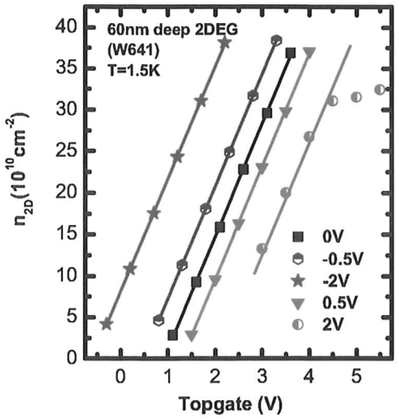

(a)

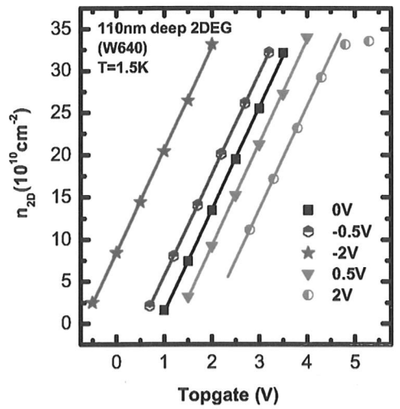

(b)

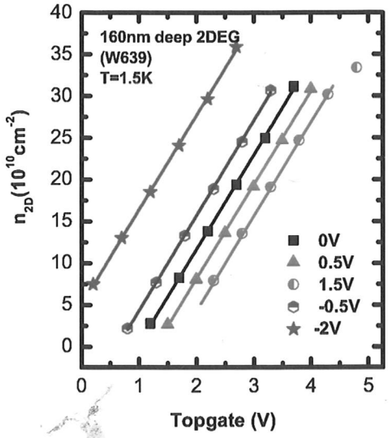

(c)

Figure 3.11: The density versus topgate voltage relation for different bias applied to the topgate during cooldown, with (a) the results from a 60nm deep 2DEG, (b) 110nm deep 2DEG, (c) 160nm deep 2DEG. The symbols are data and the lines are from a least squares fit. This set of samples had SiO_2 as the insulator. In the data for the 2V bias cooldown, the density versus topgate voltage relation in no longer linear above ~4V. This is a characteristic of the insulator. See section 2.4.5 (p.23) for a discussion of this.

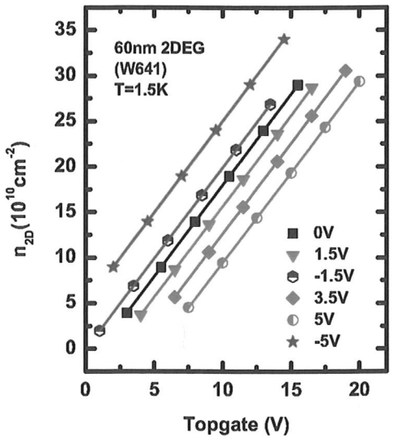

(a)

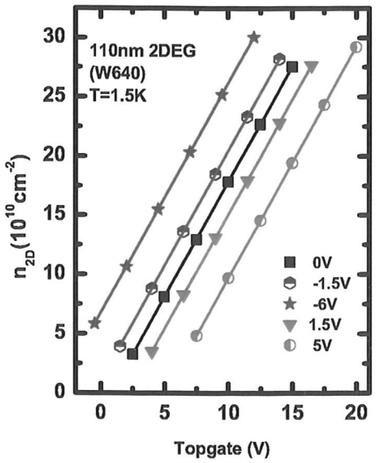

(b)

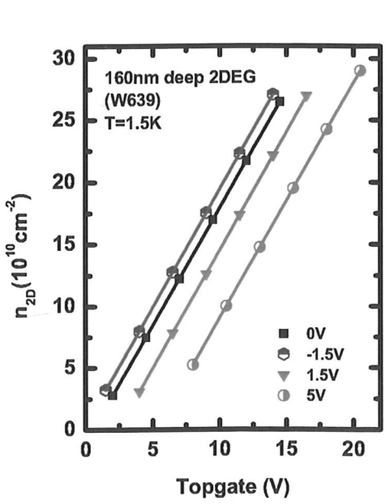

(c)

Figure 3.10: The density versus topgate voltage relation for different bias applied to the topgate during cooldown. This set of samples had polyimide as the insulator. The depths of the 2DEGs are: (a) 60nm, (b) 110nm, and (c) 160nm. The symbols are data and the lines are from a least squares fit. In sample (c), it was not possible perform a measurement after a 'high' negative voltage (-5V) was applied during cooldown due to the ohmics freezing out. This may be due to the charge built up in the polyimide insulator screening the topgate.

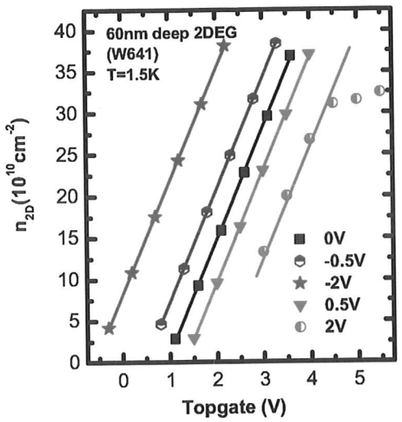

(a)

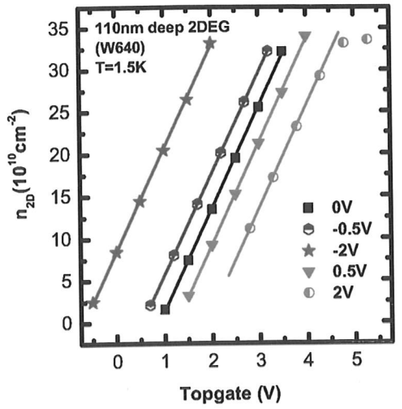

(b)

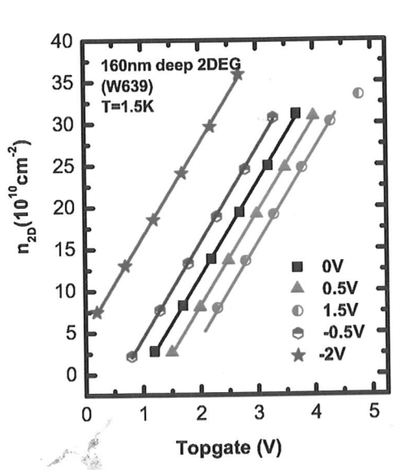

(c)

Figure 3.11: The density versus topgate voltage relation for different bias applied to the topgate during cooldown, with (a) the results from a 60nm deep 2DEG, (b) 110nm deep 2DEG, (c) 160nm deep 2DEG. The symbols are data and the lines are from a least squares fit. This set of samples had SiO_2 as the insulator. In the data for the 2V bias cooldown, the density versus topgate voltage relation in no longer linear above ~4V. This is a characteristic of the insulator. See section 2.4.5 (p.23) for a discussion of this.

polyimide or SiO_2, suggesting that it is not due solely to the surface states or a particular property of the insulator.

It is possible to model the effects of the bias cooldown on the 2DEG just by changing a single parameter, the depletion field N_{depl}. Figures 3.12, 3.13, 3.14 show how the density-mobility relation for induced 2DEGs at different depths are affected after bias cooldown. The symbols are the measured data, and the lines are calculated values using the model described in section 3.2. The same parameters are used for all the fitting curves, with the exception of N_{depl} in the interfacial roughness term. While one may argue that the bias voltage may have affected background impurities or the surface charges, it was not possible to model the change in mobility by varying the background impurity concentration alone. In addition, if there is an effect on the surface charge, any changes seen would be enhanced in the 60nm deep 2DEG. However, there is no significant difference in the decrease in mobility of the 60nm 2DEGs as compared to the deeper ones. Thus the change in the bandstructure is the most likely explanation for the effects seen.

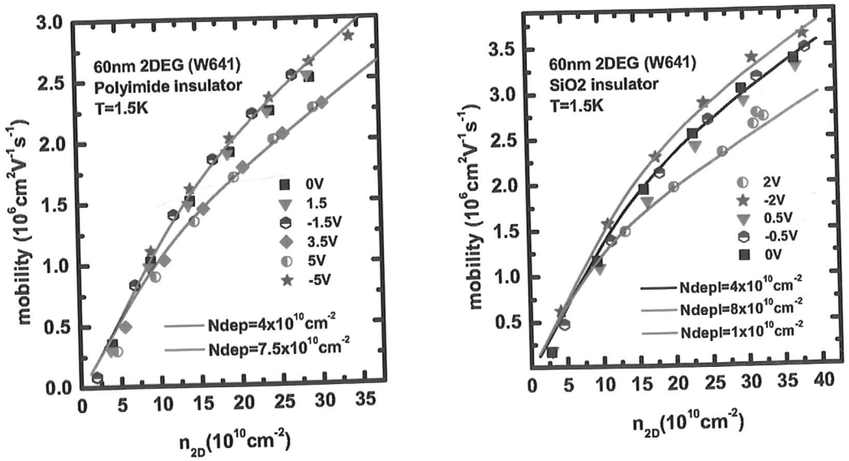

Figure 3.12: Effects of bias cooldown on the density-mobility relation of 60nm deep undoped 2DEGs.

From this set of results, one can see the cooldown routine can have effects on electron transport of undoped samples, even if the 2DEG does not exist during

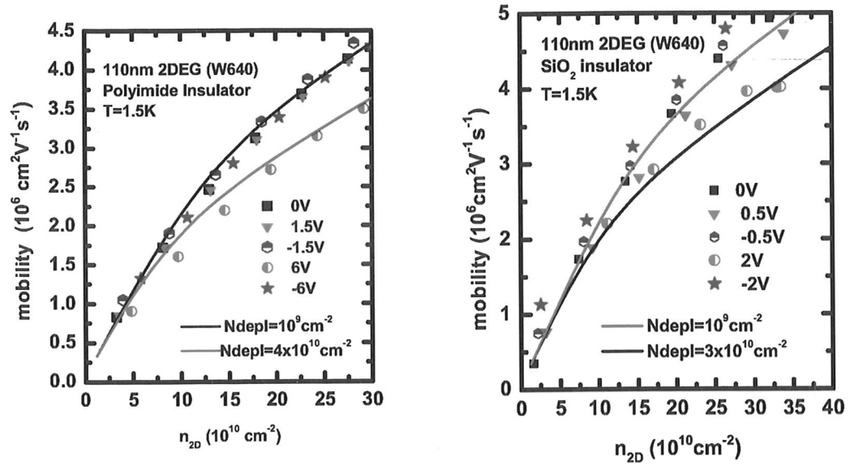

Figure 3.13: Effects of bias cooldown on the density-mobility relation of 110nm deep undoped 2DEGs.

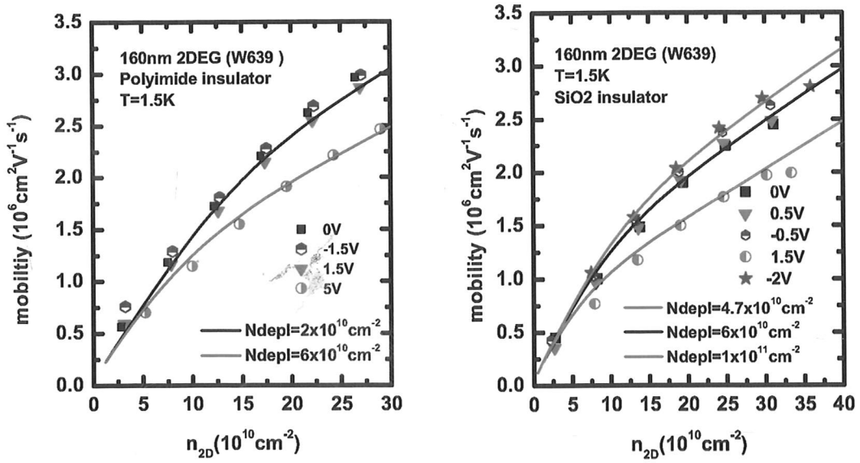

Figure 3.14: Effects of bias cooldown on the density-mobility relation of 160nm deep undoped 2DEGs.

the cooldown process[1]. With SiO_2, a -2V bias appears to cause a small (~10%) gain in mobility in all three wafers studied, whereas there seems to be no improvement in mobility in the polyimide samples for high negative voltages. While this experiment indicates that bias cooling of the 2DEG cannot improve mobility significantly, this technique opens the possibility of modifying the bandstructure of the overall crystal, which may be useful in improving measurements in other ways, for example by removing a parallel conducting layer.

It would also be interesting to investigate whether it is possible to reverse the effects of bias cooling by illuminating the sample. In doped samples, illumination can undo the effects of a bias cool, and one may expect this to happen for undoped samples as well. However, as bias cooling also changes the insulator, which has effects on the 2DEG formed, illumination may not be able to completely undo the effects of bias cooling in an undoped sample .

3.6 The Quantum Hall and Fractional Quantum Hall Effect

3.6.1 Magnetotransport in high magnetic fields

To explain effects seen in electron transport in higher fields, such as the quantum hall effect, a quantum mechanical treatment of the electron transport has to be used. For an electron system confined to two dimensions (the xy plane) in a magnetic field perpendicular to the plane, $B\hat{z}$, the Schroedinger equation can be written as

$$\frac{1}{2m^*}(\mathbf{p} + e\mathbf{A})^2\Phi = E\Phi \tag{3.23}$$

The magnetic vector potential $\mathbf{A}$ obeys the relation $\mathbf{B}=\nabla$ x $\mathbf{A}$. As the magnetic field is perpendicular to the plane of the electrons, the equation can be solved by using the Landau gauge, where $\mathbf{A}$= (0, Bx, 0), and the wavefunction Φ =

[1]Some of the higher positive applied voltages, e.g. 5V, are sufficient to generate a 2DEG at temperatures below approximately 10K, but at higher temperatures no well defined 2DEG can be found. See section 3.8.2 for a discussion of the dependence of 2DEG formation on temperature.

$f(x)exp(iky)$.The quantised energy levels then have values of

$$E_{n,l} = (n + \frac{1}{2})\hbar\omega_c \tag{3.24}$$

where ω_c is the cyclotron frequency and is equal to $|eB/m^*|$. This means that the density of states of the 2D system is split into a series of discrete values, spaced $\hbar\omega_c$ apart. These are known as Landau levels. The number of occupied Landau levels, ν, at a magnetic field B and an electron density of n_{2D} is given by

$$\nu = \frac{hn_{2D}}{eB} \tag{3.25}$$

In the ideal case, the Landau levels are delta functions in energy, separated by $\hbar\omega_c$, as illustrated in fig.3.15 (a). In this case, all the states in the same level are degenerate in energy . However, the disorder in real samples mean that not all the states in the same Landau level have the same energy, and each Landau level is broadened, as illustrated in fig.3.15(b). At the centre of each Landau level are the extended states, in which transport can take place throughout the sample. Towards the 'tails' of the Landau levels are the localised states, in which most electrons are confined to small regions in the sample and cannot take part in transport.

3.6.2 Shubnikov de-Haas Oscillations

The Shubnikov de-Haas (SdH) effect is a series of oscillations in the longitudinal resistance of a two-dimensional conducting layer as the perpendicular magnetic field, B, is swept. One characteristic of these oscillations is that a minimum occurs at values of B where ν is an integer. These minima go to zero at higher magnetic fields, and the minima also go to zero at smaller magnetic fields at lower temperatures . The SdH oscillations can be explained using the picture of Landau levels. As the field increases, electrons move to lower Landau levels. The Fermi level shifts with the density of states, since the number of electrons is constant, and when it crosses a region between two Landau levels the density of states drops to zero. Longitudinal transport, which happens at the Fermi level, drops to zero. Thus σ_{xx}=0, and by equation 3.4, the longitudinal resistance also

the cooldown process[1]. With SiO_2, a -2V bias appears to cause a small (~10%) gain in mobility in all three wafers studied, whereas there seems to be no improvement in mobility in the polyimide samples for high negative voltages. While this experiment indicates that bias cooling of the 2DEG cannot improve mobility significantly, this technique opens the possibility of modifying the bandstructure of the overall crystal, which may be useful in improving measurements in other ways, for example by removing a parallel conducting layer.

It would also be interesting to investigate whether it is possible to reverse the effects of bias cooling by illuminating the sample. In doped samples, illumination can undo the effects of a bias cool, and one may expect this to happen for undoped samples as well. However, as bias cooling also changes the insulator, which has effects on the 2DEG formed, illumination may not be able to completely undo the effects of bias cooling in an undoped sample .

3.6 The Quantum Hall and Fractional Quantum Hall Effect

3.6.1 Magnetotransport in high magnetic fields

To explain effects seen in electron transport in higher fields, such as the quantum hall effect, a quantum mechanical treatment of the electron transport has to be used. For an electron system confined to two dimensions (the xy plane) in a magnetic field perpendicular to the plane, $B\hat{z}$, the Schroedinger equation can be written as

$$\frac{1}{2m^*}(\mathbf{p} + e\mathbf{A})^2\Phi = E\Phi \tag{3.23}$$

The magnetic vector potential **A** obeys the relation $\mathbf{B}=\nabla$ x **A**. As the magnetic field is perpendicular to the plane of the electrons, the equation can be solved by using the Landau gauge, where **A**= (0, Bx, 0), and the wavefunction Φ =

[1]Some of the higher positive applied voltages, e.g. 5V, are sufficient to generate a 2DEG at temperatures below approximately 10K, but at higher temperatures no well defined 2DEG can be found. See section 3.8.2 for a discussion of the dependence of 2DEG formation on temperature.

$f(x)exp(iky)$.The quantised energy levels then have values of

$$E_{n,l} = (n + \frac{1}{2})\hbar\omega_c \tag{3.24}$$

where ω_c is the cyclotron frequency and is equal to $|eB/m^*|$. This means that the density of states of the 2D system is split into a series of discrete values, spaced $\hbar\omega_c$ apart. These are known as Landau levels. The number of occupied Landau levels, ν, at a magnetic field B and an electron density of n_{2D} is given by

$$\nu = \frac{hn_{2D}}{eB} \tag{3.25}$$

In the ideal case, the Landau levels are delta functions in energy, separated by $\hbar\omega_c$, as illustrated in fig.3.15 (a). In this case, all the states in the same level are degenerate in energy . However, the disorder in real samples mean that not all the states in the same Landau level have the same energy, and each Landau level is broadened, as illustrated in fig.3.15(b). At the centre of each Landau level are the extended states, in which transport can take place throughout the sample. Towards the 'tails' of the Landau levels are the localised states, in which most electrons are confined to small regions in the sample and cannot take part in transport.

3.6.2 Shubnikov de-Haas Oscillations

The Shubnikov de-Haas (SdH) effect is a series of oscillations in the longitudinal resistance of a two-dimensional conducting layer as the perpendicular magnetic field, B, is swept. One characteristic of these oscillations is that a minimum occurs at values of B where ν is an integer. These minima go to zero at higher magnetic fields, and the minima also go to zero at smaller magnetic fields at lower temperatures . The SdH oscillations can be explained using the picture of Landau levels. As the field increases, electrons move to lower Landau levels. The Fermi level shifts with the density of states, since the number of electrons is constant, and when it crosses a region between two Landau levels the density of states drops to zero. Longitudinal transport, which happens at the Fermi level, drops to zero. Thus σ_{xx}=0, and by equation 3.4, the longitudinal resistance also

the cooldown process[1]. With SiO_2, a -2V bias appears to cause a small (~10%) gain in mobility in all three wafers studied, whereas there seems to be no improvement in mobility in the polyimide samples for high negative voltages. While this experiment indicates that bias cooling of the 2DEG cannot improve mobility significantly, this technique opens the possibility of modifying the bandstructure of the overall crystal, which may be useful in improving measurements in other ways, for example by removing a parallel conducting layer.

It would also be interesting to investigate whether it is possible to reverse the effects of bias cooling by illuminating the sample. In doped samples, illumination can undo the effects of a bias cool, and one may expect this to happen for undoped samples as well. However, as bias cooling also changes the insulator, which has effects on the 2DEG formed, illumination may not be able to completely undo the effects of bias cooling in an undoped sample .

3.6 The Quantum Hall and Fractional Quantum Hall Effect

3.6.1 Magnetotransport in high magnetic fields

To explain effects seen in electron transport in higher fields, such as the quantum hall effect, a quantum mechanical treatment of the electron transport has to be used. For an electron system confined to two dimensions (the xy plane) in a magnetic field perpendicular to the plane, $B\hat{z}$, the Schroedinger equation can be written as

$$\frac{1}{2m^*}(\mathbf{p} + e\mathbf{A})^2\Phi = E\Phi \tag{3.23}$$

The magnetic vector potential $\mathbf{A}$ obeys the relation $\mathbf{B}=\nabla$ x $\mathbf{A}$. As the magnetic field is perpendicular to the plane of the electrons, the equation can be solved by using the Landau gauge, where $\mathbf{A}$= (0, Bx, 0), and the wavefunction Φ =

[1]Some of the higher positive applied voltages, e.g. 5V, are sufficient to generate a 2DEG at temperatures below approximately 10K, but at higher temperatures no well defined 2DEG can be found. See section 3.8.2 for a discussion of the dependence of 2DEG formation on temperature.

$f(x)exp(iky)$.The quantised energy levels then have values of

$$E_{n,l} = (n + \frac{1}{2})\hbar\omega_c \tag{3.24}$$

where ω_c is the cyclotron frequency and is equal to $|eB/m^*|$. This means that the density of states of the 2D system is split into a series of discrete values, spaced $\hbar\omega_c$ apart. These are known as Landau levels. The number of occupied Landau levels, ν, at a magnetic field B and an electron density of n_{2D} is given by

$$\nu = \frac{hn_{2D}}{eB} \tag{3.25}$$

In the ideal case, the Landau levels are delta functions in energy, separated by $\hbar\omega_c$, as illustrated in fig.3.15 (a). In this case, all the states in the same level are degenerate in energy . However, the disorder in real samples mean that not all the states in the same Landau level have the same energy, and each Landau level is broadened, as illustrated in fig.3.15(b). At the centre of each Landau level are the extended states, in which transport can take place throughout the sample. Towards the 'tails' of the Landau levels are the localised states, in which most electrons are confined to small regions in the sample and cannot take part in transport.

3.6.2 Shubnikov de-Haas Oscillations

The Shubnikov de-Haas (SdH) effect is a series of oscillations in the longitudinal resistance of a two-dimensional conducting layer as the perpendicular magnetic field, B, is swept. One characteristic of these oscillations is that a minimum occurs at values of B where ν is an integer. These minima go to zero at higher magnetic fields, and the minima also go to zero at smaller magnetic fields at lower temperatures . The SdH oscillations can be explained using the picture of Landau levels. As the field increases, electrons move to lower Landau levels. The Fermi level shifts with the density of states, since the number of electrons is constant, and when it crosses a region between two Landau levels the density of states drops to zero. Longitudinal transport, which happens at the Fermi level, drops to zero. Thus σ_{xx}=0, and by equation 3.4, the longitudinal resistance also

drops to zero. The SdH minima thus offer an alternative method of estimating the electron density: from equation 3.25, a plot of ν versus 1/B will give a slope of $n_{2D}h/e$.

3.6.3 Integer Quantum Hall Effect

The classical Hall effect, in which the transverse resistance is proportional to the perpendicular magnetic field, is explained under the semi-classical transport model as discussed in section 3.1. However, as von Kltizing *et.al* discovered [57], at higher magnetic fields, magnetoresistance measurements show that the Hall resistance shows quantised plateaus at values of

$$R_H = \left(\frac{h}{e^2}\right)\frac{1}{\nu} \tag{3.26}$$

where ν is an integer, and corresponds to the number of filled Landau levels. At the same time, the longitudinal resistance goes to zero at low temperatures. This is known as the Integer Quantum Hall Effect (IQHE), and the quantisation of the plateaus is accurate to the order of 10^{-10}. These plateaus tend to span a wide range in field, and require an extension of the explanation of the low field Shubnikov de-Haas oscillations.

The integer quantum hall effect can be explained by a combination of the Landau levels and the Landauer-Buttiker formalism [58] which takes account of the sample edges. At fields where an integer number of Landau levels are filled, the Fermi energy is in the 'tails' of the Landau levels, where the electrons would all be in localised states, and no transport can take place. However, this only applies if the sample is infinite. In reality, the potential at the edges of the sample is slightly different, which means that the degeneracy of the Landau levels is lifted. The interaction of the electrons near the edges with the disorder potential in the sample means that the states near the edges are extended states. Equipotential lines form along the edges (i.e. the 'edge states'), and electrons can travel along these. It can be shown [59] that electrons can only travel in a fixed direction along these lines, and electrons travelling in different directions are spatially separated from each other, provided that the sample is large enough.

Thus there is no back scattering and the longitudinal resistance drops to zero. At the same time, as electrons cannot travel in the transverse direction, there is a finite Hall voltage. The extent of the Landau level broadening is dependent on disorder, and therefore the width of the quantum Hall plateaus would be wider for samples of lower quality.

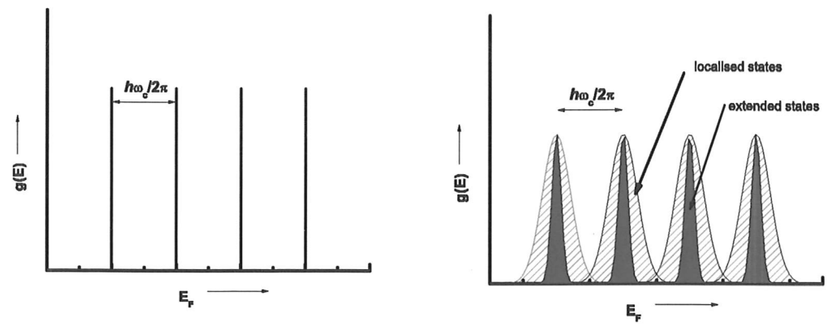

Figure 3.15: In an ideal system, the Landau levels are δ functions, as shown in (a). Due to disorder, they are broadened (b). Each broadened level has extended states where transport can take place through the whole sample, and localised states, in which transport takes place through edge states.

3.6.4 Fractional Quantum Hall Effect

As the mobility, and hence cleanliness of the material increases, and temperature decreases, it is possible to observe Fractional Quantum Hall states. In these states, the Hall plateaus are quantised at values of

$$R_{xy} = \frac{h}{e^2}\frac{1}{p/q} \tag{3.27}$$

where p and q are integers. q is an odd integer in most cases. Since the first observation of the existence of Fractional Quantum Hall states [60], the improvement in sample quality and low temperature techniques have enabled more fractional states to be observed [8].

In FQHE, the resistivity values of ρ_{xx} in the minima of the fractional states have an exponential temperature dependence of

$$\rho_{xx} \propto exp\left(\frac{-\Delta_{p/q}}{2k_BT}\right) \tag{3.28}$$

where $\Delta_{p/q}$ is the activation energy from a localised state at the Fermi level to the closest unoccupied extended state. In order to observe the fractional states, the disorder potential in the sample, as well as the thermal energy, should be smaller than $\Delta_{p/q}$. As $\Delta_{p/q}$ tend to be quite small (<1K) this means only material with very low disorder can be used in experiments, and very cold temperatures are required.

3.6.4.1 Composite fermions

To explain the FQHE, several theories which complement each other were developed, which generally include a wavefunction to solve Schroedinger's equation for the interacting electrons. The first theory was proposed by Laughlin [61], in which he proposed a wavefunction to explain the $\nu = 1/3$ FQH state. In this the interacting electron ground state has quasiparticles excitations that carry fractional charges. A further extension of this is the picture of composite fermions, which allows the FQHE to be explained in the framework of IQHE [62]. At high magnetic fields, the strong interaction between electrons results in their forming into another state where they are only weakly interacting and also experience a smaller effective magnetic field, B_{eff}. In this state, the electron quasiparticles are bound to an even integer number of magnetic flux quanta, and are known as composite fermions. The even number of flux quanta means that the fermionic nature of the electrons is not changed. By treating the composite fermions as electrons in the IQHE, one can obtain the FQHE, except that the zero of B_{eff} is now at $\nu = p/2$, where p is an integer, of the IQHE. Similar to IQHE, composite fermions form their own Landau levels, and when there is an integer number of filled composite fermion Landau levels, one can observe a plateau in the Hall resistance and a minimum/zero in the longitudinal resistance.

The effective field that composite fermions feel is given by:

$$B_{eff} = B - B_{\nu/2} \tag{3.29}$$

The effective filling factor, ν_{eff} is given by:

$$\nu_{eff} = \frac{n_{2D}h}{eB_{eff}} \tag{3.30}$$

3.6.5 The ν=5/2 Fractional Quantum Hall state

In the composite fermion picture, all the fractional states should have an odd denominator filling, ν, since an even denominator filling will correspond to a zero effective magnetic field. However, a Hall plateau has also been found corresponding to the ν=5/2 filling factor [63], requiring an extension to the description of the FQHE. The proposed explanations take into account that there may be a residual interaction remaining between the composite fermions. For example, it may be the formation of Cooper pairs of composite fermions [64]. Another possibility is Wigner crystallisation [65].

In the Cooper pairing picture of the 5/2 fractional state, theory predicts that the excitations above the ground state follow non-Abelian statistics and hence could form the qubits of a topological quantum computer [66]. The qubits are expected to be more robust and better able to maintain their entanglement for longer [67].

However, the exact nature of the 5/2 state and its excitations are still under debate as there are other theories proposed to explain the 5/2 state that correspond to particles that do not obey non-Abelian statistics. While many studies are being conducted to answer this question, challenges remain to observing the state in the first place as the excitation gap energies of the state are quite low, typically in the range of 100-200mK [68], and a maximum of 500mK [69], thus requiring very low electron temperatures and very high quality samples for experiments.

3.6.6 First signs of the ν=5/2 FQH state in an induced 2DEG sample

Experiments on the 5/2 fractional state in GaAs systems have been mainly done in doped samples, with only two reports of observing the 5/2 state in induced devices [70, 71]. Typical mobilities required for the doped samples are of the order of $2x10^7 cm^2V^{-1}s^{-1}$, with experimental temperatures of around 10mK. As induced samples do not suffer from scattering from the disorder potential from ionised dopants, it may be possible to observe the 5/2 fractional state with wafers of slightly lower mobilities and/or at higher temperatures.

To test whether a high quality undoped wafer would show Fractional Quantum Hall states, a hall bar was made on W111, which has a mobility of approximately $9x10^6 cm^2V^{-1}s^{-1}$ at an electron density of $2.5x10^{11} cm^{-2}$ at 1.5K. This sample was then cooled to 300mK and a series of magnetic field sweeps up to the $\nu = 2$ filling factor was done, with the longitudinal and hall resistances measured.

Fig.3.16 shows the results from the magnetotransport experiment. The lowest temperature trace was done at 300mK, and a dip corresponding to the 5/2 Fractional Quantum Hall state could be seen. As the dip is smeared out at a much lower temperature than the nearby fractional states and the integer quantum hall states, it is very likely that this is indeed the more 'fragile' 5/2 fraction[1]. The observation of the dip at 300mK seems to indicate that undoped samples promise to be a good system for experiments involving the 5/2 fraction.

3.6.7 Wafer structure development for very low temperature 2D transport experiments

The high mobility undoped wafer, W111, shows promising signs of enabling experiments related to Fractional Quantum Hall states, especially the 5/2 quantum hall state, to be conducted at much higher electron temperatures than those reported in the literature. However, on cooling down a hall bar from W111 to dilution fridge temperatures, it was found that at integer filling factors, such as

[1]In terms of activation energy, the integer quantum hall states have the highest activation energy. Between ν=2 and ν=3, the 7/3 and the 8/3 fractional states have higher activation energies than the 5/2. Other fractional states have lower activation energies than the 5/2.

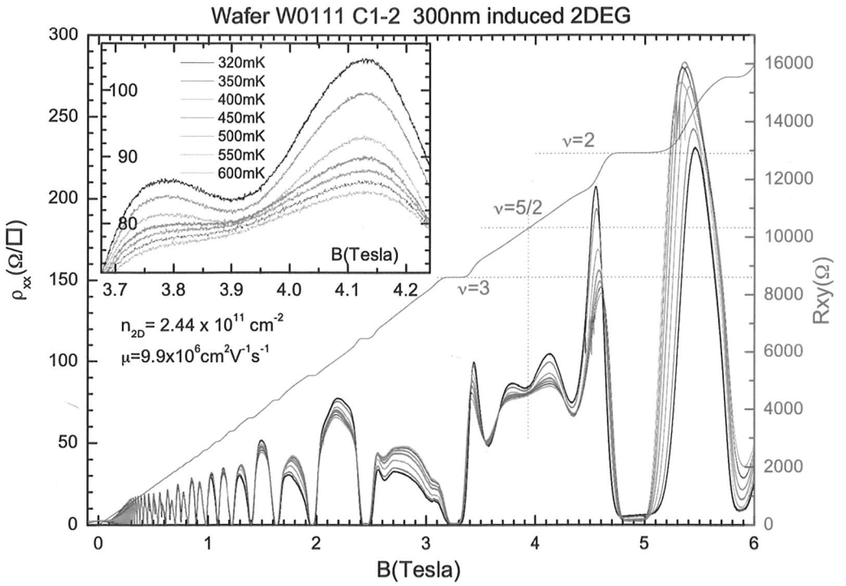

Figure 3.16: Four terminal measurement on a high mobility undoped heterostructure, showing a characteristic dip at the magnetic field corresponding to the 5/2 Fractional Quantum Hall state.

ν=2 and ν=3, the minima of the Shubnikov-de-Haas oscillations did not go to zero. In doped wafers, this would be a sign that there is parallel conduction in a separate layer. As the other layer is not at exactly the same filling factor as the 2DEG being measured, the longitudinal resistance of the parallel conducting layer is not zero, leading to a total finite resistance.

However, as there is no dopant layer in an induced wafer, can there be parallel conduction? In the process of wafer growth, there is a very thin layer of AlGaAs at the interface between the grown layers and the substrate, which is used as part of the calibration process. This layer forms a separate GaAs/AlGaAs interface that may be very weakly populated, and at the lowest temperatures, its resistance decreases sufficiently that it can conduct in parallel with the main 2DEG. This is why this problem only arises at dilution fridge temperatures ($\lesssim$ 100mK), and not at the higher temperatures ($\gtrsim$300mK) at which the sample was first assessed. However, whether this mechanism truly explains why parallel conduction like behaviour is observed is still debatable, as one would think that once the 2DEG is fully induced, it would screen the layers below from the topgate.

To attempt to correct for this problem, an undoped wafer, D120605E[1], was grown without this bottom layer of AlGaAs. Similar to W111, it has an GaAs/AlGaAs interface 300nm below the surface, and a 1μm GaAs buffer. It also has similar mobility, reaching approximately $10^7 cm^2V^{-1}s^{-1}$ at a density of $2.5x10^{11}cm^{-2}$ at 1.5K. The density-mobility relation for this sample is shown in fig.3.17. This sample was cooled down to 40mK in a dilution fridge. As fig.3.18 shows, there is no problem with parallel conduction and the Shubnikov de Haas minima at the integer filling factors reach zero. In addition, the high quality of the sample is demonstrated by the presence of many fractional states below ν=1. Thus it seems that the extra interface does form a parallel conducting layer at very low temperatures. An even more concrete proof would be to use an undoped wafer with a superlattice, where, if multiple interfaces are occupied, the parallel conduction effect may be significant enough to be observed at 1.5K.

[1]Grown by the Advanced Semiconductor Materials group at the ETH Zurich, Switzerland

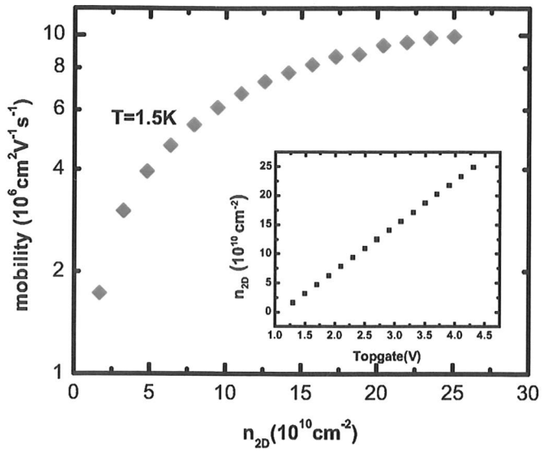

Figure 3.17: Density-mobility relation for the sample used in the experiment exploring 5/2 FQHE. Inset shows the density versus topgate relation.

3.6.8 Experiments on the 5/2 Fractional Quantum Hall state.

Using the high quality sample from D12060SE, a measurement of the activation gap ($\Delta_{5/2}$) was carried out at several densities ranging from $2.8x10^{11}cm^{-2}$ to $4x10^{11}cm^{-2}$. Although this experiment has been conducted by other groups, e.g. [68, 70], this set of measurements is a first step towards more complex experiments on the 5/2 Fractional Quantum Hall state, and as such is a 'proof of principle' to show that the processing stages and measurement set up is not detrimental to observing this state.

A four terminal measurement was carried out on a hall bar with a length to width ratio of 760μm by 140μm. A constant current of 10nA was used. This value of current was found to be the best in terms of reducing electron heating effects without losing measurement accuracy due to noise. Figure 3.19 shows the longitudinal and hall measurements at density $3.3x10^{11}cm^{-2}$. There is a clear dip in the longitudinal resistance corresponding to the 5/2 filling factor as well as an inflection point in the Hall resistance. Fig.3.20(a) shows how the 5/2 dip in the

ν=2 and ν=3, the minima of the Shubnikov-de-Haas oscillations did not go to zero. In doped wafers, this would be a sign that there is parallel conduction in a separate layer. As the other layer is not at exactly the same filling factor as the 2DEG being measured, the longitudinal resistance of the parallel conducting layer is not zero, leading to a total finite resistance.

However, as there is no dopant layer in an induced wafer, can there be parallel conduction? In the process of wafer growth, there is a very thin layer of AlGaAs at the interface between the grown layers and the substrate, which is used as part of the calibration process. This layer forms a separate GaAs/AlGaAs interface that may be very weakly populated, and at the lowest temperatures, its resistance decreases sufficiently that it can conduct in parallel with the main 2DEG. This is why this problem only arises at dilution fridge temperatures ($\lesssim$ 100mK), and not at the higher temperatures ($\gtrsim$300mK) at which the sample was first assessed. However, whether this mechanism truly explains why parallel conduction like behaviour is observed is still debatable, as one would think that once the 2DEG is fully induced, it would screen the layers below from the topgate.

To attempt to correct for this problem, an undoped wafer, D120605E[1], was grown without this bottom layer of AlGaAs. Similar to W111, it has an GaAs/AlGaAs interface 300nm below the surface, and a 1μm GaAs buffer. It also has similar mobility, reaching approximately $10^7 cm^2V^{-1}s^{-1}$ at a density of $2.5x10^{11}cm^{-2}$ at 1.5K. The density-mobility relation for this sample is shown in fig.3.17. This sample was cooled down to 40mK in a dilution fridge. As fig.3.18 shows, there is no problem with parallel conduction and the Shubnikov de Haas minima at the integer filling factors reach zero. In addition, the high quality of the sample is demonstrated by the presence of many fractional states below ν=1. Thus it seems that the extra interface does form a parallel conducting layer at very low temperatures. An even more concrete proof would be to use an undoped wafer with a superlattice, where, if multiple interfaces are occupied, the parallel conduction effect may be significant enough to be observed at 1.5K.

[1]Grown by the Advanced Semiconductor Materials group at the ETH Zurich, Switzerland

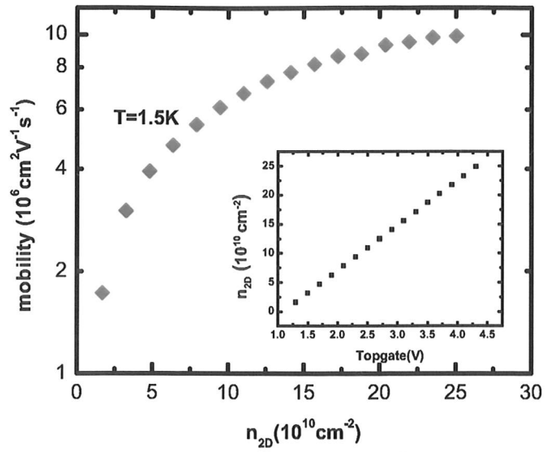

Figure 3.17: Density-mobility relation for the sample used in the experiment exploring 5/2 FQHE. Inset shows the density versus topgate relation.

3.6.8 Experiments on the 5/2 Fractional Quantum Hall state.

Using the high quality sample from D12060SE, a measurement of the activation gap ($\Delta_{5/2}$) was carried out at several densities ranging from $2.8x10^{11}cm^{-2}$ to $4x10^{11}cm^{-2}$. Although this experiment has been conducted by other groups, e.g. [68, 70], this set of measurements is a first step towards more complex experiments on the 5/2 Fractional Quantum Hall state, and as such is a 'proof of principle' to show that the processing stages and measurement set up is not detrimental to observing this state.

A four terminal measurement was carried out on a hall bar with a length to width ratio of 760μm by 140μm. A constant current of 10nA was used. This value of current was found to be the best in terms of reducing electron heating effects without losing measurement accuracy due to noise. Figure 3.19 shows the longitudinal and hall measurements at density $3.3x10^{11}cm^{-2}$. There is a clear dip in the longitudinal resistance corresponding to the 5/2 filling factor as well as an inflection point in the Hall resistance. Fig.3.20(a) shows how the 5/2 dip in the

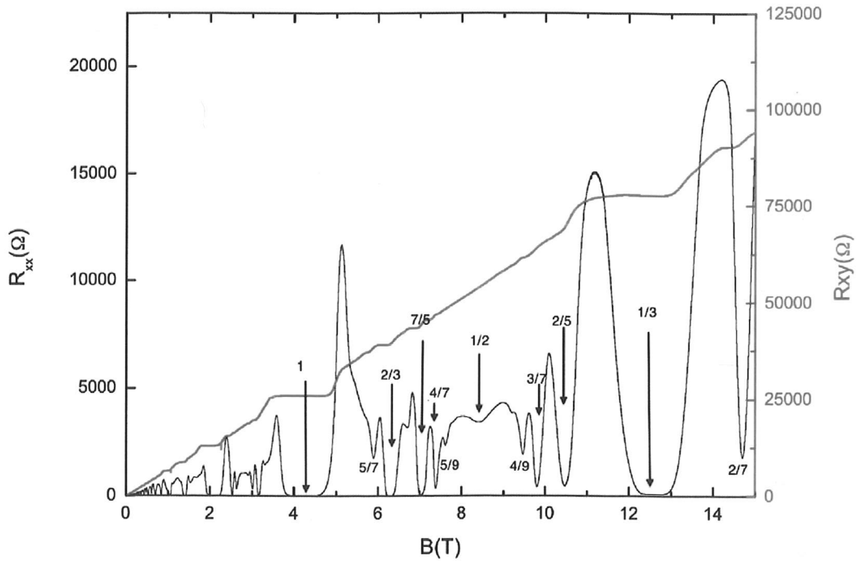

Figure 3.18: Longitudinal and Hall resistance measurements of a high mobility, undoped wafer at 30mK. The density was $9.0\text{x}10^{10}\text{cm}^{-2}$ and the mobility $8.6\text{x}10^{6}\text{cm}^{2}\text{V}^{-1}\text{s}^{-1}$.

longitudinal resistance varied as temperature increased. As expected, the depth of the dip decreases as temperature rises. No temperature variation measurement was done for the Hall measurement as there is no obvious plateau corresponding to the 5/2 FQHE.

Similar traces were taken at three other densities to measure the activation gap of the 5/2 state. The base temperature traces at these densities are shown in fig.3.20(b), with the 5/2 dip having a greater depth, due to a higher activation energy at higher densities. The density range was chosen such that the lowest density gives a noticeable dip in the longitudinal resistance corresponding to the 5/2 state, and the highest density was limited by the maximum voltage the insulator (SiO_2) can withstand before breakdown.

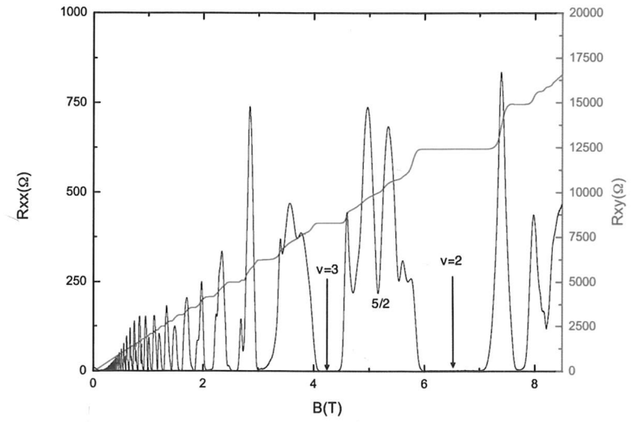

Figure 3.19: Four terminal measurement on a high mobility undoped wafer. The density was $3.3\text{x}10^{11}\text{cm}^{-2}$ and the mobility $11.5\text{x}10^{6}\text{cm}^{2}\text{V}^{-1}\text{s}^{-1}$.

$\Delta_{5/2}$ is related to the value of the longitudinal resistance at the 5/2 minimum by equation 3.28. Thus the slope of an Arrenhius plot of the temperature dependence of the 5/2 minimum will give the activation energy. The temperature dependence of the 5/2 state at four different densities was measured, and the results are presented in fig.3.21. The mobilities measured at these densities are slightly higher than one would expect if the density-mobility curve in fig.3.17

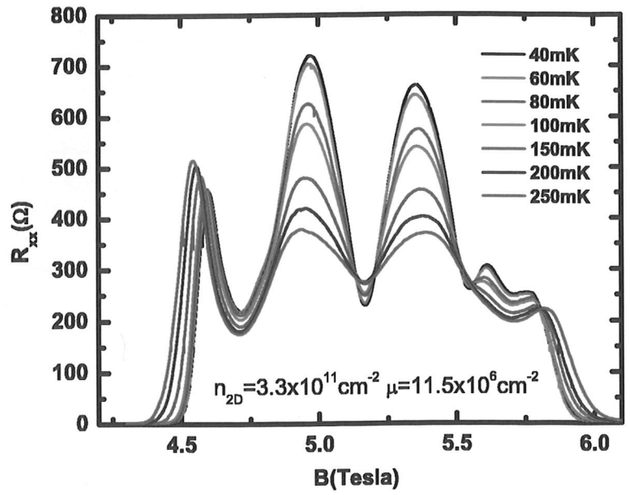

(a)

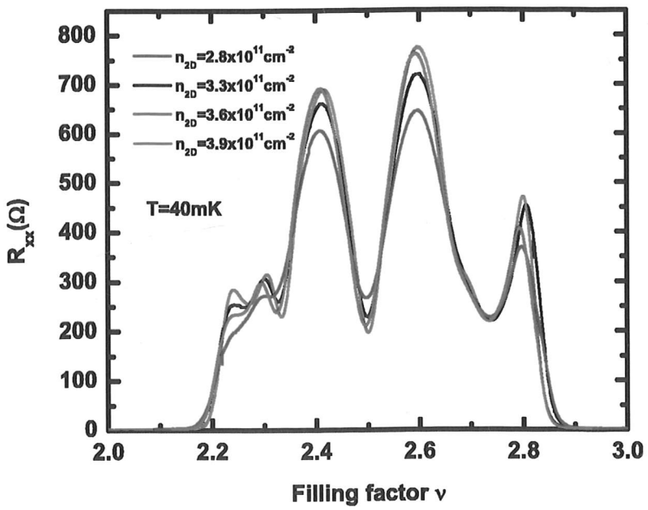

(b)

Figure 3.20: The observation of the 5/2 FQHE improves with (a) colder temperatures and (b) higher density.

is extended. This is probably due to the variation on cooldown and the slight improvement in electron mobility in going from 1.5K to 40mK.

The values obtained for the activation gap, for temperatures up to approximately 60mK, are quite small compared to most values reported in literature. However, our 5/2 minima did not reach zero, and the quoted temperatures in fig.3.21 are from the thermometer reading of the temperature in the mixing chamber of a dilution fridge, rather than the electron temperature. Therefore, the estimation of the gap energies is likely to be an underestimation. However, future work to improve the measurement set up and hall bar configuration is likely to improve the 5/2, and the other more 'fragile' Fractional Quantum Hall states observed. Electron temperatures can be reduced through optimisation of the circuit to minimise noise, using a smaller excitation current, and reducing the contact resistance further. Another possibility is to sweep the density at fixed magnetic fields, thus removing any heating from eddy currents [71].While this was tried on the sample measured, there was no improvement in the 5/2 minimum. However, this may be because the limiting obstacle to obtaining lower electron temperature is not the eddy currents, and this technique may prove useful once the other sources of electron heating have been reduced.

Another improvement that can be made is the dimensions of the Hall bar. A smaller Hall bar will sample a more uniform potential over the transport region, which could lead to a better observation of the fractional states. While the electrons should be in the diffusive transport regime[1], rather than ballistic for this experiment, at high magnetic fields, the electrons follow a cyclotron orbit, which means the edge states will not interact with each other, even if the Hall bar dimensions are too small for experiments with diffusive transport at zero magnetic field.

Another interesting possibility to explore is illumination. In section 3.4, there is a gain in mobility in deeper 2DEGs that can be attributed to a reduction in scattering from ionised background impurities. In the case of the Fractional Quantum Hall states, where a lower disorder potential is essential, illumination may very well lead to a better observation of the states, as well as higher activation

[1]For a sample with a mobility of $10^7 cm^2 V^{-1} s^{-1}$ at $2.5x10^{11} cm^{-2}$ density, the mean free path is approximately $90\mu m$.

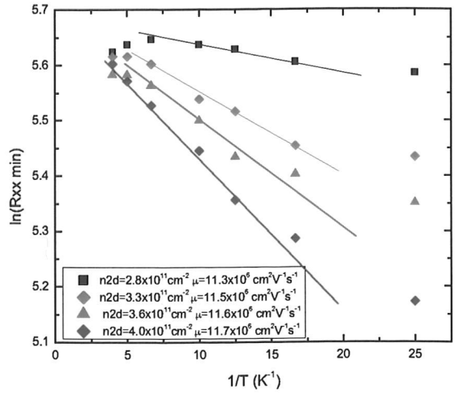

(a)

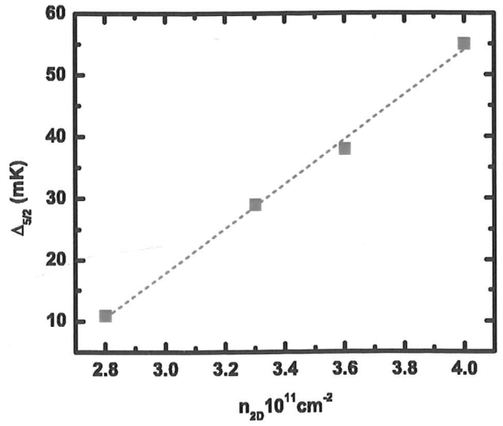

(b)

Figure 3.21: Finding the activation gap for the 5/2 FQHE: (a) Arrenhius plots for the four different densities, and (b) the activation gap energies obtained.

gaps.

3.7 The very low density regime

An area of interest in two dimensional transport is the regime where the interactions between the carriers are very strong. Predictions have been made for exotic phases such as paramagnetic and ferromagnetic liquid phases and Wigner crystals [72]. In these phases, the 2DEG changes from a conductor to an insulator. Studies have been conducted into transitions between insulating and conducting phases of a 2DEG/2DHG (e.g. [73]), as well as in other systems such as helium. However, experimental challenges remain as reaching the conditions required for the insulating phase to develop requires very high quality samples and/or low temperatures.

The interaction strength between carriers is measured by the parameter r_s, which is the ratio between the Coulomb interaction energy and the fermi energy of the system. One can express r_s as:

$$r_s = \frac{E_{e-e}}{E_F} = (n\pi)^{\frac{1}{2}} m^* \frac{e^2}{4\pi\hbar^2\epsilon} \tag{3.31}$$

Since r_s values scale with the effective mass m^*, a 2DHG would give a much stronger interaction as compared to a 2DEG of the same 2D carrier density.

Simulations have suggested that in a two dimensional electron or hole gas, the system crystallises for r_s values of around 30, with the predicted values ranging from 31±1[74] to 37±5[75]. This will correspond to a carrier density of $\lesssim$3.5x10^{8}cm^{-2} for electrons and $\lesssim$6.7x10^{9}cm^{-2} for holes. While there have been reports in literature of doped samples going to such low densities, for example 2.9x10^{9}cm^{-2} in [76], and 1.9x10^{10}cm^{-2} in [77], it is difficult to obtain such samples. The background impurity levels in these wafers would have to be very low, as the intentional dopants would already have contributed to scattering that limits the carrier transport at low densities. Undoped samples can reach these densities more easily, even if they have higher background impurity levels. For example, it was possible to obtain a low carrier density of 5x10^{9}cm^{-2} in an undoped sample (from wafer V591) with a maximum hole mobility of only

$6x10^5 cm^2V^{-1}s^{-1}$, and an electron mobility of $5x10^6 cm^2V^{-1}s^{-1}$. This is in contrast to the high mobilities required for samples on doped wafers such as [76]. Thus undoped heterostructures may offer a good way of exploring these exotic states of matter.

3.7.1 Percolation threshold

As the carrier density decreases, the potential across the 2DEG becomes less uniform due to reduced screening of the impurity potential. As a result, the 2DEG starts to break up into 'puddles', and transport occurs via percolation, where electrons jump from puddle to puddle, rather than diffusive transport (a good picture of this is given in [78]). At a critical density, n_c, at the percolation threshold, the puddles become separated sufficiently that conduction can no longer occur. Thus the percolation threshold limits the lowest density a system can reach. A sample with a higher impurity concentration has a more non-uniform potential landscape, and thus a higher n_c is more likely.

In the percolation regime, the conductivity of the electrons is predicted to follow the relation [79]

$$\sigma \propto (n - n_c)^a \tag{3.32}$$

where $a \approx 1.3$ This percolation transition can be seen in fig.3.22, where the measured mobility at the lowest density deviates from the density-mobility relation calculated from the model discussed in section 3.2. Instead, the lowest density-mobility data fit a relation where the mobility is proportional to $(n_{2D} - n_c)^{1.3}$.

3.7.2 Reaching low densities in an undoped device

There are two main challenges to reaching the lowest density: that of maintaining good ohmic contacts and the percolation threshold. With samples with one overall topgate over the ohmic region and the transport area, it was found that the sample no longer conducts below a density of approximately $2x10^{10} cm^{-2}$. However, the density-mobility curve at this density has not reached the percolation region, suggesting that it is the ohmic contacts that are no longer functioning, rather than the 2DEG reaching the percolation threshold. To reach the lowest density,

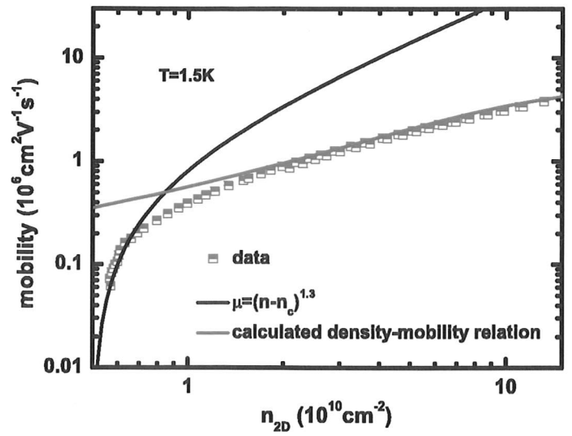

Figure 3.22: Density-mobility data from an induced wafer (V581) with the lowest density data showing a transition to a percolation regime.

a two level gating system (first developed in [28]) was used, with a central gate over the main hall bar region, close to or on the surface of the sample, and separate gate over the ohmic contacts. A slight overlap between the ohmic contact gates and the central gates enable the 2DEG to be continuous with the contacts. A higher voltage is applied to the inducing gates over the ohmic contacts to maintain a high density to ensure they work properly, whereas a much lower voltage over the central gate enables the low density ($\lesssim 10^{10} cm^{-2}$) regime to be explored.

Fig.3.23 shows the density-mobility relation in 2DHG and 2DEG samples from the same wafer. The holes have a lower mobility due to their higher effective mass, as $\mu \propto 1/m^*$. However, both were able to reach densities of less than $10^{10} cm^{-2}$, using the two level gating configuration. Fig.3.24 shows hall and longitudinal resistance measurements on these samples. While the temperature of 1.5K was too high for features such as SdH oscillations to show up, the Hall resistance is linear in field, indicating that the 2DEG/2DHG has not broken up into isolated regions.

Fig.3.25(a) shows further data from a 2DHG sample cooled down to 300mK. While it was not able to reach such a low density as the one shown in fig.3.24(b), the temperature dependence of the longitudinal resistance at the lowest density

shows an upturn at the lowest temperature, suggesting an onset of insulating behaviour. However, 300mK is not cold enough for conclusive test for the metal-insulator transition, as there are studies where the upturn changes direction on cooling from 300mK to 50mK [80]. Fig.3.25(b) shows a similar measurement on a 2DEG made from the same wafer which was able to go to lower densities.

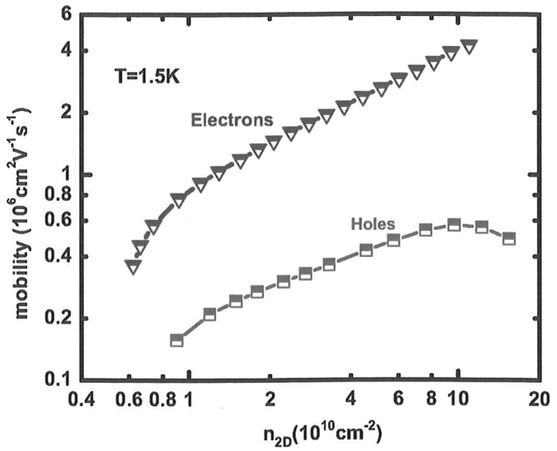

Figure 3.23: Density-mobility relation of two undoped samples made from the same wafer: one a 2DEG and the other a 2DHG. They were both able to reach a low density of 6x10^{9}cm^{-2}.

3.7.2.1 Further developments

While the induced samples measured were able to go to low densities in the 5x10^{9}cm^{-2} range, this density is higher than that required for observing zero magnetic field crystallisation in electrons, and while the sample with an induced 2DHG could reach a density corresponding to $r_s \approx 36$, the p-type ohmics did not work well at 300mK, and thus no experiments at lower temperatures could be carried out.

In order to explore insulating states of matter with induced samples, there are several improvements required: that of wafer quality, hall bar design, and

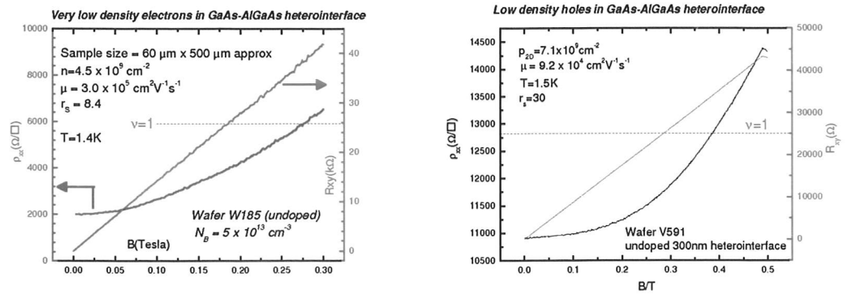

(a) (b)

Figure 3.24: Hall and longitudinal resistance measurements of (a) a 2D electron gas and (b) 2D hole gas in undoped wafers in the very low density regime.

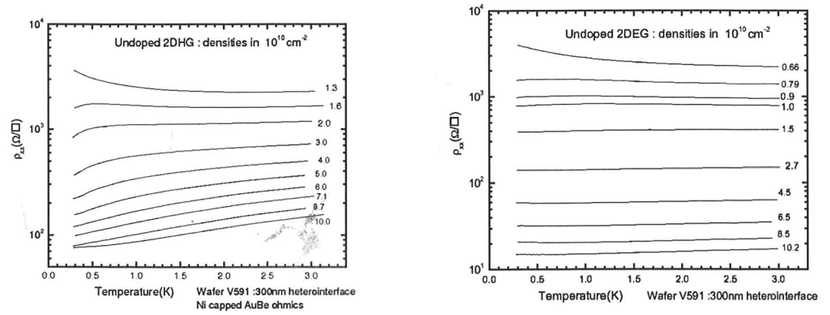

(a) (b)

Figure 3.25: Temperature dependence of the longitudinal resistance at zero magnetic field of (a) an induced 2DHG sample and (b) and induced 2DEG

optimisation of ohmics. Obtaining a high quality wafer with low disorder is required to enable samples to reach a lower density, as the percolation threshold is dependent on the disorder potential. A modification in the dimensions of the hall bar may be necessary, as a hall bar with a large area samples a more uneven potential than one with a smaller area, and thus the optimal design would be one that has as small an area as possible while carriers are still in the diffusive transport regime. Development of the processing of induced ohmics to 2DHGs would enable samples with high r_s values to be made and measured at low temperatures and higher magnetic fields for experiments.

3.8 InGaAs/GaAs undoped heterostructure

Besides GaAs/AlGaAs, other materials can also be used to form the heterostructure. The main condition is that the two materials should have different bandgaps, to form the triangular well for the 2DEG, and while a similar lattice spacing would be ideal to minimise strain in the crystal, it is not strictly necessary.

One such system, that of an AlGaAs/InGaAs/GaAs heterostructure was explored. It was of interest because InGaAs has a smaller bandgap than GaAs, and the greater difference in conduction band energies in an AlGaAs/InGaAs system means that it offers a stronger 2D confinement, and hence a potential for higher temperature operation.

The wafer used, A4185, had a structure of 100nm $Al_{0.33}Ga_{0.67}As$, 20nm $In_{0.1}Ga_{0.9}As$, and a 1μm GaAs buffer, i.e., it is an InGaAs channel rather than a true quantum well. Using the standard induced processing techniques, it was possible to obtain working hall bars from this wafer, and the following presents some of the results obtained.

3.8.1 Initial assessment

A hall bar from A4185 was first characterised at 1.5K. Fig.3.26(a) shows the density-mobility relation[1], and fig.3.26(b) the density versus gate voltage trace.

[1]The density-mobility relation is not modelled for this sample. This is because the model used for the GaAs samples presented in this chapter cannot take into account the alloy scattering, which is a dominant scattering mechanism in where the conducting channel is in InGaAs, which is a ternary alloy.

The mobility is much less than that of an undoped GaAs/AlGaAs sample. One cause of this may be the lattice spacing in InGaAs, which does not match that of GaAs/AlGaAs. As a result, there is strain in the crystal, leading to deformation. As GaAs is piezoelectric, this deformation can generate an electric field, which could result in extra scattering. The mobility also decreases as the density increases, suggesting that roughness scattering and alloy scattering, both of which increase with density, are dominant. In contrast to GaAs, alloy scattering is not negligible in this sample as the conducting channel is in the InGaAs.

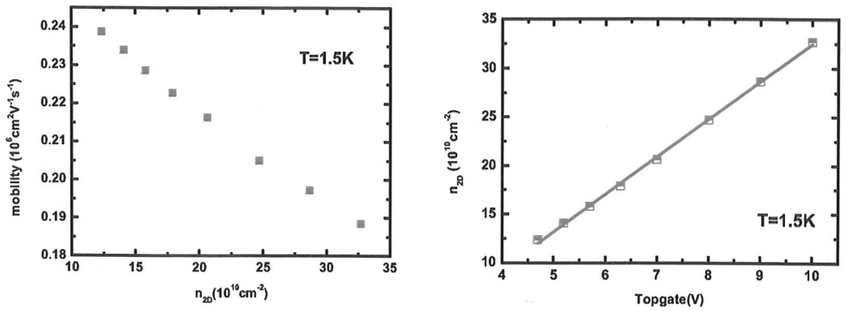

(a) (b)

Figure 3.26: (a)The density-mobility relation of the 2DEG formed in the InGaAs channel, and (b), the density versus topgate voltage trace

3.8.2 Higher temperature operation[1]

To investigate the device operation at higher temperatures, the sample was cooled down in a 1.5K cryostat with a sample heater that can raise the sample temperature up to 100K. The device was than characterised at certain temperature points from 1.5K up to 80K. As a comparison, an undoped GaAs/AlGaAs heterostructure (V651) with the interface also 100nm below the surface was characterised at the same temperatures. Both samples had the same insulator (polyimide) so as to ensure that the differences observed are due to the semiconductor material.

[1]The samples used in section 3.8.2 were made by the author. However, the temperature dependence measurements were done by Dr. Bastian Marquardt at the Cavendish Laboratory.

optimisation of ohmics. Obtaining a high quality wafer with low disorder is required to enable samples to reach a lower density, as the percolation threshold is dependent on the disorder potential. A modification in the dimensions of the hall bar may be necessary, as a hall bar with a large area samples a more uneven potential than one with a smaller area, and thus the optimal design would be one that has as small an area as possible while carriers are still in the diffusive transport regime. Development of the processing of induced ohmics to 2DHGs would enable samples with high r_s values to be made and measured at low temperatures and higher magnetic fields for experiments.

3.8 InGaAs/GaAs undoped heterostructure

Besides GaAs/AlGaAs, other materials can also be used to form the heterostructure. The main condition is that the two materials should have different bandgaps, to form the triangular well for the 2DEG, and while a similar lattice spacing would be ideal to minimise strain in the crystal, it is not strictly necessary.

One such system, that of an AlGaAs/InGaAs/GaAs heterostructure was explored. It was of interest because InGaAs has a smaller bandgap than GaAs, and the greater difference in conduction band energies in an AlGaAs/InGaAs system means that it offers a stronger 2D confinement, and hence a potential for higher temperature operation.

The wafer used, A4185, had a structure of 100nm $Al_{0.33}Ga_{0.67}As$, 20nm $In_{0.1}Ga_{0.9}As$, and a 1μm GaAs buffer, i.e., it is an InGaAs channel rather than a true quantum well. Using the standard induced processing techniques, it was possible to obtain working hall bars from this wafer, and the following presents some of the results obtained.

3.8.1 Initial assessment

A hall bar from A4185 was first characterised at 1.5K. Fig.3.26(a) shows the density-mobility relation[1], and fig.3.26(b) the density versus gate voltage trace.

[1]The density-mobility relation is not modelled for this sample. This is because the model used for the GaAs samples presented in this chapter cannot take into account the alloy scattering, which is a dominant scattering mechanism in where the conducting channel is in InGaAs, which is a ternary alloy.

The mobility is much less than that of an undoped GaAs/AlGaAs sample. One cause of this may be the lattice spacing in InGaAs, which does not match that of GaAs/AlGaAs. As a result, there is strain in the crystal, leading to deformation. As GaAs is piezoelectric, this deformation can generate an electric field, which could result in extra scattering. The mobility also decreases as the density increases, suggesting that roughness scattering and alloy scattering, both of which increase with density, are dominant. In contrast to GaAs, alloy scattering is not negligible in this sample as the conducting channel is in the InGaAs.

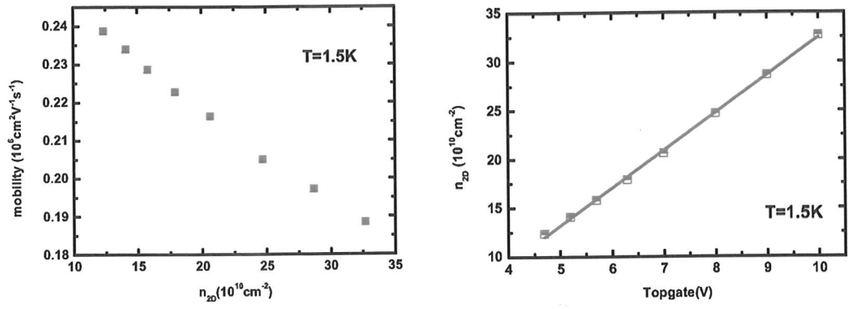

Figure 3.26: (a)The density-mobility relation of the 2DEG formed in the InGaAs channel, and (b), the density versus topgate voltage trace

3.8.2 Higher temperature operation[1]

To investigate the device operation at higher temperatures, the sample was cooled down in a 1.5K cryostat with a sample heater that can raise the sample temperature up to 100K. The device was than characterised at certain temperature points from 1.5K up to 80K. As a comparison, an undoped GaAs/AlGaAs heterostructure (V651) with the interface also 100nm below the surface was characterised at the same temperatures. Both samples had the same insulator (polyimide) so as to ensure that the differences observed are due to the semiconductor material.

[1]The samples used in section 3.8.2 were made by the author. However, the temperature dependence measurements were done by Dr. Bastian Marquardt at the Cavendish Laboratory.

optimisation of ohmics. Obtaining a high quality wafer with low disorder is required to enable samples to reach a lower density, as the percolation threshold is dependent on the disorder potential. A modification in the dimensions of the hall bar may be necessary, as a hall bar with a large area samples a more uneven potential than one with a smaller area, and thus the optimal design would be one that has as small an area as possible while carriers are still in the diffusive transport regime. Development of the processing of induced ohmics to 2DHGs would enable samples with high r_s values to be made and measured at low temperatures and higher magnetic fields for experiments.

3.8 InGaAs/GaAs undoped heterostructure

Besides GaAs/AlGaAs, other materials can also be used to form the heterostructure. The main condition is that the two materials should have different bandgaps, to form the triangular well for the 2DEG, and while a similar lattice spacing would be ideal to minimise strain in the crystal, it is not strictly necessary.

One such system, that of an AlGaAs/InGaAs/GaAs heterostructure was explored. It was of interest because InGaAs has a smaller bandgap than GaAs, and the greater difference in conduction band energies in an AlGaAs/InGaAs system means that it offers a stronger 2D confinement, and hence a potential for higher temperature operation.

The wafer used, A4185, had a structure of 100nm $Al_{0.33}Ga_{0.67}As$, 20nm $In_{0.1}Ga_{0.9}As$, and a 1μm GaAs buffer, i.e., it is an InGaAs channel rather than a true quantum well. Using the standard induced processing techniques, it was possible to obtain working hall bars from this wafer, and the following presents some of the results obtained.

3.8.1 Initial assessment

A hall bar from A4185 was first characterised at 1.5K. Fig.3.26(a) shows the density-mobility relation[1], and fig.3.26(b) the density versus gate voltage trace.

[1]The density-mobility relation is not modelled for this sample. This is because the model used for the GaAs samples presented in this chapter cannot take into account the alloy scattering, which is a dominant scattering mechanism in where the conducting channel is in InGaAs, which is a ternary alloy.

The mobility is much less than that of an undoped GaAs/AlGaAs sample. One cause of this may be the lattice spacing in InGaAs, which does not match that of GaAs/AlGaAs. As a result, there is strain in the crystal, leading to deformation. As GaAs is piezoelectric, this deformation can generate an electric field, which could result in extra scattering. The mobility also decreases as the density increases, suggesting that roughness scattering and alloy scattering, both of which increase with density, are dominant. In contrast to GaAs, alloy scattering is not negligible in this sample as the conducting channel is in the InGaAs.

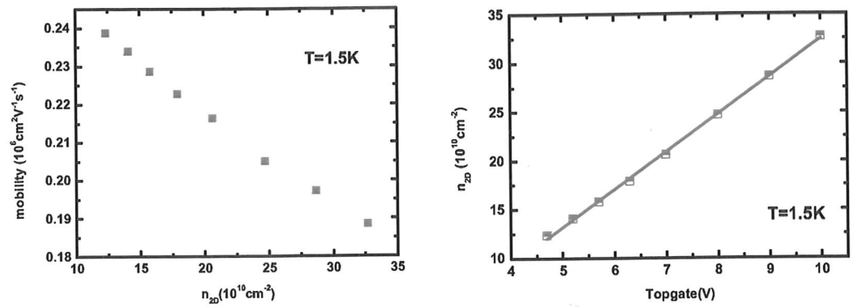

Figure 3.26: (a)The density-mobility relation of the 2DEG formed in the InGaAs channel, and (b), the density versus topgate voltage trace

3.8.2 Higher temperature operation[1]

To investigate the device operation at higher temperatures, the sample was cooled down in a 1.5K cryostat with a sample heater that can raise the sample temperature up to 100K. The device was than characterised at certain temperature points from 1.5K up to 80K. As a comparison, an undoped GaAs/AlGaAs heterostructure (V651) with the interface also 100nm below the surface was characterised at the same temperatures. Both samples had the same insulator (polyimide) so as to ensure that the differences observed are due to the semiconductor material.

[1]The samples used in section 3.8.2 were made by the author. However, the temperature dependence measurements were done by Dr. Bastian Marquardt at the Cavendish Laboratory.

These two samples only differ from each other in the extra 20nm of $In_{0.1}Ga_{0.9}As$ between the AlGaAs layer and the GaAs. .

3.8.2.1 Carrier density variation with temperature

For a device to work at a higher temperature, it is necessary to be able to maintain carriers in the conducting channel. A measure of this is how the carrier density changes with temperature. Fig.3.27 compares the behaviour of the undoped InGaAs sample with a GaAs/AlGaAs heterostructure sample as the temperature increases. The topgate voltage was held at the same value—10V, during the measurement. There is very little change in carrier density in the InGaAs sample as the temperature rises from 1.5K to 60K, while the carrier density in the GaAs sample drops gradually from 1.5K to 40K, with a significant decrease at temperatures higher than 40K. The difference between the InGaAs and the GaAs sample in the loss of carrier density as temperature rises happens at all carrier densities, and is further illustrated in fig.3.28. In the InGaAs channel sample, the density versus topgate voltage curve (fig.3.28(a)) shows little change up to 60K, whereas in the GaAs/AlGaAs sample (fig.3.28(b)), it is getting progressively harder to induce carriers as temperature rises above 1.5K. Once there is a large shift in the density versus gate voltage curve, it was also observed that the carrier density is not very stable in time.

3.8.2.2 Mobility variation

While the main aspect to consider for high temperature operation is whether the carrier density can be maintained, it is also interesting to investigate what happens to the mobility as temperature is varied, as this can give information on the scattering mechanisms that are dominating.

Fig.3.29 shows the variation in the mobility at a carrier density of $3x10^{11}$ cm^{-2} for the InGaAs and GaAs samples as the temperature is increased from 1.5K to 70K. The mobility in the GaAs sample decreases sharply as the temperature increases above 1.5K, whereas there is little change in the mobility of the InGaAs sample until above 30K. In the GaAs sample, the limiting factor for mobility at temperatures above 1.5K is scattering from acoustic phonons, which scales

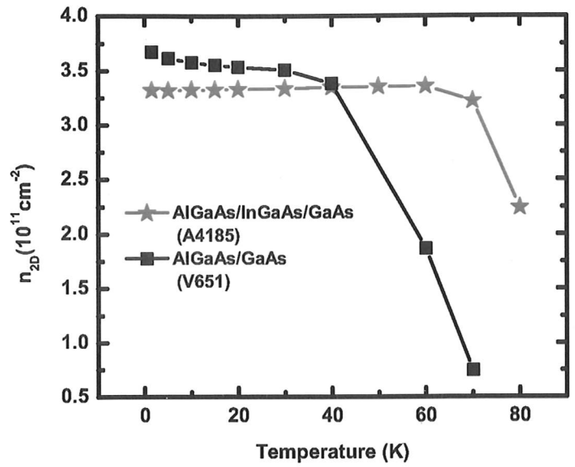

Figure 3.27: The change in carrier density of the InGaAs sample compared to a standard GaAs sample as temperature is varied from 1.5K to 80K

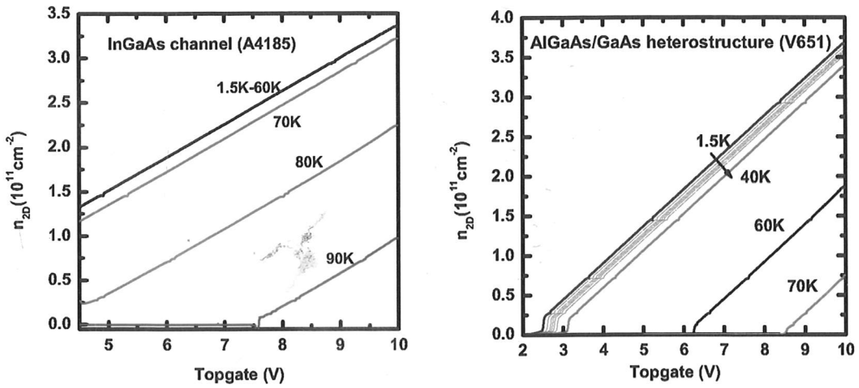

(a) (b)

Figure 3.28: The density versus topgate voltage relation for (a) the InGaAs channel sample, and (b) a normal GaAs/AlGaAs heterostructure

with temperature. In contrast, the limiting factor in the mobility of the InGaAs sample was not phonons until a higher temperature, which is why there is little change in the mobility up to 30K. A good illustration of the different dominant scattering mechanisms at different temperatures for InGaAs and GaAs samples can be found in [81].

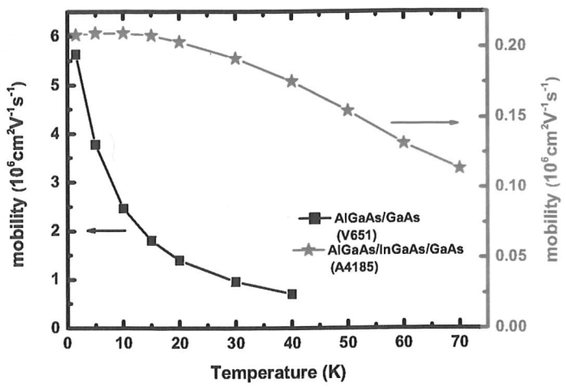

Figure 3.29: The change in mobility of the InGaAs channel sample compared to a standard GaAs sample as temperature is varied from 1.5K to 80K. For both samples, the mobility data was taken at a density of $3x10^{11}cm^{-2}$.

3.8.2.3 Influence of the insulator

As part of the investigation into higher temperature operation of undoped devices, the temperature variation on two GaAs/AlGaAs samples with different insulators (polyimide and SiO_2) was also measured. These two samples were from the same wafer (W639) with the 2DEG 160nm below the surface. Comparing the differences in the density versus gate voltage curves in fig.3.30, polyimide seems to be the better insulator, with less drift in the samples with temperature as compared to SiO_2. As the change in insulator does introduce a difference, it may be useful to explore other insulators, such as Al_2O_3 to see if further improvement can be achieved.

Comparing the sample shown in fig.3.30(a), which had a 160nm deep 2DEG,

with that in fig.3.28(b), which is a 110nm deep 2DEG, one can see that there is less shift in the carrier density versus topgate voltage curve as temperature rises in the deeper 2DEG. It may be that the thicker AlGaAs barrier reduces the tunnelling of the electrons from the 2DEG to the surface.

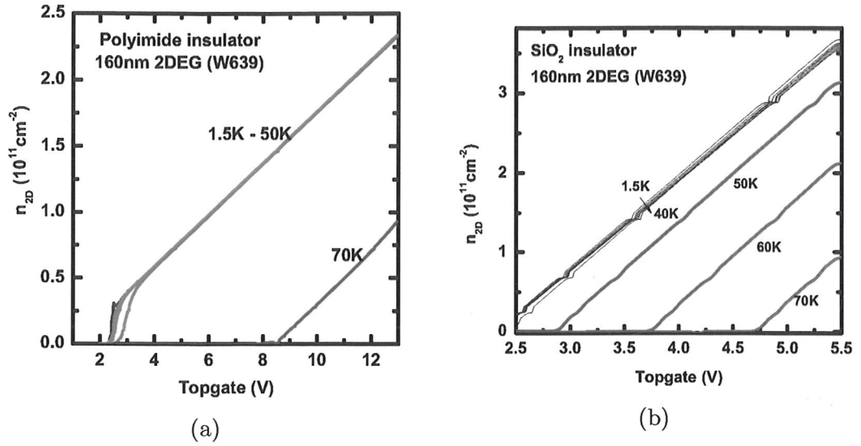

Figure 3.30: The density versus topgate voltage relation at various temperatures for two 160nm deep undoped 2DEGs with (a) polyimide insulation, and (b) SiO_2 insulation.

3.8.2.4 Further developments

This experiment shows that the higher bandgap in AlGaAs/InGaAs structure does help to increase confinement of electrons to the conducting layer. The choice of insulator and the depth of the 2DEG also have effects on how stable the carrier density is to higher temperatures. A development of the InGaAs structure, together with optimisation of the 2DEG depth, may potentially lead to devices that can work at liquid nitrogen, or even higher, temperatures.

3.9 Ambipolar devices

Ambipolar transport means that either electron or holes can flow through the same conducting channel. While this has been demonstrated in graphene [82],

it is not possible to achieve in doped GaAs samples. In undoped samples, the polarity of the carriers formed depends only on the gate voltage applied, and thus, with a suitable device design, it is possible to have electron or hole transport through the same sample [83]. As a first step towards more complex devices involving ambipolar transport, it would be useful to able to replicate the result from [83] in the induced device structure presented in section 2.3. The device is designed such that each voltage and current probe is connected to both an n ohmic and a p ohmic, and it is possible to change from measuring a 2DEG to a 2DHG without changing connections.

Fig.3.31 illustrates the operation of a device on an undoped heterostructure with both n-type (electron) and p-type (hole) ohmics[1]. Fig.3.31(a) shows the variation of carrier density with topgate voltage. This is linear in both the hole transport and electron transport regions, with the change in the sign of the density versus gate voltage slope signifying a change in carrier polarity. Between approximately -1V and 1V, the sample does not conduct, corresponding to an off state in such devices. Fig.3.31(b) shows the density-mobility relation of the electrons and holes through the same sample. As expected, the hole mobility is lower compared to that of the electrons.

This experiment has shown that it is possible to obtain working ambipolar transport on undoped heterostructures, and this paves the way for future experiments. For example, by placing the n and p ohmics on opposing ends of a hall bar, and using a split topgate design, it may be possible to obtain a p-n junction device. One can also make use of the fact that the electrons and holes experience a similar disorder potential to investigate effects such as Wigner crystallisation in magnetic field, in which the transition temperature is predicted to be independent of effective mass if the disorder potential is identical [73].

Recent work [84] has also demonstrated the possibility of obtaining ambipolar transport in undoped quantum wells. However, the heterostructure has advantages in that the processing is simpler, making it a better candidate for applications where the main requirement is the ability to change current direction.

[1]Sample fabricated by Dr. Bastian Marquardt. Measurements and mask design done by the author.

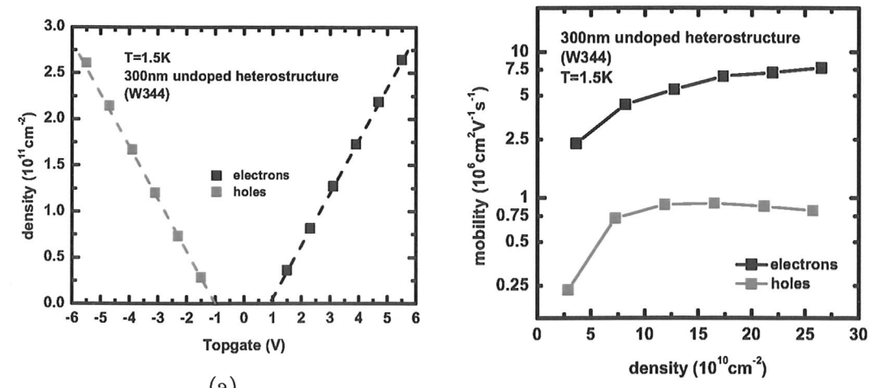

(a) (b)

Figure 3.31: (a) shows the relation between the carrier density and the topgate voltage, (b) the density-mobility relation of the two types of carriers in the sample.

3.10 Summary

In this chapter, I have covered various two dimensional transport experiments in undoped devices. They have provided examples of how undoped samples can be used to monitor a MBE chamber and help to optimise growth conditions. Bias cooldown and illumination experiments have provided a glimpse into the complex issues that remain with these two treatments despite the lack of dopants. High quality undoped samples also offer a potential route into exploring fragile Fractional Quantum Halll states such as the ν=5/2 state, as well as the low carrier density regime where the electron interaction is very strong. The use of different materials in undoped heterostructures, such as InGaAs, also offer a first step towards room temperature operation of undoped devices.

Chapter 4

Quantum dots on induced 2DEGs

4.1 Quantum dot theory[1]

A quantum dot is a zero dimensional (0D) system with a well defined set of energy levels, and a discrete number of electrons. There are many ways of forming a quantum dot, such as in self assembled quantum dots [87], carbon nanotubes [88], vertical quantum dots [89], and lateral semiconductor quantum dots (e.g.[90]). In a lateral semiconductor quantum dot, which is the system studied here, the 2DEG is formed into the dot shape via a potential applied by a set of gates, or by etching. In the gating method, formation of a quantum dot is by biasing metallic gates deposited on the GaAs surface. The gate is isolated from the surface by a Schottky barrier, and an applied voltage on the gate can then deplete carriers underneath, producing confinement to 0D.

In gated quantum dots, the dot is coupled to a reservoir of charges via tunnel barriers. It is also coupled capacitively to plunger gates, which can be used to vary the electronic levels in the dot. A simple illustration of this is shown in figure 4.1.

The quantum dot system can be modelled as a parallel plate capacitor, with a disc of electrons in the area, A, of the dot, separated by a layer of non-conducting GaAs, of distance d from the metal gate on the surface. The capacitance of the

[1]The important aspects of the theory of transport through quantum dots will be summarised in this section. However, a more detailed treatment can be found in references such as [29, 85, 86].

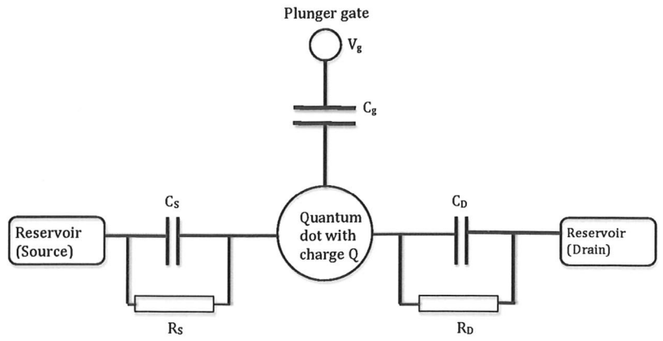

Figure 4.1: Equivalent circuit for a quantum dot. The dot, with charge Q, is coupled to the source and drain reservoirs via tunnel barriers, with resistances R_S and R_D, and capacitances C_S and C_D. It is also coupled capacitively to the plunger gate(s).

dot, C, is then:

$$C = \frac{\epsilon\epsilon_0 A}{d} \tag{4.1}$$

where ϵ_0 is the permittivity of free space and ϵ the relative permittivity of GaAs.

4.1.1 Energy levels in a quantum dot

In a quantum dot that is only weakly coupled to the reservoirs, the energy levels are well defined, and electrons can only hop into or out of the dot one at a time.

For a quantum dot with N electrons, the electrostatic energy, E_s of the overall system is not $(Ne)^2/C$, as there are free charges in the crystal that will flow to minimise the energy. The excess charges on the gates must also be taken into account. E_s can be expressed as:

$$E_s = \frac{(-eN + Q_0)^2}{2C} \tag{4.2}$$

$-eN$ is the charge inside the dot. $Q_0 = \sum C_g V_g$ is the excess charge in the system due to the gates and the potential in the 2DEG around the dot.

At zero temperature, the ground state energy of the dot with N electrons,

$U(N)$ is given by [91]

$$U(N) = E_s + \sum_{p=1}^{N} E_p \tag{4.3}$$

where E_p is the single particle energies relative to the bottom of the conduction band of the quantum dot. The chemical potential of the dot, $\mu_D(N)$, is the energy required to add an electron to the system, and can be expressed as:

$$\mu_D(N) = U(N) - U(N-1) \tag{4.4}$$

$$= E_N + \frac{(2N-1)e^2}{2C} - \frac{eC_gV_g}{C} \tag{4.5}$$

If there is no change in the gate voltage, then the energy required to add an electron to the dot, i.e. the charging energy, ΔU, is

$$\Delta U = \mu_{N+1} - \mu_N = E_{N+1} - E_N + \frac{e^2}{C} \tag{4.6}$$

If the 0D energy spacing between the $(N+1)$th and the Nth level, $E_{N+1} - E_N$, is small compared to e^2/C, then the energy of the dot changes by a discrete amount of e^2/C for every electron that hops on or off. The electrons inside the dot also interact with external charges to minimise the net charge of the system, and this will lead to the charge of the dot oscillating between -e/2 and +e/2 with respect to the gates for consecutive electrons tunnelling in or out of the dot.

4.1.2 Coulomb Blockade Oscillations

When the barriers of the quantum dot rises above the Fermi energy, the energy levels in the dot take well defined values. Electrons can only tunnel in and out of the dot when the energy levels in the dot align with those in the leads. In a gated quantum dot, as the plunger gate voltage is varied, the energy levels in the quantum dot shift and thus at periodic voltages the energy levels align and electrons can tunnel in or out of the dot, leading to oscillations in the measured current, which are known as Coulomb blockade oscillations.

Fig.4.2(a) illustrates the situation where the Coulomb blockade is lifted. In this case, the empty N+1 level aligns with the reservoirs. After an electron

tunnels into the dot, the occupied levels in the dot aligns with the leads, and no more electrons can tunnel into the dot until the one occupying the N+1 level tunnels out of the dot. For plunger gate voltages where the energy levels do not align, there can be no transport through the dot, as illustrated in fig.4.2(b).

To observe Coulomb blockade oscillations, one must ensure that the dot is well isolated, and therefore the tunnel barriers must be high enough in energy that the electrons from the reservoirs cannot gain enough thermal energy to hop into the dot, i.e. $k_BT << e^2/C$. To be able to resolve energy levels separated by e^2/C, the condition on the tunnel barrier height can also be determined by using the uncertainty principle $\Delta E \Delta t > h$. ΔE, the uncertainty in energy, is equal to the charging energy, e^2/C. Δt is the time to charge the island and is equal to R_BC where R_B is the resistance of the tunnel barrier, and therefore $R_B > h/e^2$.

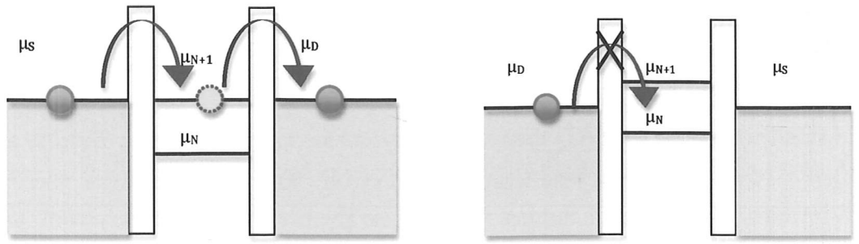

(a) (b)

Figure 4.2: (a) shows the case where the energy levels in the quantum dot align with the leads, allowing transport through the system. (b) shows the case where the energy levels do not align, and hence transport is blockaded.

The spacing between the Coulomb blockade peaks in terms of the plunger gate voltage (V_{pg}) is given by the the relation [86]

$$\Delta V_{pg} = \frac{C}{C_g}\left(\frac{E_{N+1} - E_N}{e}\right) + \frac{e}{C_g} \tag{4.7}$$

For a small energy spacing between the levels in the quantum dot, one can approximate the spacing to be e/C_g. One can also define a term α, the lever arm, that is used to quantify the coupling of the plunger to the dot, thus describing

how much effect the plunger gate has on the system. α is given by:

$$\alpha = \frac{\Delta U}{e\Delta V_{pg}} \tag{4.8}$$

where ΔU is the charging energy and ΔV_{pg} is the spacing between two Coulomb blockade peaks.

4.1.3 Source-drain bias spectroscopy

A source-drain bias spectroscopy measurement generates a picture called 'Coulomb blockade diamonds', from which one can measure the charging energy, excited state energy, and level arm of the quantum dot. In this measurement, plunger gate sweeps are taken at many different source-drain bias values, and the sweeps are plotted together in a grayscale to generate the plot.

When a source-drain bias is applied to a quantum dot system, a 'bias window' opens, and the energy levels of the quantum dot no longer have to match those of the leads in order for an electron to hop on or off, and a current can flow as long as $\mu_s \geq \mu_N \geq \mu_d$. This is illustrated in fig.4.3. In fig.4.3(a), there is no transport as the bias is insufficient for electrons to hop onto the dot. In fig.4.3(b), the bias is just sufficient for electrons hop onto the dot via one of the energy levels, and if sufficient bias is applied, as in the case of fig.4.3(c), two energy levels can be involved in transport. In this picture, only the ground states of the quantum dot are involved.

4.1.3.1 Excited state spectroscopy

In addition to transport through the ground state of each of the quantum dot levels, at certain bias, excited states of certain energy values in the dot may become accessible. This situation is illustrated in fig.4.4(a). The N-1 ground state does not take part in transport as it is at a lower potential than the drain. However, the N-1 excited state (called N-1* in the diagram) has an energy higher than the drain, and therefore can take part in transport. This excited state transport leads to extra lines which can be seen in the 'Coulomb diamonds' measurement, as illustrated in fig.4.4(b). However, the excited states can only be

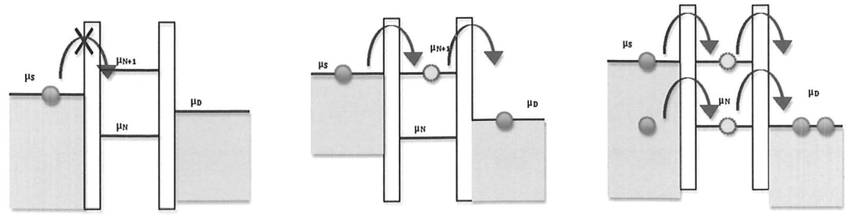

(a) (b) (c)

Figure 4.3: If the source-drain bias is insufficient, as in (a), there is no transport through the system. If the bias is sufficient, electron transport can take place through one of the energy levels in the dot (b). For even higher bias voltages, two levels can be involved (c).

seen if the temperature is low enough that thermal broadening does not occur, i.e. $k_BT << \Delta E$. For example, in fig.4.4(c), which shows a higher temperature (1.4K) measurement of the same device as that in fig4.4(b), the excited states are smeared out.

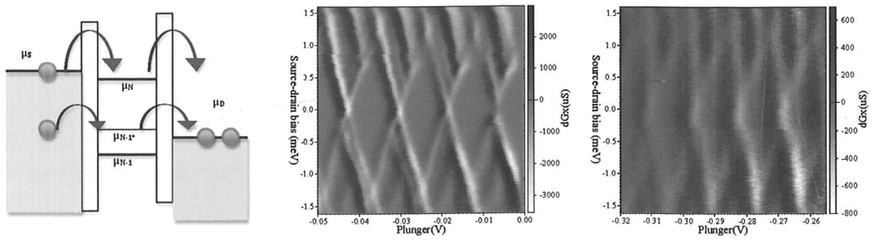

(a) (b) (c)

Figure 4.4: (a) an illustration of how excited states can take part in transport through a quantum dot under bias. (b) and (c) shows 'Coulomb diamonds' measurements on the same undoped quantum dot device at different temperatures. (b) is at 300mK and (c) is at 1.4K. The excited state lines can be seen clearly in (b) but are not visible in (c)

4.1.3.2 Interpreting a Coulomb diamond

Each line in the Coulomb diamonds plot corresponds to where certain energy levels in the quantum dot align with those in the leads. Fig.4.5 shows an illustration of this. Within each diamond defined by the brown solid lines, the quantum dot is in the blockaded regime and electrons cannot hop on or off. At point (a), and at similar points where two lines cross, the energy levels that the source and drain aligns with differ by one electron, and both states can take part in transport. By measuring the energy of this point (which is given by V_{SD}), one can obtain the charging energy, ΔU, of the quantum dot. The dotted lines in the fig.4.5 corresponds to the excited state lines. At (b), the energy levels that the source and drain align with are the ground state and the excited state of a particular energy level. Thus one can also obtain the single particle excitation energy, ΔE. Using equations 4.6, 4.8 and 4.7, one can also obtain the values for C, α, and C_g.

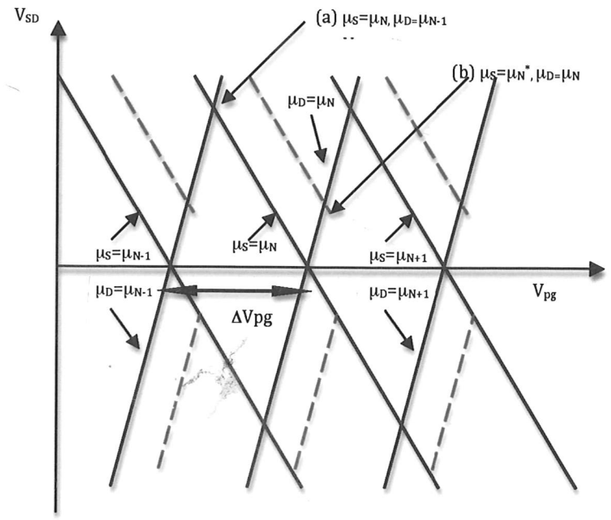

Figure 4.5: An illustration of the lines seen in a Coulomb diamond, and the energy levels they correspond to.

4.1.4 Temperature Dependent Lineshape of Coulomb Blockade oscillations

By considering resonant tunnelling through the barriers in the quantum dot, one can derive the expression for electron transport through a dot contaning N electrons. The conductance, G, is given by [85] :

$$G = \frac{e^2}{h}\frac{A}{k_B T}\int_{-\infty}^{\infty}\left[\frac{(h\Gamma)^2}{(E-E_0)^2+(h\Gamma)^2}\right]\mathrm{sech}^2\left[\frac{E-\mu}{2k_BT}\right]dE \qquad (4.9)$$

where A is a constant, $\Gamma = (\Gamma^S + \Gamma^D)/2$, where $\Gamma^{S(D)}$ is the tunnel coupling of the source(drain) barrier, and μ is the chemical potential.

4.1.5 The strong and weak coupling regimes

Depending on the how high the barriers are in a quantum dot, the system can be in the strong coupling or weak coupling regime. In the weak coupling regime, the barriers are sufficiently high that the quantum dot states are well isolated from the states in the leads. The lineshape of the Coulomb blockade then takes on the form of a thermally broadened resonant peak and is proportional to $1/cosh^2(e\alpha(V_g - V_0))$ [90, 92]. In the strong coupling regime, the states inside the dot are very linked to the states in the leads and the reservoirs. This leads to a residual conductance through the dot even in the blockaded region. Thus in the observed Coulomb blockade, the minima do not go to zero conductance, and the lineshape takes on form that is a convolution of the derivative of the Fermi-Dirac distribution with a Lorentzian form [90]. This closely approximates to a Lorentzian lineshape if $\Gamma >> k_BT$ i.e.

$$G \propto \frac{\Gamma/2}{(\Gamma/2)^2 + e\alpha(V_g - V_0)} \qquad (4.10)$$

All the measurements on quantum dots presented in this chapter are done in the weak coupling regime. This was to ensure that the leads does not have an effect on the measurements. In addition, certain effects, such as the excited states, are difficult to observe in the strong coupling regime.

4.1.6 Single and multi level transport

Single level transport occurs if $h\Gamma << k_BT < \Delta E < \Delta U$, where ΔE is the single particle energy spacing of the quantum dot. In this regime, only one level in the dot is involved in transport, and the excited states are not accessible at zero bias. Then equation 4.9 simplifies to [93]:

$$G_s = \frac{e^2}{h}\frac{A_1}{k_BT}sech^2\left[\frac{e\alpha(V_g - V_0)}{2k_BT}\right] \qquad (4.11)$$

where A_1 is a constant.

Multi-level transport occurs in a quantum dot when $\Delta U > k_BT >> \Delta E$. This means that a series of states in the quantum dot can participate in transport due to temperature broadening. The conductance can be approximated by:

$$G_m = \frac{e^2}{h}\frac{A_2}{\Delta E}sech^2\left[\frac{\alpha(V_g - V_0)}{2.5k_BT}\right] \qquad (4.12)$$

for a constant A_2.

To determine whether a quantum dot is in the single or multiple level transport regime, one has to measure the temperature dependence of the Coulomb blockade peaks. In the single level regime, the peak height, Gmax, is proportional to 1/T, and the full width at half maximum is equal to $2k_BT/\alpha e$. In contrast, the peak height is temperature independent in the multi-level transport regime, and the full width at half maximum is equal to $2.5k_BT/\alpha e$ [93]. A_1 and A_2, which are dependent on the tunnelling barriers Γ_L and Γ_R, are assumed to be temperature independent and hence does not affect the temperature dependent changes in the Coulomb blockade peaks.

4.2 Gate-defined Quantum dot on a very shallow induced 2DEG

In order to define sharp details on a mesoscopic device, it is advantageous to have the 2DEG as close to the confinement potential as possible. While quantum dots have been fabricated as close as 28 nm to the surface on doped wafers [16], these

were done via AFM lithography. Gated quantum dots on doped wafers with a 2DEG that is so close to the surface could not be fabricated due to the difficulty in obtaining devices that are gateable. However, with undoped wafers there is no such problem and, using the technique for contacting shallow 2DEGs discussed in chapter 1, it was possible to fabricate quantum dot devices on a 2DEG that is 30nm below the surface using standard lithographic techniques.

A simple 6-gated design, as shown in fig.4.6 was used. To operate the device, the topgate was held constant at a voltage that would induce a high carrier density. For example, in this particular device, the topgate was held at 8V, corresponding to an electron density of approximately $2.5\text{x}10^{11}\text{cm}^{-2}$. The barriers were then held at a constant positive value, while the plunger was swept.The Coulomb blockade oscillations observed, as shown in fig.4.7, indicated tunnelling transport taking place. In the 300mK trace of the peaks close to pinch off, (fig.4.7(b)), the conductance goes to zero between the Coulomb blockade peaks, indicating that the system is in the weak coupling regime. The fit of two of the peaks to a $1/cosh^2$ form is shown in fig.4.7 (d) and (e), a further confirmation that the system is indeed in the weak coupling regime at 300mK. The persistence of the Coulomb blockade oscillations up to 1.4K (fig.4.7(c)) is an indication of the high charging energy of the system.

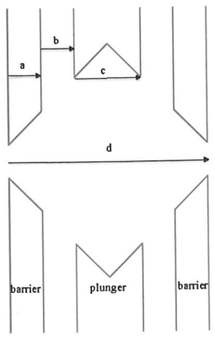

Figure 4.6: A schematic of the gate configuration in the quantum dot. The four gates on the edges form the barriers, and the two gates in the centre form the plunger. For the quantum dot on the 30nm deep 2DEG, the lithographic dimensions of the dot are: a=60nm, b=60nm, c=120nm, and d=360nm.

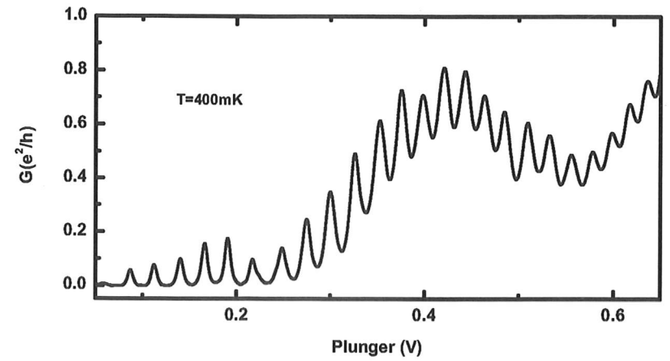

(a)

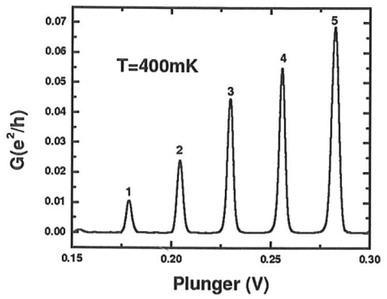

(b)

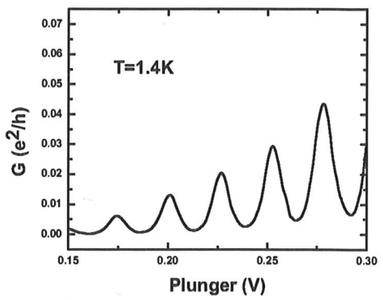

(c)

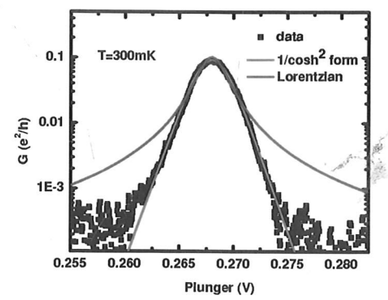

(d)

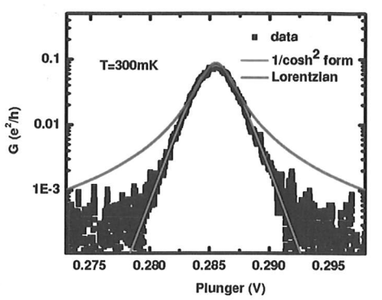

(e)

Figure 4.7: Coulomb blockade oscillations of a quantum dot 30nm below surface. (a) shows both the weak and strong coupling regimes, and (b) focuses on several peaks from (a) which are closest to pinch off; (c) shows the same peaks, but at a higher temperature of 1.4K. (d) and (e) shows the fit of peaks 4 and 5 respectively to a $1/cosh^2$ form. The good fit indicates that the system is in the weak coupling regime. The best fit to a Lorentzian is also shown for comparison

4.2.1 Bias spectroscopy

Additional parameters were also found from the source-drain bias spectroscopy in fig.4.8. These include the charging energy, ΔU=1.25meV, the total capacitance, C_Σ=128aF, α=0.083meV/mV, and C_g=9.5aF. By modelling the dot as simple capacitor, and using equation 4.1, the area of the dot is approximately 3.4x10^{-14}m^2, and number of electrons in the dot is estimated to be 80. Compared to the actual lithographic dimensions of the dot, which is 1.0x10^{-13}m^2, which would contain approximately 250 electrons, the actual dot is smaller. This effect is true of all induced mesoscopic devices. As the Schottky gates defining the device screen the topgate, the area depleted of carriers inside the dot would be larger than the gates themselves. This means that undoped mesoscopic devices can have larger, more robust Schottky gates than their doped counterparts.

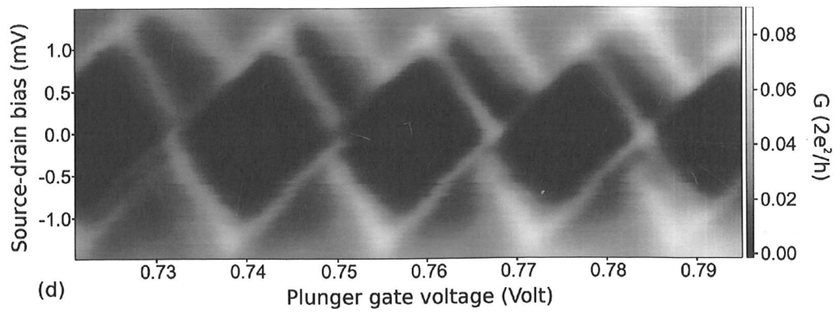

Figure 4.8: Source Drain Bias spectroscopy measurement of an induced quantum dot device on a 30nm deep 2DEG

4.2.2 Temperature dependence measurements

When the 0D system is in the temperature broadened regime rather than the lifetime broadened regime (i.e. weak coupling), the shape of the Coulomb blockade is also useful for determining the actual electron temperature. The Coulomb blockade peaks were measured at a series of temperatures, and equation 4.9 was used to fit these peaks. A set of parameters was found such that to fit a certain peak at different temperatures, all that needs to be changed is the value of T in

equation 4.9. The values of temperature that give the best fit to all the peaks will be the electron temperatures.

Fig.4.9 compares how the electron temperature varies with thermometer reading. As expected, the lower temperatures deviate from the thermometer reading due to heating effects such as noise, causing the electrons to be hotter than the lattice. At higher temperatures, the electron temperature closely approximates that of the thermometer reading.

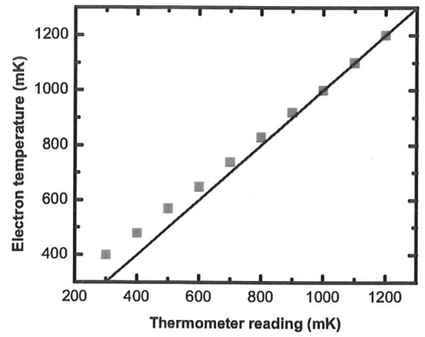

Figure 4.9: Calibration of electron temperature versus thermometer reading. Symbols are obtained from fitting, and the line shows what the electron temperature would be if it exactly follows the thermometer reading.

The temperature variation of the maximum conductance and the full width at half maximum of the Coulomb blockade peaks were also measured to determine whether the system is in the single level transport regime or the multi level transport regime. In fig.4.10 the variation in the peak height as well as the FWHM of two of the peaks is shown. In (a), the variation in 1/Gmax is linear with temperature from 400mK to 800mK, suggesting that the quantum dot is in the single level transport regime. Above 800mK, there is a transition to the multi-level transport regime, with an almost temperature independent peak height. In (b), the FWHM has a linear dependence with temperature, as expected from equation 4.11. While the FWHM data does not show a change in slope at 800mK which would indicate a change from single level to multi level transport, this may be because the change is not sufficient to see within error.

The temperature dependence of the peak amplitude and width can be more complex than the ideal case. While the two peaks which are analysed in detail here have a FWHM versus temperature relation that is linear, as expected from equation 4.11, other peaks have a peak height and FWHM relation with temperature that is not linear. An explanation for this is suggested in [93, 94]: if the energy levels corresponding to adjacent peaks have very different coupling strengths to the leads, then the variation of the peaks with temperature will be determined by how big k_BT is compared to the relevant energy level spacings. Extrapolating the data shown in fig.4.10(b), peak 4 has a zero FWHM at zero electron temperature as one would expect from equation 4.11. However, peak 5 has a finite FWHM at zero electron temperature. This suggests that the approximation of $h\Gamma << k_BT$ is not quite correct for this peak, and hence there is still a finite peak width at zero temperature.

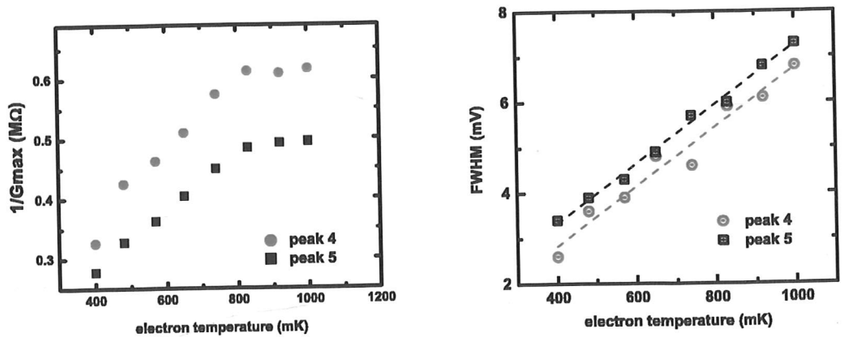

(a) (b)

Figure 4.10: Temperature dependence of Coulomb blockade peaks of a quantum dot on a 30nm deep 2DEG.

4.2.3 Devices with SiO_2 as insulator

Another two quantum dots, of the same dimensions and the same 2DEG depth as the sample discussed above, were made with 175nm of SiO_2 as the insulator. A similar 2DEG density was achieved using a topgate voltage of 4.5V. These devices were characterised, with the properties listed in table 4.2 (p.117). They

have very similar charging energies and capacitances, suggesting that as long as one can obtain the induced 2DEG with no leakage to the ohmics, the operation of the mesoscopic device will not be affected greatly by the choice of insulator.

4.3 Quantum dots at different depths

While a quantum dot on a 30nm deep 2DEG offers advantages of giving good confinement, there is a possibility that interactions with the surface states can make it 'noisy'. As discussed in section 3.3, the influence of the surface states on 2D properties decreases as the depth of the heterointerface increases from 30nm to 60nm, and is almost negligible at 110nm. Therefore, it would be useful to investigate quantum dots defined on these different depths to see whether stability would increase, as well as testing whether it is possible to define a quantum dot at the deepest depth. This investigation will give insight into the best 2DEG depth for future experiments on more complex 0D systems, such as double dots.

A set of quantum dots with the 2DEG at 60nm and 110nm below the surface were fabricated to investigate the effects the 2DEG depth has on the operation of the device. They had the same design as the 30nm deep sample discussed in section 4.2, with minor modifications to the gate dimensions in order to obtain good working devices. (i.e., showing Coulomb blockade peaks in the weak coupling regime). Referring back to fig.4.6, the dimensions for the 60nm and 110nm deep quantum dots are:

2DEG depth(nm)	a(nm)	b(nm)	c (nm)	d (nm)
30	60	60	120	360
60	90	90	180	540
60	120	120	240	720
110	175	100	150	700

Table 4.1: Dimensions of the quantum dot devices on 30nm, 60nm and 110nm deep 2DEGs. a, b, c, d are illustrated in fig.4.6.

For the 60nm deep quantum dots, it is possible to obtain a working sample just by enlarging the dimensions of the Schottky gates as compared to 30nm deep

devices. Both dimensions stated in table 4.1 work, but samples made using the smaller dimensions were easier to tune and to observe Coulomb blockade in the weak coupling regime. For the 110nm deep device, it was necessary to modify the relative sizes of the plunger and the barriers. An initial design where the dimensions were scaled up from shallower devices could not be tuned, due to the plunger being very dominant.

4.3.1 Quantum dots defined on a 60nm deep 2DEG

Fig.4.11 shows the data obtained from a quantum dot on a 60nm 2DEG. (a) shows the Coulomb blockade oscillations at base temperature (280mK) and at 1.2K. Similar to the quantum dot on the 30nm deep 2DEG, the charging energy is sufficiently high that the oscillations can still be observed at 1.2K. Fig. 4.11(b) shows one of the peaks with a $1/\cosh^2$ fit and a Lorentzian fit. While neither form fits the peak exactly, the $1/\cosh^2$ form is a better fit. Together with the fact that the conductance minima between the peaks are zero at 280mK, this suggests that the peaks shown are in the weak coupling regime. The temperature dependence of the Coulomb blockade peak was also investigated, and figures 4.11(c) and 4.11(d) show the temperature variation of the peak height and the peak width respectively. The relation between 1/(peak height) and temperature is linear up to approximately 1K, suggesting that the system is in the single level transport regime, with a transition to multi-level transport at around 1K. The slope of the FWHM curve is also linear, as one would expect from Coulomb blockade in the weak coupling regime. However, extrapolating the curve in fig.4.11(d) will give a negative FWHM at zero temperature. This rather counterintuitive result may be due to the assumption that the constant A_1 in equation 4.11 being independent of temperature is no longer correct.

Fig. 4.12(a) shows the bias spectroscopy measurement, from which the parameters obtained included: the charging energy ΔU=1.1meV; plunger lever arm, α=0.116meV/mV; single particle energy spacing ΔE=0.3meV; plunger capacitance C_g=16.8aF; total capacitance C_Σ=145aF, with approximately 200 electrons.

Similar to the 30nm quantum dot presented above, a calibration of the electron

temperature versus the thermometer reading was also done by fitting the Coulomb blockade peak shown in fig. 4.11(b) with equation 4.9. This was necessary as the quantum dots on the 60nm and 110nm deep 2DEGs were measured in a different cryostat. The measurement set up was slightly different, and the heating effects of noise on the electrons would be different as well. The results of this calibration are shown in fig.4.12(b), and the electron temperatures quoted in the temperature dependence measurements were obtained from this calibration.

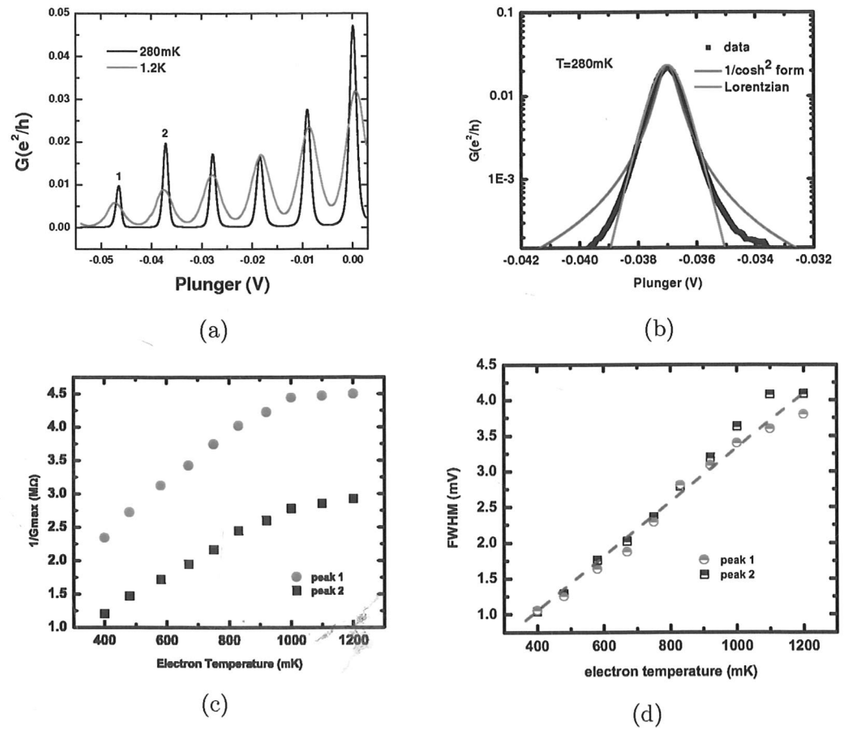

Figure 4.11: Data obtained from a quantum dot on a 60nm deep 2DEG, with (a) showing Coulomb blockade peaks, (b) showing a Coulomb blockade peak with $1/\cosh^2$ and Lorentzian fits, (c) variation of the maximum peak height with temperature, and (d) the variation of the peak width with temperature.

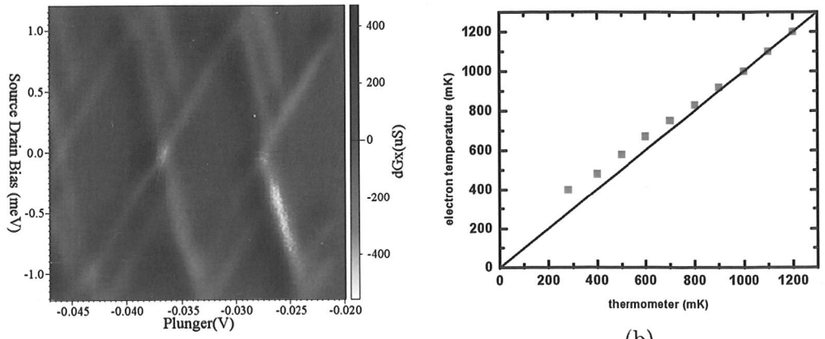

(a) (b)

Figure 4.12: Further data obtained from a quantum dot on a 60nm deep 2DEG. (a) the source drain bias spectroscopy plot, and (b) the calibration of the electron temperature versus thermometer reading.

4.3.2 Quantum dots defined on a 110nm deep 2DEG

In a gated quantum dot device, a deeper 2DEG will result in a less sharply defined electric potential, and this may lead to a smaller charging energy and a system that is harder to decouple from the reservoirs. Nonetheless, after several variations of gate dimensions, a working device was obtained on an undoped 2DEG that is 110nm below the surface. Fig.4.13(a) shows the Coulomb blockade traces at 280mK and at a higher temperature of 900mK, while fig.4.13(b) shows a $1/\cosh^2$ fit to one of the Coulomb blockade peaks. These two indicate that the system is in the weak coupling regime in the set of peaks shown. While it is still possible to observe Coulomb blockade peaks that are in the weak coupling regime, most of these peaks are very small in amplitude, even after significant tuning. It may be that the dimensions of the device still requires optimisation, but it is also possible that it is harder to define a 0D system due to the spreading out of the electric field from the Schottky gates.

The temperature dependence of two of the peaks is shown in fig.4.14(a) and (b). Similar to the other two quantum dots, the FWHM versus temperature trace is linear, and the data extrapolates to a zero FWHM at zero temperature. The scatter of the data points makes it difficult to state with certainty whether there

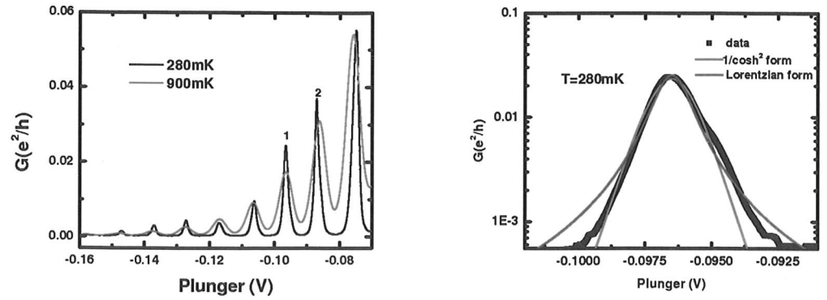

(a) (b)

Figure 4.13: Data obtained from a quantum dot on a 110nm deep 2DEG, with (a) showing Coulomb blockade peaks, and (b) the fit of one of the peaks to a $1/\cosh^2$ form. Together, they illustrate that the system is in a weak coupling regime near pinch off.

is a change in slope. However, the 1/Gmax versus temperature plot shows a transition to a temperature independent state at around 600mK, suggesting a transition to a multi-level transport regime. While a transition temperature of 600mK is lower than that of the 30nm and 60nm deep devices, this is not unexpected as the energy levels of the 110nm deep quantum dot are more closely spaced. The energy levels measured via bias spectroscopy (fig.4.15) are charging energy ΔU=0.9meV and single particle energy spacing ΔE=0.25meV. The other parameters that can be obtained are: plunger lever arm, α=0.100meV/mV; plunger capacitance C_g=17.8aF; total capacitance C_Σ=177.8aF, and approximately 420 electrons.

An interesting point to note from the bias spectroscopy measurement is that in the 30nm and 60nm deep quantum dots, ΔU does not vary noticeably between peaks that are close together. However, for this sample, the ΔU measured from the bias spectroscopy changes from 0.9meV to 0.5meV from peak 1 closest to pinch off to peak 5 that is furthest from pinch off. The decrease in charging energy means that the energy levels of the quantum dot are getting more closely spaced as the system moves away from pinch off. This indicates that the decrease in the confinement potential between peaks is more significant for 110nm deep

quantum dots compared to devices on 30nm and 60nm 2DEGs.

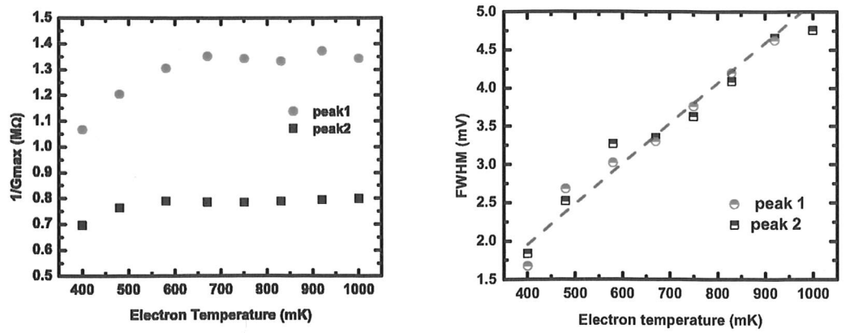

(a) (b)

Figure 4.14: Variation of Coulomb blockade peaks with temperature, with (a) showing the peak height variation and (b) the peak width variation of the quantum dot on a 110nm deep 2DEG.

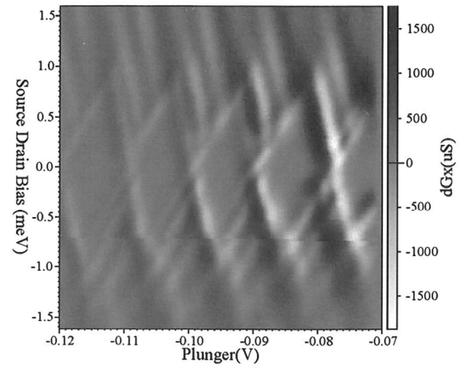

Figure 4.15: Bias spectroscopy measurements of a quantum dot on a 110nm deep induced 2DEG.

4.4 Determining the stability of a 0D system

Mesoscopic devices such as quantum dots and quantum wires can interact with charge fluctuations in the surroundings, leading to 'Random Telegraph Signal' (RTS) noise. This leads to sudden shifts in the device characteristics, for example, the positions of the Coulomb blockade peaks may show a jump. Besides introducing extra error into measurements, such interactions could lead to unwanted effects such as spin decoherence in coupled quantum dots [95, 96].

There have been many studies conducted into the origin and the reduction of RTS noise in doped mesoscopic devices, and there have been many proposed mechanisms for the origin of the RTS. These include: small leakage currents from the surface gates [97, 98], switching due to remote ionised impurities and defects [99, 100] from DX centres [101], and trapping and detrapping of electrons, which lead to a fluctuating potential [102]. However, there are very few studies of RTS in *undoped* mesoscopic devices. As one potential source of RTS noise is the intentional dopants, one would expect that undoped devices would be 'quieter' than their doped counterparts.

While most studies into RTS noise utilise quantum wires, it would be useful to characterise this in quantum dots, especially undoped quantum dots, as they are a different system, and it is necessary to confirm whether the methods of reducing RTS noise in quantum wire devices are still applicable. This can help

develop a stable undoped quantum dot system, which will be essential for more complex devices as well as improving measurement accuracy in other undoped mesoscopic devices.

4.4.1 Experimental method

In many studies of RTS noise, the noise spectrum was found by taking a time trace of the conductance around a fixed value. This was usually chosen to be the region between the pinch off and the first conductance plateau of a quantum wire, as any changes to the system are most easily observable at this point. An analogy in a quantum dot is the position halfway up a Coulomb blockade peak. However, if the device drifts away from this region, for example, to the top of a Coulomb blockade peak or to the zero conductance region between the peaks, the measurement would become less sensitive to the changes made by RTS. One way of ensuring that there is little drift in the device is by letting the device stabilise after cooldown, which may take several days.

As the measurements were carried out in a 300mK system, where the base temperature can only be held for 70 hours, there is insufficient time to allow the device to 'settle down' after each cooldown or condensation. As a result, there is usually a unidirectional drift in the peak position. This is unrelated to the instability in a 0D device due to RTS noise (from coupling to impurities or surface states). To investigate how stable a device is, the voltage on the plunger gate is swept through the same set of peaks (usually four or five) over a period of two hours at the rate of 1.5V/hr. The peak position is then found and the drift is corrected for by using a linear fit to the data points, and the slope subtracted. The scatter of the peak positions for each plunger gate sweep about the mean is normalised with respect to the full width at half maximum of the Coulomb blockade peak. This is to allow a comparison between different peaks or even different devices. This works because all devices compared are in the single level transport regime, and all are measured at 300mK (with an approximate electron temperature of 400mK). In this regime, the width of the Coulomb blockade peak is essentially dictated by thermal broadening k_BT. The variance of the distribution about the mean is then calculated. A greater variance would suggest a more

'noisy' device, where there is a greater variation about the mean position.

All the peaks chosen for this measurement are in the weak coupling regime, as a stronger coupling to the leads can change the stability characteristics of the device. In addition, all the peaks that are measured have a maximum amplitude of at least 0.2μS of conductance, as it was not possible to measure smaller peaks accurately due to equipment and circuit noise.

This method is not the most precise way to quantify noise in the quantum dot devices. In [103], a technique for measuring and quantifying the noise levels in lateral quantum dots is presented. However, this requires the use of non-invasive charge detection techniques, which is not possible with the current device design. Given the limitations of the present device design, the method discussed in this section offers a useful way to compare differences between cooldown regimes and/or quantum dots at different depths.

4.4.2 Depth dependence of device stability

To investigate the optimal 2DEG depth for undoped mesoscopic devices, the stability of quantum dots made on 2DEGs at 30nm, 60nm and 110nm below the surface was measured. Two or more samples were measured for devices on 30nm and 60nm deep 2DEGs. In the 110nm deep 2DEG, this was not possible as there was only one working device. Figure 4.16 shows the variance values for Coulomb blockade peaks at each depth. As expected, quantum dots that are 60nm deep are more stable than the 30nm dots, as the influence of surface states on a deeper 2DEG is smaller. Surprisingly, there is little improvement in quantum dots that are at a depth of 110nm compared to those that are 60nm deep. This is probably due to the fact that there may be other sources of RTS besides the surface states, and these become the limiting factor to device stability as the 2DEG depth increases. In addition, the confinement potential in the quantum dots on the 110nm 2DEG may not be as strong as in the shallower dots, resulting in a greater sensitivity to external influences such as ionised impurities.

It would also be useful to investigate whether different insulators have an effect on the stability of devices. However, due to fabrication issues, no working samples using SiO_2 were obtained on quantum dots on 60nm and 110nm deep

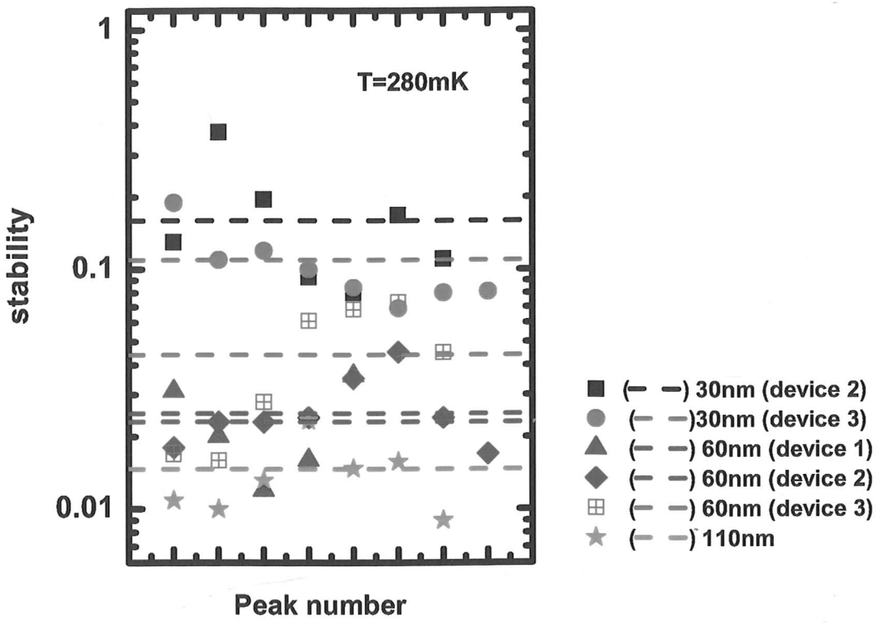

Figure 4.16: The variation of stability of quantum dots at three different depths. The 30nm quantum dot samples had SiO_2 as the insulator while the polyimide was used in other samples. The dashed lines show the average 'stability value' of each sample. The method of determining this is explained in section 4.4.1

2DEGs. While quantum dots on 30nm 2DEGs have been made with both SiO_2 and polyimide as the insulator, a stability measurement on the dot with polymide was not carried out.

4.4.3 Reproducibility of device characteristics

One important aspect of experiments on mesoscopic devices is the reproducibility of device characteristics from sample to sample, and in the sample for different cooldowns. For example, quantum dots with nominally the same gate dimensions on a 2DEG at the same depth should show the same charging energy, and approximately the same periodicity in the Coulomb blockade oscillations. The same device should also show similar behaviour between cooldowns. This is important as, ideally, any observations made on a particular sample should be reproduced in order to reduce experimental error.

In doped mesoscopic devices, it is often reported that certain illumination or cooldown regimes are necessary in order for the samples to work or to reduce RTS noise (e.g.[104]). However, the effects of these regimes are not necessarily easily reproducible [98]. With quantum dots on undoped 2DEGs 30nm and 60nm deep, it was found that device characteristics were very similar between samples and cooldowns. Tables 4.2 and 4.3 show the parameters from the measurements of six devices on 2DEGs 30nm and 60nm deep, with three from each depth. As can be seen, devices share very similar characteristics.

Device	ΔU (meV)	ΔE_c (meV)	C_Σ (aF)	C_g (aF)	α (meV/mV)	stability
1	1.25	0.50	128	9.5	0.083	n.a.
2	1.30	0.55	123	12.3	0.093	0.16
3	1.20	0.55	133	12.3	0.092	0.11

Table 4.2: Parameters of quantum dots on a 30nm 2DEG. The value of stability is the average of the normalised variance of all the Coulomb blockade peaks in the stability measurement . Device 1 had polyimide as an insulator whereas devices 2 and 3 had SiO_2 as an insulator.

Device	ΔU (meV)	ΔE (meV)	C_Σ (aF)	C_g (aF)	α (meV/mV)	stability
1	1.1	0.30	145	16.8	0.116	0.023
2	0.7	0.20	229	16.0	0.070	0.025
3	1.2	0.30	160	16.0	0.100	0.052

Table 4.3: Parameters of quantum dots on a 60nm 2DEG. Device 2 has a slightly different dimension compared to devices 1 and 3.

4.5 RTS noise and the effects of bias cooling

A common method for reducing RTS in doped mesoscopic devices is by bias cooling, where an electric field is applied as the device is cooled from room temperature. Explanations of why this technique works include the changing of the state of the deep traps in the semiconductor that contribute to RTS [105]; that it affects the energy levels of the DX centers and hence changes whether electrons can hop into and out of them into the mesoscopic region [56]; and that it shifts the operational voltage of the Schottky gates, leading to a reduction in the minute current leakage from the gates [97, 98]. While this current is virtually undetectable, devices are more noisy if a current flows.

4.5.1 Bias cooldown of induced quantum dot devices

To obtain more information of the cause of instability in induced quantum dot devices, a set of bias cooldown experiments was conducted on induced quantum dot devices at 2DEG depths of 30nm, 60nm and 110nm (i.e. the devices discussed in the previous section).

4.5.1.1 Cooldown routine

In each bias cooldown, the gates defining the quantum dot was connected together, then a SMU, with the current compliance level set to 5nA to prevent damage to the sample, was used to apply either a positive (0.3V) or a negative voltage (-0.3V) from room temperature as the sample was cooled to 300mK. The ohmic contacts and the topgate were kept grounded during cooldown. On reaching base temperature, the device was tuned to ensure that the device was operating in the weak coupling regime. The stability measurement as discussed

in section 4.4 was then conducted. The topgate was not biased during cooldown in these experiments as initial tests found that there is no effect on the operation of the quantum dot on biasing the topgate, even at voltages which produced a change in the mobility of the 2DEG (as discussed in section 3.5). Source-drain bias spectroscopy and temperature dependence measurements were also taken to investigate whether the device has changed in other ways besides the stability.

4.5.1.2 Changes in device characteristics

While bias cooldowns on mesoscopic devices on doped 2DEGs can affect the operating voltages of the gates [97], there was no significant change in the operating voltages in the undoped quantum dots measured, beyond a variation that comes with every cooldown. The period of the Coulomb blockade peaks was unchanged within experimental error, and parameters such as the charging energy and the capacitance of the dot were also not affected by a bias cooldown. However, there can be variations in the number of Coulomb blockade peaks in the weak coupling regime, as well as variation in the peak amplitudes between cooldowns.

4.5.1.3 Effects on stability

Fig.4.17 shows the effects of bias cooldowns on three different quantum dot devices at different 2DEG depths. The 'stability' is obtained by the method discussed in section 4.4.1, and each symbol represents a Coulomb blockade peak which is in the weak coupling regime. The average of the stability of all the peaks with the same cooldown regime is shown by the dotted lines in the graphs.

The results of this bias cooling experiment are less clear than the results of the experiment on 2DEGs as presented in section 3.5, with the three devices showing quite different responses. In the 30nm deep quantum dot, there is little difference in device stability between cooldowns with 0V, 0.2V and -0.2V bias. The -0.4V bias cooldown trace was slightly less stable, but this may be due to experimental variation, as the difference is similar to that between two different cooldowns with no bias on the 60nm quantum dot device. In the 60nm quantum dot, a bias cooldown with $\pm$ 0.2V on the gates improved the stability, with the variance of the peak position decreasing by almost an order of magnitude. In

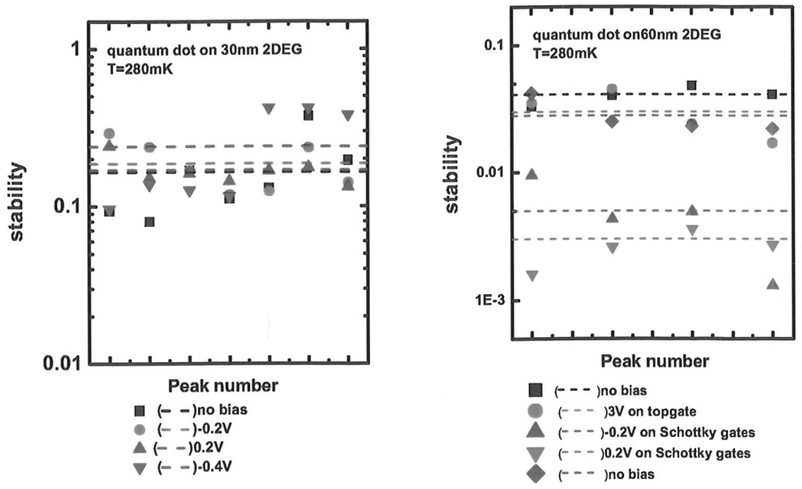

(a)

(b)

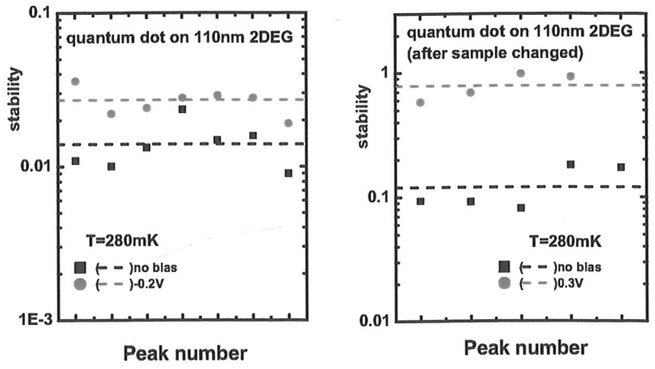

(c)

Figure 4.17: Bias cooldown effects on the stability of quantum dots at 2DEG depths of (a) 30nm, (b) 60nm and (c)110nm. The dashed lines show the average stability value for each cooldown bias. There are two graphs for 110nm as the sample was spiked after the -0.2V bias measurement and was less stable than before.

the 110nm quantum dot, the sample was less stable after bias cooling with both positive and negative voltages.

While this does not allow one to conclude whether bias cooldown is advantageous to obtaining more accurate measurements from induced quantum dots, the fact that both positive and negative voltages have the same effect on stability suggests that in contrast to [97], the source of RTS in this set of undoped quantum dot devices does not come from leakage from the Schottky gates. The fact that the effects of bias cooling change with 2DEG depth suggests that surface states may be playing a role in affecting the device performance.

To have a better insight into what bias cooling can do to device stability, more devices could be measured. To be consistent, the devices should be of the same design, using the same wafers, and measured with the same experimental set up. The extra measurements will give an indication of whether the effects seen so far are due solely to the individual device or are part of a general trend. Different bias voltages could also be tried to investigate whether certain voltage regimes have a more significant effect on device stability than others.

In addition, it would also be interesting to investigate the effects of RTS in undoped quantum wires. The measurements of RTS in doped quantum wires are usually conducted around a conductance of $G = e^2/h$, which is much higher than that of a Coulomb blockade peak in the weak coupling regime. This would yield information as to whether the noise in the measurement circuit noise has any significant effect on the observed device stability.

4.5.2 Other techniques to reduce RTS noise in induced quantum dots

While using to a deeper 2DEG (e.g. 110 nm deep) may offer a slight advantage in a more stable mesoscopic device as compared to a very shallow 2DEG (e.g. 30nm), it is also harder to achieve good definition of the confinement potential due to the spreading out of the electric field. Therefore, it would be worthwhile in future experiments to explore other methods of reducing RTS noise in shallow quantum dots. For example, surface passivation [17] or the choice of insulator may affect how surface states interact with the quantum dot. It may also be

possible to reduce other interactions such as those with ionised impurity atoms by using wafers with an even lower background impurity level.

4.6 Other mesoscopic devices

Besides quantum dots, a large variety of mesoscopic devices can also be made on induced 2DEGs, including quantum wires, Aharonov-Bohm rings, and many more. In this section, some results from a set of quantum wires made on induced 2DEGs are presented. While not intended to be a detailed study on quantum wires, they do showcase the possibilities with undoped devices, including observing zero bias analomy at 300mK, and quantisation plateaus at 1.5K for shallow quantum wires.

4.6.1 Confinement to 1D

By suitably shaping the 2DEG via surface gates, it is possible to obtain a region where electron transport is confined to 1D. In the 1D transport regime, the electrons occupy well defined energy levels known as subbands. Provided that the length of the quantum wire is less than the elastic mean free path, l_e, the motion of electrons is ballistic, i.e. they can travel along occupied 1D subbands without scattering. It can be shown [106] that each occupied subband contributes e^2/h to the overall conductance of the overall system, G, such that

$$G = \frac{e^2}{h}N \tag{4.13}$$

where N is the number of occupied subbands. In zero field, due to spin degeneracy, N is an even integer. Experimentally, this quantisation was first observed in [107], once the resistance of the circuit has been taken into account, and many other experiments have followed since then.

4.6.2 Saddle point potential

To better model a system where the confinement to 1D is provided by the potential from a pair of surface split gates, the saddle point potential is proposed

[108]. In this model, the potential is smooth, and takes the form:

$$V(x,y,z) = V(z) - \frac{1}{2}m^*\omega_x^2 x^2 + \frac{1}{2}m^*\omega_y^2 y^2 \tag{4.14}$$

and the Hamiltonian can be separated into x, y and z components. The confinement potential in the y direction is assumed to be parabolic and gives subband energies of $E_y = \hbar\omega_y(n + 1/2)$.

The saddle point potential model gives a very similar solution to that assuming hard wall potentials. However, the transition between the quantised conductance peaks is now smooth, as illustrated in fig.4.18 , taken from [108]. The transition region between the steps is determined by $\hbar\omega_x$ and thus the quantisation can only be seen if $k_BT << \hbar\omega_x$ and $\hbar\omega_x << \hbar\omega_y$.

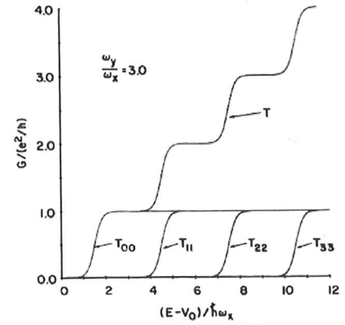

Figure 4.18: The form of the transmission through a quantum wire modelled with the saddle point potential. Taken from [108].

4.6.3 Zero bias anomaly in 1D

While the saddle point potential provides a simple explanation of the effects seen in 1D, it does not take into account electron-electron interactions, and cannot explain effects such as the 0.7 structure [109] and the zero bias anomaly (ZBA) effect [110]. More sophisticated models such as the spin polarisation [111] and Kondo models [112] have been proposed, which predict slightly different effects. The spin polarisation model provides a good explanation for the 0.7 structure,

but not the ZBA, whereas the Kondo model for 1D transport does explain the ZBA, but certain effects such as the variation of the ZBA peaks with temperature does not fit the model [113]. Regardless of whether the theory explains all the observations, experiments seems to indicate that the ZBA is intrinsic to quantum wires, and not due solely to coupling with impurities [113].

4.6.4 Induced quantum wires

Detailed studies on induced quantum wires have been done in [27], and it is not the focus of this work to further those investigations. However, as quantum point contacts are one of the simplest mesoscopic devices to fabricate, several induced quantum wire samples were made at two different 2DEG depths (60nm and 300nm) to explore any fabrication or measurement issues before moving on to more complex devices. The results of this is presented in this section for completeness.

4.6.4.1 Conduction quantisation

Fig.4.19 illustrates the conductance through the two quantum wires on undoped 2DEGs as the split gate voltage is swept. Both wires have the same lithographic dimensions (400nm long and 700nm wide). As one would expect from a 1D channel, the conductance is quantised in units of $2e^2/h$, after the series resistance of the circuit has been taken into account. The length of each quantisation plateau in the 60nm deep quantum wire is much wider than that of the wire on the 300nm deep 2DEG, and the plateau edges are also sharper. This is due to the larger subband spacing on the 60nm quantum wire. In addition, the subband spacing is sufficiently high in the 60nm deep wire that quantisation can be seen at 1.5K, while the quantisation in the deep quantum wire can only be seen at lower temperatures.

4.6.4.2 Subband spacings

Similar to a quantum dot, one can perform a source-drain bias spectroscopy measurement on a quantum wire to measure the energy between the subbands. Fig.4.20 shows bias spectroscopy on the two quantum wires discussed above. The

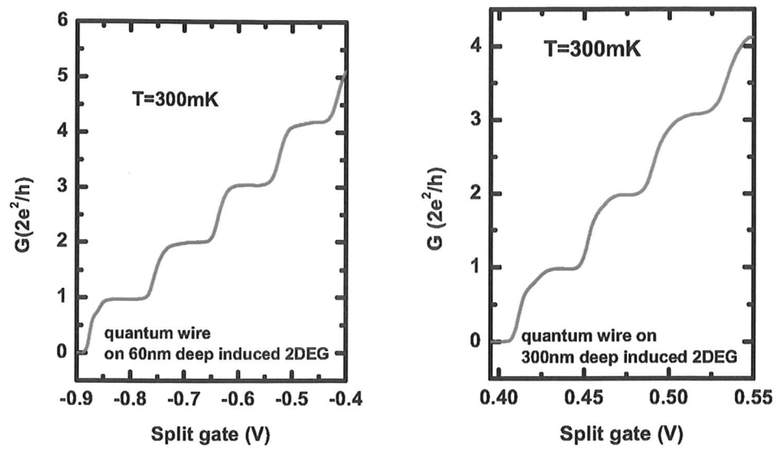

(a) (b)

Figure 4.19: Conductance quantisation in two quantum wires, with a 2DEG depth of (a) 60nm, and (b) 300nm.

wire on the shallower 2DEG has a higher subband energy (2.5meV as opposed to 1meV) due to a stronger confinement.

4.6.4.3 Zeeman splitting

In the quantum wires, the conductance quantisation into units of $2e^2/h$ in zero magnetic field no longer applies as the magnetic field increases. With an increasing magnetic field, the spin degeneracy is lifted, and the quantisation changes to units of e^2/h . This is illustrated in fig.4.21, where the plateau spacing changes to e^2/h quantisation due to the Zeeman splitting.

4.6.4.4 Zero bias anomaly measurement

Instead of sweeping the split gates, one can set up a measurement where the source drain bias is swept at fixed split gate voltages. Fig.4.22 shows this measurement at 300mK for the two quantum wires discussed in the previous section, where the split gate voltage is stepped for a series of traces on the first riser closest to pinch off. In the 60nm deep quantum wire, the zero bias anomaly is seen,

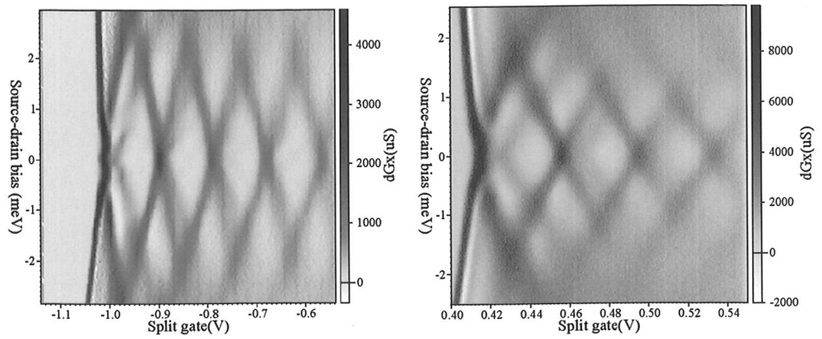

(a) (b)

Figure 4.20: Source-drain bias spectroscopy of two quantum wires, with a 2DEG depth of (a) 60nm, and (b) 300nm. Measurements were done at 300mK.

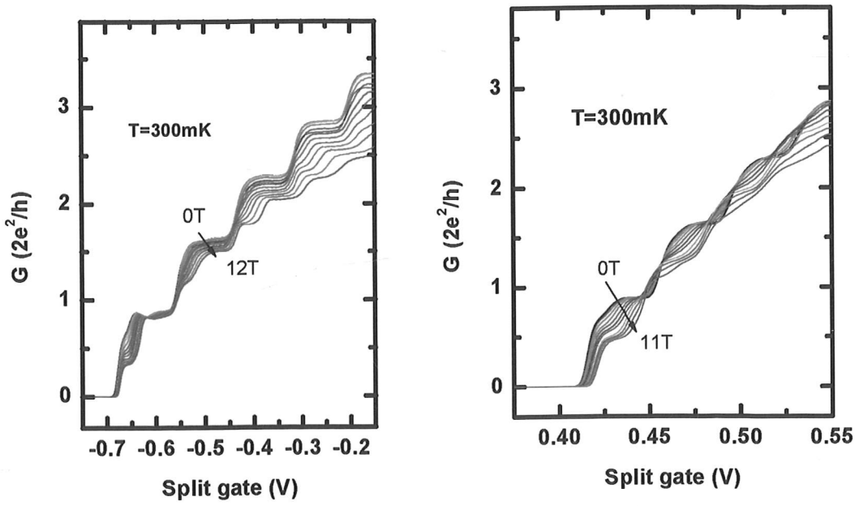

(a) (b)

Figure 4.21: Zeeman splitting in quantum wires of similar dimensions in undoped 2DEGs of depth (a) 60nm, and (b) 300nm. The resistances shown are as measured, and have not been corrected for series resistance.

whereas for the deeper quantum wire, there is no ZBA peak. This difference is not entirely unexpected, as the 60nm deep quantum wire has a greater subband spacing compared to the 300nm deep quantum wire, and the effect would not be smeared out by thermal broadening as easily.

In [27], there does not seem to be a correlation between the height of the ZBA peak and subband spacing. While it is not possible to test this at 300mK, colder temperatures may yield further insight. In addition, by using very shallow 2DEGs, it should be possible to test a wider range of subband spacings.

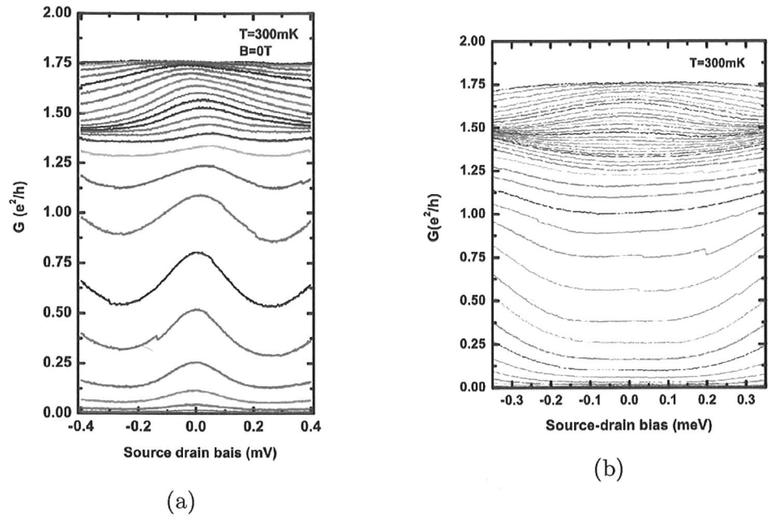

(a) (b)

Figure 4.22: Sweeping the source-drain bias of two quantum wires at various split gate voltages near the pinch off. The 2DEG depth of (a) is 60nm, and (b) is 300nm.

4.7 Summary

In this chapter, I have discussed measurements on undoped mesoscopic devices, with the focus on quantum dot devices that show single level transport at 300mK. With the developments in processing, it is possible to obtain gated quantum dot devices on induced 2DEGs that are only 30nm below the surface of the wafer.

Undoped quantum dots on 2DEGs of greater depth can also be made after suitable modification of the lithographic dimensions of the Schottky gates . On comparing deeper devices with those that are 30nm, it was found that 60nm devices are more stable than their 30nm counterparts, but there is no further improvement in going beyond 60nm. The bias cooling technique was also tried on three undoped quantum dot devices at three different depths. While bias cooling does not affect the operating voltages of the Schottky gates defining the 0D region, it does have an effect on the device stability. However, as it improves the stability in the 60nm deep device but worsens the stability in the 30nm and 110nm deep devices, the precise effect of bias cooling on undoped quantum dots is still up for debate. The chapter finishes with a brief discussion on quantum wires on both shallow and deep undoped 2DEGs.

Chapter 5

Conclusions and the road ahead

5.1 Conclusions

In this thesis, I have discussed why one may want to used undoped GaAs/AlGaAs semiconductor heterostructures as a basis for investigating electron transport, and have presented developments in fabrication technique that enable one to contact very shallow undoped 2DEGs, as well as achieving very low resistance ohmic contacts. The experiments discussed showcase the wide range of investigations for which one can use induced devices. From investigating Fractional Quantum Hall effects to characterising the background impurity levels of MBE grown wafers, from simple mesoscopic devices such as quantum wires, to more complex zero dimensional systems such as quantum dots, not only can one replicate on induced samples experiments normally done on doped samples, induced samples can also offer a better insight into the intrinsic nature of transport properties due to the lack of intentional dopants.

5.2 Future work

In the previous chapters, I have suggested extensions to the experiments presented in this thesis. However, there are many areas in which undoped devices would perform well. The following are a few examples of potential experiments on undoped samples which may yield some very interesting insights.

5.2.1 More complex experiments with the 5/2 fractional quantum hall state

The exact nature of the 5/2 Fractional Quantum Hall state is still under debate. While experimental progress is being made, there are still obstacles to the observation of the state due to the requirements for very clean systems and very low electron temperatures.

Undoped systems will hopefully offer a simpler system for the investigation of the 5/2 FQHE. Once wafer and device design have been optimised, and electron temperatures lowered, it should be possible to observe a fully developed 5/2 FQHE in undoped samples. This can lead to experiments complementing those done in doped samples, especially as one can study the density and/or mobility dependence of these effects. Some examples may be probing the 5/2 state with tilted magnetic field experiments to investigate the change in the 5/2 resistance minimum and gain an understanding of factors such as the nature of the 5/2 ground state [114]; using interferometers on the 5/2 state, in which non-Abelian particles are predicted to show oscillations corresponding to charges of $e/2$ and $e/4$ [115]; single electron transistors to probe the 5/2 state, and many more.

5.2.2 Towards high temperature operation

Through the development of wafer structure, it may be possible to obtain induced devices that work at liquid nitrogen, or even higher, temperatures. Besides the possibility of conducting experiments at temperatures that are more easily accessible (e.g. using liquid nitrogen), higher temperature operation may also lead to practical applications. One example is ambipolar devices, which are very difficult, if not impossible, to make using doped samples. Recent work [83] has shown working induced ambipolar devices, and higher temperature operation of such samples could complement graphene ambipolar devices such as those in [116, 117]. The fact that induced ambipolar devices have a voltage range around 0V in which the sample does not conduct (i.e. a well defined 'off' state) could potentially give them an advantage over their graphene counterparts.

5.2.3 Double quantum wires

Double quantum wires offer the potential to prove whether the ZBA in quantum wires arises from a Kondo interaction. In a double quantum dot system, the Kondo effect results in a split peak in the ZBA. The analogy of this in 1D is a double quantum wire system. If each wire shows a non-split ZBA peak when electrons are flowing through only one wire, and a split ZBA peak when transport is going through both of them, then this is a good indication that the ZBA in quantum wires is due to the Kondo effect, and has an associated bound state.

This experiment will be more conclusive in an undoped system due to the smaller number of impurities, as the Kondo effect can also arise if the 1D system couples to impurities.

5.2.4 Double quantum dots on undoped 2DEGs/2DHGs

In double quantum dots on doped 2DEGs, two major sources of decoherence are RTS noise and the interaction with the spins of the nuclei. Undoped samples, with a cleaner system, are less likely to suffer from RTS noise; thus it may be possible to extend the decoherence times in an undoped double dot system. Recent work in undoped Si/SiGe structures [118] has found that a double dot made on this structure has a much longer decoherence time compared to doped structures, and it should be possible to extend this to undoped structures based on GaAs.

To extend the coherence times even more, one can use holes, as these do not interact with the nuclei spin. Double hole quantum dots may be a promising route towards a quantum dot based qubit. Of course, there remains significant challenges before an undoped hole quantum dot can be realised. Holes, with their higher mass, would require finer features, thus limiting the depth at which the hole gas can be. Processing p-type ohmics on undoped samples would also need to be optimised in order to achieve reliable contacts to very shallow 2DHGs.

Appendix A

Sample Fabrication

A.0.5 Mesa

1. Premix 1:1:20 H_3PO_4:H_2O_2:H_2O solution and leave for at least 1 hour before using.
2. Bake chip on 125°C hotplate 2 minutes.
3. Spin 1813 resist 60s at 5500rpm.
4. Bake chip on 115°C hotplate 1 minutes.
5. Expose mesa layer for 6.5 seconds on the Orange Karl-Suss mask aligner.
6. Develop in MF319 Developer until pattern becomes clear.
7. Rinse in DI water at least 60s.
8. Dry with N_2 gas.
9. RF ash 60s.
10. 30s dip in 20% HCl, rinse in DI water.
11. Etch sample in 1:1:20 H_3PO_4:H_2O_2:H_2O solution for 150s to obtain a mesa of approximately 500nm in height.

12. Measure depth of the etch to have a calibration of the etch rate.

A.0.6 Ohmics

The ohmic contacts are necessary to contact the outside world, and they should have low resistance in order to obtain good measurement results. As opposed to doped samples, ohmic contacts in undoped samples are recessed. Therefore, a test chip is necessary to calibrate the etch rate of the etch solution, as obtaining an accurate depth in the ohmic pit is important for good ohmic contacts. The processing details are as follows:

1. Bake chip on 125°C hotplate 2 minutes.
2. Spin 1813 resist 60s at 5500rpm.
3. Bake chip on 115°Chotplate 1 minutes.
4. Expose ohmics layer for 6.5 seconds on the Orange Karl-Suss mask aligner.
5. Develop in MF319 Developer until pattern becomes clear.
6. Rinse in DI water at least 60s.
7. Dry with N_2 gas.
8. RF ash 60s.
9. 30s dip in 20% HCl, rinse in DI water.
10. Etch test chip in 1:1:20 H_3PO_4:H_2O_2:H_2O solution, aiming for 350nm in depth if the wafer being processed has an AlGaAs/GaAs interface at 300nm below the surface, or 300nm in depth if the interface is closer than 300nm to the surface.
11. Measure depth of the etch to have a calibration of the etch rate.
12. Using calibrated etch rates, etch actual sample.
13. Microwave ash sample, 110s on low power with Si wafer.

14. 30s dip in 20% HCl, rinse in DI water.
15. Load immediately into layered ohmics evaporator. A rotatilt is used, with the sample holder being at 60 degrees away from horizontal.
16. Load 220mg Au,28mg Ge into one boat, and a large quantity of Ni into a ceramic boat.
17. Pump evaporator chamber down to $\leq 3x10^{-7}$mbar.
18. Premelt the AuGe mixture.
19. Metal deposition: start the rotatilt, evaporate 10nm Ni, followed by all of the Au and Ge mixture, finally 120nm of Ni. Ensure that the pressure inside the chamber is $\leq 2x10^{-6}$mbar.
20. Wait 30 minutes for the evaporator to cool, then take out samples and place in acetone immediately for liftoff.
21. After liftoff, rinse samples in propanol and dry with N_2 gas.
22. Anneal at 470°C for 120s in forming gas.

A.0.7 Electron beam lithography gates

1. Bake chip on 125°C hotplate 2 minutes.
2. Spin 1:1 495K A5 PMMA:MIBK 4000rpm 60s.
3. chip on 150°C hotplate 20 minutes.
4. Spin 1:5 950K A11 PMMA:MIBK 6000rpm 60s.
5. Bake chip on 125°C hotplate 20 minutes.
6. Pattern written by electron beam.
7. Develop in IPA:MIBK:MEK 15:5:1 for 6-8s.
8. Rinse in propanol for 60s.

9. Dry with N_2 gas.
10. Check that pattern has developed cleanly.
11. Load into evaporator, and ensure pressure inside chamber is $\leq 3x10^{-7}$mbar before metal deposition.
12. Deposit 18nm Ti, 25nm Au. Ensure that the pressure during the Ti evaporation is $\leq 3x10^{-7}$mbar, and the rate of evaporation for Au is $\leq 0.2nms^{-1}$.
13. Place samples into acetone for liftoff. This usually takes several hours.
14. Rinse in propanol, dry with N_2 gas.

A.0.8 Optical surface gates

1. Bake chip on 125°C hotplate 2 minutes.
2. Spin 495K PMMA 4000rpm 60s.
3. Bake chip on 150°C hotplate 20 minutes.
4. Spin 1805 photoresist 6000rpm 60s.
5. Bake chip on 125°C hotplate 2 minutes.
6. Expose topgate layer for 3.5 seconds on the Orange Karl-Suss mask aligner.
7. Develop in MF319 Developer until pattern becomes clear.
8. Rinse in DI water at least 60s.
9. Dry with N_2 gas.
10. Place in ozone asher for 30 minutes.
11. Develop in IPA:MIBK:MEK 15:5:1 for 10s[1].

[1]The development time still has to be optimised, as some samples had problems with the optical surface gates shorting to the topgate, possibly due to the liftoff not being very sharp.

12. Rinse in propanol for 60s.
13. Dry with N_2 gas.
14. RF ash 45s.
15. Optional step: Dip in 20% HCl, rinse DI water, dry N_2 gas.
16. Load evaporator, and ensure pressure inside chamber is $\leq 3x10^{-7}$mbar before metal deposition.
17. Deposit 18nm Ti, 30nm Au. Ensure that the pressure during the Ti evaporation is $\leq 3x10^{-7}$mbar, and the rate of evaporation for Au is $\leq 0.2nms^{-1}$.
18. Place samples into acetone for liftoff. Metal should come off easily.

A.0.9 Insulator

The insulator can be either polyimide or SiO_2.
For polyimide:

1. Take out a bottle of 3:1 polyimide:thinner mixture from fridge to warm to room temperature, approximately 5 mins.
2. Check the humidity inside spinner compartment. If it is $\geq$ 45%, vent the compartment with N_2 gas to ensure that it is at a low humidity when it is spun on.
3. Bake chip on 125°C hotplate 2 minutes.
4. Spin the polyimide 10s at 500rpm, then ramp up to 6500rpm for 60s.
5. Bake chip on 90°C hotplate 3 minutes.
6. Expose polyimide layer for 70 seconds on the Orange Karl-Suss mask aligner.
7. Wait 5 minutes, then bake chip on 80°C hotplate for 1 minute.
8. Develop in polyimide developer 30s, rinse in polyimide rinse for 30s, dry N_2 gas.

9. Cure in furnance: Bake at 150°C 0.2 hour, ramp to 200°C, and bake for 0.5 hour, then ramp to 300°C and bake for 1 hour. Ramp down to room temperature.

For SiO2:

1. Deposit 200nm SiO2 with PCVD at 300°C.
2. Bake chip on 125°C hotplate 2 minutes.
3. Spin 1813 resist 60s at 5500rpm.
4. Bake chip on 115°Chotplate 1 minutes.
5. Expose SiO2 layer for 6.5 seconds on the Orange Karl-Suss mask aligner.
6. Develop in MF319 Developer until pattern becomes clear.
7. Rinse in DI water at least 60s.
8. Dry with N_2 gas.
9. Etch away the SiO2 from unwanted areas with buffer HF.

A.0.10 Topgate

1. Bake chip on 125°C hotplate 2 minutes.
2. Spin 495K PMMA 4000rpm 60s.
3. Bake chip on 150°C hotplate 20 minutes.
4. Spin neat 495K A5 PMMA 4000rpm 60s (This is the second layer of PMMA to ensure there is enough height for liftoff).
5. Bake chip on 150°C hotplate 20 minutes.
6. Spin 1805 photoresist 6000rpm 60s.
7. Bake chip on 125°C hotplate 2 minutes.

8. Expose topgate layer for 3.5 seconds on the Orange Karl-Suss mask aligner.
9. Develop in MF319 Developer until pattern becomes clear.
10. Rinse in DI water at least 60s.
11. Dry with N_2 gas.
12. Place in ozone asher for 30minutes.
13. Develop in IPA:MIBK:MEK 15:5:1 for 10s.
14. Rinse in propanol for 60s.
15. Dry with N_2 gas.
16. RF ash 45s.
17. Optional step: Dip in 20% HCl, rinse DI water, dry N_2 gas.
18. Load evaporator, using the rotatilt, and ensure pressure inside chamber is $\leq 3x10^{-7}$mbar
19. Deposit 30nm Ti, 150nm Au. Ensure that the pressure during the Ti evaporation is $\leq 3x10^{-7}$mbar.
20. Place samples into acetone for liftoff. Metal should come off easily.

A.0.11 Bonding

1. Cleave chip into separate devices.
2. Mount samples onto chip carrier (LCC) package with g-varnish.
3. Bond device to chip package. For samples with fine electron beam gates, ensure that the 'auto spark' is off, that the ionised air blower is turned on, and to leave 60s between each bond. It is also advisable to put a folded piece of Al underneath the LCC package, to ensure good contact between the pads of the package such that all the bonded gates are at the same potential.

References

[1] V. Umansky, M. Heiblum, Y. Levinson, J.; Smet, J. Nuebler, and M. Dolev. MBE growth of ultra-low disorder 2DEG with mobility exceeding 35x10^6 cm^2/Vs. *Journal of Crystal Growth*, 311(7):1658 – 1661, 2009.

[2] H.L. Stormer, R. Dingle, A.C. Gossard, W. Wiegmann, and M.D. Sturge. Two-dimensional electron gas at a semiconductor-semiconductor interface. *Solid State Communications*, 29(10):705 – 709, 1979.

[3] R. H. Harrell, K. S. Pyshkin, M. Y. Simmons, D. A. Ritchie, C. J. B. Ford, G. A. C. Jones, and M. Pepper. Fabrication of high-quality one- and two-dimensional electron gases in undoped GaAs/AlGaAs heterostructures. *Appl. Phys. Lett.*, 74(16):2328–2330, 1999.

[4] C.W.J. Beenakker and H. van Houten. Quantum transport in semiconductor nanostructures. In Henry Ehrenreich and David Turnbull, editors, *Semiconductor Heterostructures and Nanostructures*, volume 44 of *Solid State Physics*, pages 1 – 228. Academic Press, 1991.

[5] John H. Davies. *The Physics of Low-Dimensional Systems.* Cambridge University Press, 1998.

[6] P. Atkinson. PhD thesis, University of Cambridge, 2002.

[7] I. Farrer. *Growth and Applications of Self-Assembled Quantum Dots.* PhD thesis, University of Cambridge, 2001.

[8] W. Pan, J. S. Xia, H. L. Stormer, D. C. Tsui, C. Vicente, E. D. Adams, N. S. Sullivan, L. N. Pfeiffer, K. W. Baldwin, and K. W. West. Experimental

studies of the fractional quantum hall effect in the first excited landau level. *Phys. Rev. B*, 77:075307, Feb 2008.

[9] J. P. Eisenstein, K. B. Cooper, L. N. Pfeiffer, and K. W. West. Insulating and fractional quantum hall states in the first excited landau level. *Phys. Rev. Lett.*, 88:076801, Jan 2002.

[10] M. A. Zudov, R. R. Du, L. N. Pfeiffer, and K. W. West. Evidence for a new dissipationless effect in 2D electronic transport. *Phys. Rev. Lett.*, 90:046807, Jan 2003.

[11] A. T. Hatke, M. A. Zudov, J. D. Watson, and M. J. Manfra. Magnetoplasmon resonance in a two-dimensional electron system driven into a zero-resistance state. *Phys. Rev. B*, 85:121306, Mar 2012.

[12] B.A. Piot, Z. Jiang, C.R. Dean, L.W. Engel, G. Gervais, L.N. Pfeiffer, and K. West. Wigner crystallization in a quasi-three-dimensional electronic system. *Nature Physics*, 4:936–939, 2008.

[13] L. Pfeiffer and K.W West. The role of MBE in recent quantum hall effect physics discoveries. *Physica E: Low-dimensional Systems and Nanostructures*, 20:57 – 64, 2003.

[14] G. Snider. 1D Poisson-Schroedinger Solver. online at http://www.nd.edu/ gsnider/.

[15] J. Huang, D. S. Novikov, D. C. Tsui, L. N. Pfeiffer, and K. W. West. Nonactivated transport of strongly interacting two-dimensional holes in GaAs. *Phys. Rev. B*, 74:201302, Nov 2006.

[16] R. Nemutudi, M. Kataoka, C. J. B. Ford, N. J. Appleyard, M. Pepper, D. A. Ritchie, and G. A. C. Jones. Noninvasive lateral detection of coulomb blockade in a quantum dot fabricated using atomic force microscopy. *J. Appl. Phys.*, 95(5):2557–2559, 2004.

[17] G. Kopnov, V. Y. Umansky, H. Cohen, D. Shahar, and R. Naaman. Effect of the surface on the electronic properties of a two-dimensional electron gas as measured by the quantum hall effect. *Phys. Rev. B*, 81:045316, Jan 2010.

[18] D. Laroche, S. Das Sarma, G. Gervais, M. P. Lilly, and J. L. Reno. Scattering mechanism in modulation-doped shallow two-dimensional electron gases. *Appl. Phys. Lett.*, 96:162112, 2010.

[19] A. J. M. Giesbers, U. Zeitler, M. I. Katsnelson, D. Reuter, A. D. Wieck, G. Biasiol, L. Sorba, and J. C. Maan. Correlation-induced single-flux-quantum penetration in quantum rings. *Nature Physics*, 6:173–177, 2010.

[20] C. Rossler, B. Küng, S. Drüscher, T. Choi, T. Ihn, K. Ensslin, and M. Beck. Highly tunable hybrid quantum dots with charge detection. *Appl. Phys. Lett.*, 97:152109, 2010.

[21] R. Nemutudi, C-T. Liang, M. J. Murphy, H. E. Beere, C. G. Smith, D. A. Ritchie, M. Pepper, and G. A. C. Jones. *Microelectronics Journal*, 36:425, 2005.

[22] S. Nakamura, Y. Yamauchi, M. Hashisaka, K. Chida, K. Kobayashi, T. Ono, R. Leturcq, K. Ensslin, K. Saito, Y. Utsumi, and A. C. Gossard. Nonequilibrium fluctuation relations in a quantum coherent conductor. *Phys. Rev. Lett.*, 104:080602, 2010.

[23] A. E. Gildemeister, T. Ihn, R. Schleser, K. Ensslin, D. C. Driscoll, and A. C. Gossard. Imaging a coupled quantum dot-quantum point contact system. *J. Appl. Phys.*, 102:083703, 2007.

[24] A. Mühle, W. Wegscheider, and R. J. Haug. Quantum dots formed in a GaAs/AlGaAs quantum ring. *Appl. Phys. Lett.*, 92:013126, 2008.

[25] C. Fricke, F. Hohls, W. Wegscheider, and R. J. Haug. Bimodal counting statistics in single-electron tunneling through a quantum dot. *Phys. Rev. B*, 76:155307, 2007.

[26] D. Goldhaber-Gordon, H. Shtrikman, D. Mahalu, D. Abusch-Magder, U. Meirav, and M. A. Kastner. Kondo effect in a single-electron transistor. *Nature*, 391:156, 1998.

[27] S. Sarkozy. *Mesoscopic Transport in Undoped Heterostructure*. PhD thesis, University of Cambridge, August 2008.

[28] R.H. Harrell. *Induced Electron gases in undoped GaAs/AlGaAs.* PhD thesis, University of Cambridge, 1998.

[29] T. Ihn. *Semiconductor Nanostructures.* Oxford University Press, 2010.

[30] A. B. Fowler, T. Ando, and F. Stern. Electronic properties of two dimensional systems. *Reviews of Modern Physics*, 54(2):437–672, Apr. 1982.

[31] D. Kozlov, Z. Kvon, A. Kalagin, and A. Toropov. Properties of 2D electron gas in AlGaAs/GaAs heterojunctions with thin AlGaAs layers. *Semiconductors*, 41:180–183, 2007.

[32] G.E. Stillman and C.M. Wolfe. Electrical characterization of epitaxial layers. *Thin Solid Films*, 31(1-2):69 – 88, 1976.

[33] E. E. Mendez, P. J. Price, and M. Heiblum. Temperature dependence of the electron mobility in GaAs/AlGaAs heterostructures. *Appl. Phys. Lett.*, 45(3):294–296, 1984.

[34] B. Yang, Y. Cheng, Z.G. Wang, J. Liang, Q. Liao, L. Lin, Z. Zhu, B. Xu, and W. Li. Interface roughness scattering in GaAs/AlGaAs modulation-doped heterostructures. *Appl. Phys. Lett.*, 65(26):3329–3331, 1994.

[35] S. B. Ogale and A. Madhukar. Alloy disorder scattering contribution to low-temperature electron mobility in semiconductor quantum well structures. *J. Appl. Phys.*, 56(2):368–374, 1984.

[36] Tsuneya A. Self-consistent results for a GaAs/$Al_xGa_{1-x}As$ heterojunction. ii low temperature mobility. *Journal of the Physical Society of Japan*, 51(12):3900–3907, Dec. 1982.

[37] V. Umansky, R. de Picciotto, and M. Heiblum. Extremely high-mobility two dimensional electron gas: Evaluation of scattering mechanisms. *Appl. Phys. Lett.*, 71(5):683 –685, Aug 1997.

[38] D. V. Lang. Deep-level transient spectroscopy: A new method to characterize traps in semiconductors. *J. Appl. Phys.*, 45(7):3023–3032, 1974.

[39] Timothy H. Gfroerer. *Photoluminescence in Analysis of Surfaces and Interfaces.* John Wiley & Sons, Ltd, 2006.

[40] S. Sarkozy, K. Das Gupta, C. Siegert, A. Ghosh, M. Pepper, I. Farrer, H. E. Beere, D. A. Ritchie, and G. A. C. Jones. Low temperature transport in undoped mesoscopic structures. *Appl. Phys. Lett.*, 94(17):172105, 2009.

[41] W. R. Clarke, A. P. Micolich, A. R. Hamilton, M. Y. Simmons, K. Muraki, and Y. Hirayama. Fabrication of induced two-dimensional hole systems on (311)A GaAs. *J. Appl. Phys.*, 99(2):023707, 2006.

[42] S. J. MacLeod, K. Chan, T. P. Martin, A. R. Hamilton, A. See, A. P. Micolich, M. Aagesen, and P. E. Lindelof. Role of background impurities in the single-particle relaxation lifetime of a two-dimensional electron gas. *Phys. Rev. B*, 80:035310, Jul 2009.

[43] C. T. Foxon, J. J. Harris, D. Hilton, J. Hewett, and C. Roberts. Optimisation of (Al,Ga)As/GaAs two-dimensional electron gas structures for low carrier densities and ultrahigh mobilities at low temperatures. *Semicond. Sci. Technol.*, (4):582, 1989.

[44] G. Weimann and W. Schlapp. Molecular beam epitaxial growth and transport properties of modulation-doped AlGaAs-GaAs heterostructures. *Appl. Phys. Lett.*, 46(4):411–413, 1985.

[45] K. Das Gupta, A. F. Croxall, W. Y. Mak, H. E. Beere, C. A. Nicoll, I. Farrer, F. Sfigakis, and D. A. Ritchie. Linear non-hysteretic gating of a very high density 2DEG in an undoped metalsemiconductormetal sandwich structure. *Semicond. Sci. Technol.*, 27(11):242107, 2010.

[46] A. Kastalsky and J.C.M. Hwang. Study of persistent photoconductivity effect in n-type selectively doped AlGaAs/GaAs heterojunction. *Solid State Communications*, 51(5):317 – 322, 1984.

[47] D. V. Lang and R. A. Logan. Large-lattice-relaxation model for persistent photoconductivity in compound semiconductors. *Phys. Rev. Lett.*, 39:635–639, Sep 1977.

[48] D. V. Lang, R. A. Logan, and M. Jaros. Trapping characteristics and a donor-complex (DX) model for the persistent-photoconductivity trapping center in Te-doped $Al_xGa_{1-x}As$. *Phys. Rev. B*, 19:1015–1030, Jan 1979.

[49] C. S. Chang, H. R. Fetterman, D. Ni, E. Sovero, B. Mathur, and W. J. Ho. Negative photoconductivity in high electron mobility transistors. *Appl. Phys. Lett.*, 51(26):2233–2235, 1987.

[50] D. E. Lacklison, J. J. Harris, C. T. Foxon, J. Hewett, D. Hilton, and C. Roberts. A comparison of photoconduction effects in (Al, Ga)As and GaAs/(Al, Ga)As heterostructures. *Semicond. Sci. Technol.*, 3(7):633, 1988.

[51] M. Hayne, A. Usher, J.J. Harris, and C.T. Foxon. An elegant verification of the negative charge-state of the DX centre from mobility measurements of 2d electrons. *Surface Science*, 361362(0):574 – 578, 1996.

[52] T. Saku, K. Muraki, and Y. Hirayama. High-mobility two-dimensional electron gas in an undoped heterostructure: Mobility enhancement after illumination. *Jpn. J. Appl. Phys.*, 37:L765–L767, 1998.

[53] Y. Hirayama, K. Muraki, A. Kawaharazuka, K. Hashimoto, and T. Saku. Backgated layers and nanostructures. *PhysicaE*, 11:155–160, 2001.

[54] P.T. Coleridge. Correlation lengths for scattering potentials in two-dimensional electron gases. *Semicond. Sci. Technol.*, 12:22, 1996.

[55] A. R. Long, J. H. Davies, M. Kinsler, S. Vallis, and M. C. Holland. A simple model for the characteristics of GaAs/AlGaAs modulation-doped devices. *Semicond. Sci. Technol.*, 8:1581, 1993.

[56] S. W. Lin, J. Du, C. Balocco, Q. P. Wang, and A. M. Song. Effects of bias cooling on charge states in heterostructures embedding self-assembled quantum dots. *Phys. Rev. B*, 78:115314, Sep 2008.

[57] K. von Klitzing, G. Dorda, and M. Pepper. New method for high-accuracy determination of the fine-structure constant based on quantized hall resistance. *Phys. Rev. Lett.*, 45:494–497, Aug 1980.

[58] M. Büttiker. Absence of backscattering in the quantum hall effect in multiprobe conductors. *Phys. Rev. B*, 38:9375–9389, Nov 1988.

[59] B. I. Halperin. Quantized hall conductance, current-carrying edge states, and the existence of extended states in a two-dimensional disordered potential. *Phys. Rev. B*, 25:2185–2190, Feb 1982.

[60] D. C. Tsui, H. L. Stormer, and A. C. Gossard. Two-dimensional magnetotransport in the extreme quantum limit. *Phys. Rev. Lett.*, 48:1559–1562, May 1982.

[61] R. B. Laughlin. Anomalous quantum hall effect: An incompressible quantum fluid with fractionally charged excitations. *Phys. Rev. Lett.*, 50:1395–1398, May 1983.

[62] J. K. Jain. Composite-fermion approach for the fractional quantum hall effect. *Phys. Rev. Lett.*, 63:199–202, Jul 1989.

[63] R. Willett, J. P. Eisenstein, H. L. Störmer, D. C. Tsui, A. C. Gossard, and J. H. English. Observation of an even-denominator quantum number in the fractional quantum hall effect. *Phys. Rev. Lett.*, 59:1776–1779, Oct 1987.

[64] G. Moore and N. Read. Nonabelions in the fractional quantum hall effect. *Nuclear Physics B*, 360:362 – 396, 1991.

[65] Pui K. Lam and S. M. Girvin. Liquid-solid transition and the fractional quantum-hall effect. *Phys. Rev. B*, 30:473–475, Jul 1984.

[66] S. Das Sarma, M. Freedman, and C. Nayak. Topologically protected qubits from a possible non-abelian fractional quantum hall state. *Phys. Rev. Lett.*, 94:166802, Apr 2005.

[67] Ady Stern. Non-abelian states of matter. *Nature*, 464:187–193, March 2010.

[68] J. Nuebler, V. Umansky, R. Morf, M. Heiblum, K. von Klitzing, and J. Smet. Density dependence of the $\nu = \frac{5}{2}$ energy gap: Experiment and theory. *Phys. Rev. B*, 81:035316, Jan 2010.

[69] H. C. Choi, W. Kang, S. Das Sarma, L. N. Pfeiffer, and K. W. West. Activation gaps of fractional quantum hall effect in the second landau level. *Phys. Rev. B*, 77:081301, Feb 2008.

[70] W. Pan, H.L. Stormer, D.C. Tsui, L.N. Pfeiffer, K.W. Baldwind, and K.W. West. Experimental evidence for a spin-polarized ground state in the ν= 5/2 fractional quantum hall effect. *Solid State Communications*, 119:641–645, 2001.

[71] W. Pan, N. Masuhara, N. S. Sullivan, K. W. Baldwin, K. W. West, L. N. Pfeiffer, and D. C. Tsui. Impact of disorder on the ν= 5/2 fractional quantum hall state. *Physics Review Letters*, 106:206806, 2011.

[72] C. Attaccalite, S. Moroni, P. Gori-Giorgi, and G. B. Bachelet. Correlation energy and spin polarization in the 2D electron gas. *Phys. Rev. Lett.*, 88:256601, Jun 2002.

[73] Y. P. Chen, G. Sambandamurthy, Z. H. Wand, R. M. Lewis, L. W. Engel, D. C. Tsui, P. D. Ye, L. N. Pfeiffer, and K. W. West. Correlation energy and spin polarization in the 2D electron gas. *Nature*, 2:452, Jun 2006.

[74] N. D. Drummond and R. J. Needs. Phase diagram of the low-density two-dimensional homogeneous electron gas. *Phys. Rev. Lett.*, 102:126402, Mar 2009.

[75] B. Tanatar and D. M. Ceperley. Ground state of the two-dimensional electron gas. *Phys. Rev. B*, 39:5005–5016, Mar 1989.

[76] M. J. Manfra, E. H. Hwang, S. Das Sarma, L. N. Pfeiffer, K. W. West, and A. M. Sergent. Transport and percolation in a low-density high-mobility two-dimensional hole system. *Phys. Rev. Lett.*, 99:236402, Dec 2007.

[77] S. Faniel, L. Moldovan, A. Vlad, E. Tutuc, N. Bishop, S. Melinte, M. Shayegan, and V. Bayot. In-plane magnetic-field-induced metal-insulator transition in (311)A GaAs two-dimensional hole systems probed by thermopower. *Phys. Rev. B*, 76:161307, Oct 2007.

[78] John A. Nixon and John H. Davies. Potential fluctuations in heterostructure devices. *Phys. Rev. B*, 41:7929–7932, Apr 1990.

[79] A. Palevski, M.L. Rappaport, A. Kapitulnik, A. Fried, and G. Deutscher. Hall coefficient and conduction in a 2D percolation system. *Journal Physique Letters*, 45:367, Apr 1984.

[80] J. Yoon, C. C. Li, D. Shahar, D. C. Tsui, and M. Shayegan. Wigner crystallization and metal-insulator transition of two-dimensional holes in GaAs at B=0. *Phys. Rev. Lett.*, 82:1744–1747, Feb 1999.

[81] W. Walukiewicz, H. E. Ruda, J. Lagowski, and H. C. Gatos. Electron mobility in modulation-doped heterostructures. *Phys. Rev. B*, 30:4571–4582, Oct 1984.

[82] K. S. Novoselov, A. K. Geim, S. V. Morozov, D. Jiang, Y. Zhang, S. V. Dubonos, I. V. Grigorieva, and A. A. Firsov. Electric field effect in atomically thin carbon films. *Science*, 306(5696):666–669, 2004.

[83] J. C. H. Chen, D. Q. Wang, O. Klochan, A. P. Micolich, K. Das Gupta, F. Sfigakis, D. A. Ritchie, D. Reuter, A. D. Wieck, and A. R. Hamilton. Fabrication and characterization of ambipolar devices on an undoped AlGaAs/GaAs heterostructure. *Appl. Phys. Lett.*, 100(5):052101 –052101–3, jan 2012.

[84] A. F. Croxall, B. Zheng, F. Sfigakis, K. Das Gupta, I. Farrer, C. A. Nicoll, H. E. Beere, and D. A. Ritchie. Demonstration and characterization of an ambipolar high mobility transistor in an undoped GaAs/AlGaAs quantum well. *Appl. Phys. Lett.*, 2013. submitted.

[85] C. W. J. Beenakker. Theory of coulomb-blockade oscillations in the conductance of a quantum dot. *Phys. Rev. B*, 44:1646–1656, July 1991.

[86] C. G. Smith. Low-dimensional quantum devices. *Reports on Progress in Physics*, 59(2):235, 1996.

[87] D. Leonard, M. Krishnamurthy, C. M. Reaves, S. P. Denbaars, and P. M. Petroff. Direct formation of quantum-sized dots from uniform coherent islands of InGaAs on GaAssurfaces. *Appl. Phys. Lett.*, 63(23):3203–3205, 1993.

[88] M. Bockrath, D. H. Cobden, P. L. McEuen, N. G. Chopra, A. Zettl, A. Thess, and R. E. Smalley. Single-electron transport in ropes of carbon nanotubes. *Science*, 275(5308):1922–1925, 1997.

[89] M. A. Reed, J. N. Randall, R. J. Aggarwal, R. J. Matyi, T. M. Moore, and A. E. Wetsel. Observation of discrete electronic states in a zero-dimensional semiconductor nanostructure. *Phys. Rev. Lett.*, 60:535–537, Feb 1988.

[90] E. B. Foxman, P. L. McEuen, U. Meirav, Ned S. Wingreen, Yigal Meir, Paul A. Belk, N. R. Belk, M. A. Kastner, and S. J. Wind. Effects of quantum levels on transport through a coulomb island. *Phys. Rev. B*, 47:10020–10023, Apr 1993.

[91] H. Grabert and M. H. Devoret, editors. *Single Charge Tunnelling Coulomb Blockade Phenomena in Nanostructures*, volume 294 of *B*. Plenum, 1991.

[92] U. Meirav, M. A. Kastner, and S. J. Wind. Single-electron charging and periodic conductance resonances in gaas nanostructures. *Phys. Rev. Lett.*, 65:771–774, Aug 1990.

[93] E. B. Foxman, U. Meirav, P. L. McEuen, M. A. Kastner, O. Klein, P. A. Belk, D. M. Abusch, and S. J. Wind. Crossover from single-level to multilevel transport in artificial atoms. *Phys. Rev. B*, 50:14193–14199, Nov 1994.

[94] Y. Meir, N. S. Wingreen, and P. A. Lee. Transport through a strongly interacting electron system: Theory of periodic conductance oscillations. *Phys. Rev. Lett.*, 66:3048–3051, Jun 1991.

[95] T. Hayashi, T. Fujisawa, H. D. Cheong, Y. H. Jeong, and Y. Hirayama. Coherent manipulation of electronic states in a double quantum dot. *Phys. Rev. Lett.*, 91:226804, Nov 2003.

[96] M. J. Testolin, J. H. Cole, and L. C. L. Hollenberg. Modeling two-spin dynamics in a noisy environment. *Phys. Rev. A*, 80:042326, Oct 2009.

[97] C. Buizert, F. H. L. Koppens, M. Pioro-Ladrière, H. Tranitz, I. T. Vink, S. Tarucha, W. Wegscheider, and L. M. K. Vandersypen. *insitu* reduction of charge noise in $GaAs/Al_xGa_{1-x}As$ schottky-gated devices. *Phys. Rev. Lett.*, 101:226603, Nov 2008.

[98] M. Pioro-Ladrière, John H. Davies, A. R. Long, A. S. Sachrajda, Louis Gaudreau, P. Zawadzki, J. Lapointe, J. Gupta, Z. Wasilewski, and S. Studenikin. Origin of switching noise in GaAs/AlGaAs lateral gated devices. *Phys. Rev. B*, 72:115331, Sep 2005.

[99] D. H. Cobden, N. K. Patel, M. Pepper, D. A. Ritchie, J. E. F. Frost, and G. A. C. Jones. Noise and reproducible structure in a $GaAs/Al_xGa_{1-x}As$ one-dimensional channel. *Phys. Rev. B*, 44:1938–1941, Jul 1991.

[100] D. H. Cobden, A. Savchenko, M. Pepper, N. K. Patel, D. A. Ritchie, J. E. F. Frost, and G. A. C. Jones. Time-irreversible random telegraph signal due to current along a single hopping chain. *Phys. Rev. Lett.*, 69:502–505, Jul 1992.

[101] D. D. Carey, S. T. Stoddart, S. J. Bending, J. J. Harris, and C. T. Foxon. Investigation of deep metastable traps in si δ-doped $GaAs/Al_{0.33}Ga_{0.67}As$ quantum-well samples using noise spectroscopy. *Phys. Rev. B*, 54:2813–2821, Jul 1996.

[102] C. Dekker, A. J. Scholten, F. Liefrink, R. Eppenga, H. van Houten, and C. T. Foxon. Spontaneous resistance switching and low-frequency noise in quantum point contacts. *Phys. Rev. Lett.*, 66:2148–2151, Apr 1991.

[103] S. Gustavsson, R. Leturcq, T. Ihn, K. Ensslin, D.C. Driscoll, and A.C. Gossard. Noise measurements in quantum dots using charge detection techniques. *Physica E: Low-dimensional Systems and Nanostructures*, 40(1):103 – 110, 2007.

[104] L. Gaudreau, A. S. Sachrajda, S. Studenikin, A. Kam, F. Delgado, Y. P. Shim, M. Korkusinski, and P. Hawrylak. Coherent transport through a ring of three quantum dots. *Phys. Rev. B*, 80:075415, Aug 2009.

[105] M. Fujiwara, M. Sasaki, and M. Akiba. Reduction method for low-frequency noise of gaas junction field-effect transistor at a cryogenic temperature. *Appl. Phys. Lett.*, 80(10):1844–1846, 2002.

[106] Aaron Szafer and A. Douglas Stone. Theory of quantum conduction through a constriction. *Phys. Rev. Lett.*, 62:300–303, Jan 1989.

[107] B. J. van Wees, H. van Houten, C. W. J. Beenakker, J. G. Williamson, L. P. Kouwenhoven, D. van der Marel, and C. T. Foxon. Quantized conductance of point contacts in a two-dimensional electron gas. *Phys. Rev. Lett.*, 60:848–850, Feb 1988.

[108] M. Büttiker. Quantized transmission of a saddle-point constriction. *Phys. Rev. B*, 41:7906–7909, Apr 1990.

[109] K. J. Thomas, J. T. Nicholls, M. Y. Simmons, M. Pepper, D. R. Mace, and D. A. Ritchie. Possible spin polarization in a one-dimensional electron gas. *Phys. Rev. Lett.*, 77:135–138, Jul 1996.

[110] S. M. Cronenwett, H. J. Lynch, D. Goldhaber-Gordon, L. P. Kouwenhoven, C. M. Marcus, K. Hirose, N. S. Wingreen, and V. Umansky. Low-temperature fate of the 0.7 structure in a point contact: A kondo-like correlated state in an open system. *Phys. Rev. Lett.*, 88:226805, May 2002.

[111] A. C. Graham, D. L. Sawkey, M. Pepper, M. Y. Simmons, and D. A. Ritchie. Energy-level pinning and the 0.7 spin state in one dimension: GaAs quantum wires studied using finite-bias spectroscopy. *Phys. Rev. B*, 75:035331, Jan 2007.

[112] Y. Meir, K. Hirose, and N.S. Wingreen. Kondo model for the "0.7 anomaly" in transport through a quantum point contact. *Phys. Rev. Lett.*, 89:196802, Oct 2002.

[113] S. Sarkozy, F. Sfigakis, K. Das Gupta, I. Farrer, D. A. Ritchie, G. A. C. Jones, and M. Pepper. Zero-bias anomaly in quantum wires. *Phys. Rev. B*, 79:161307, Apr 2009.

[114] C. Zhang, T. Knuuttila, Y. Dai, R. R. Du, L. N. Pfeiffer, and K. W. West. ν=5/2 fractional quantum hall effect at 10T: Implications for the Pfaffian State. *Phys. Rev. Lett.*, 104:166801, Apr 2010.

[115] L. N. Pfeiffer R. L. Willett, 1 and K. W. West. Measurement of filling factor 5/2 quasiparticle interference with observation of charge e/4 and e/2 period oscillations. *PNAS*, 106:8853–8858, June 2009.

[116] X. Yang, G. Liu, M. Rostami, A.A. Balandin, and K. Mohanram. Graphene ambipolar multiplier phase detector. *Electron Device Letters, IEEE*, 32(10):1328 –1330, Oct. 2011.

[117] Han Wang, A. Hsu, Ki Kang Kim, Jing Kong, and T. Palacios. Gigahertz ambipolar frequency multiplier based on CVD graphene. In *Electron Devices Meeting (IEDM), 2010 IEEE International*, pages 23.6.1 –23.6.4, Dec. 2010.

[118] B. M. Maune, M. G. Borselli, B. Huang, T. D. Ladd, P. W. Deelman, K. S. Holabird, A. A. Kiselev, I. Alvarado-Rodriguez, R. S. Ross, A. E. Schmitz, C. A. Watson M. Sokolich, M. F. Gyure, and A. T. Hunter. Coherent singlet-triplet oscillations in a silicon-based double quantum dot. *Nature*, 481:344–347, Jan 2012.